THE ORIGIN AND $\vec{K}$-SPECTRUM
OF MAGNETOSPHERIC HISS

A DISSERTATION

SUBMITTED TO THE DEPARTMENT OF ELECTRICAL ENGINEERING

AND THE COMMITTEE ON GRADUATE STUDIES

OF STANFORD UNIVERSITY

IN PARTIAL FULFILLMENT OF THE REQUIREMENTS

FOR THE DEGREE OF

DOCTOR OF PHILOSOPHY

By

Alexandr Borisovich Draganov

September, 1993

THE ORIGIN AND $\vec{K}$-SPECTRUM OF MAGNETOSPHERIC HISS

Alexandr Borisovich Draganov, Ph.D.
Stanford University, 1993

Advisor: Umran S. Inan, Professor of Electrical Engineering, Stanford University

Magnetospheric hiss is an intense noise-like electromagnetic whistler-mode emission in the frequency range from several hundred Hz to several kHz, which permeates large regions of the earths magnetosphere. In spite of decades of extensive investigations, the generation mechanisms of hiss remain unclear. Previously suggested models assume hiss generation by energetic electrons in the magnetosphere and predict hiss propagation at small wave normal angles with respect to the earth's magnetic field lines. However, analysis of experimental data has shown that hiss typically possesses a high wave normal angle with respect to the magnetic field. In this research, we investigate the connection between electromagnetic signals originating in lightning discharges (whistlers) and hiss by means of (1) measurement of the average propagation directions of whistlers and hiss using data from the Dynamic Explorer-1 satellite and (2) theoretical modeling of two- and three-dimensional propagation of whistler waves. We perform multiple measurements of the hiss propagation direction, as well as the first measurement of propagation direction of whistlers. Based on the results of the measurements and on extensive two- and three-dimensional ray-tracing calculations, we suggest an entirely new mechanism of hiss generation by multiply reflecting whistlers. Whistlers from different lightning discharges enter the magnetosphere at different locations and propagate along complex ray trajectories which include multiple reflections. They are observed in the magnetosphere with different time delays, so that the cumulative effect from a large number of whistlers in the magnetosphere manifests itself as a noise-like emission, i.e., hiss. Our model is in agreement with experimental results which show that hiss propagates with large wave normal angles with respect to the magnetic field. Estimates show that in view of the global rate of lightning flashes of $\sim 10^2$ per second lightning generated whistlers pump enough wave energy in the magnetosphere to support observed levels of hiss on a global scale, so that magnetospheric hiss may be entirely produced by emissions from lightning.

Approved for publication:
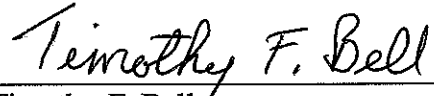
By _____
For Major Department

I certify that I have read this dissertation and that in my opinion it is fully adequate, in scope and quality, as a dissertation for the degree of Doctor of Philosophy.
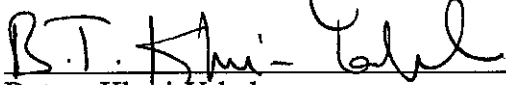
_____
Umran S. Inan   (Principal Advisor)

I certify that I have read this dissertation and that in my opinion it is fully adequate, in scope and quality, as a dissertation for the degree of Doctor of Philosophy.

_____
Timothy F. Bell

I certify that I have read this dissertation and that in my opinion it is fully adequate, in scope and quality, as a dissertation for the degree of Doctor of Philosophy.

_____
Butrus Khuri-Yakub

Approved for the University Committee on Graduate Studies:

_____

This dissertation is dedicated to my wife Luda

Abstract

Magnetospheric hiss is an intense noise-like electromagnetic whistler-mode emission in the frequency range from several hundred Hz to several kHz, which permeates large regions of the earths magnetosphere. In spite of decades of extensive investigations, the generation mechanisms of hiss remain unclear. Previously suggested models assume hiss generation by energetic electrons in the magnetosphere and predict hiss propagation at small wave normal angles with respect to the earth's magnetic field lines. However, analysis of experimental data has shown that hiss typically possesses a high wave normal angle with respect to the magnetic field. In this research, we investigate the connection between electromagnetic signals originating in lightning discharges (whistlers) and hiss by means of (1) measurement of the average propagation directions of whistlers and hiss using data from the Dynamic Explorer-1 satellite and (2) theoretical modeling of two- and three-dimensional propagation of whistler waves. We perform multiple measurements of the hiss propagation direction, as well as the first measurement of propagation direction of whistlers. Based on the results of the measurements and on extensive two- and three-dimensional ray-tracing calculations, we suggest an entirely new mechanism of hiss generation by multiply reflecting whistlers. Whistlers from different lightning discharges enter the magnetosphere at different locations and propagate along complex ray trajectories which include multiple reflections. They are observed in the magnetosphere with different time delays, so that the cumulative effect from a large number of whistlers

in the magnetosphere manifests itself as a noise-like emission, i.e., hiss. Our model is in agreement with experimental results which show that hiss propagates with large wave normal angles with respect to the magnetic field. Estimates show that in view of the global rate of lightning flashes of $\sim 10^2$ per second lightning generated whistlers pump enough wave energy in the magnetosphere to support observed levels of hiss on a global scale, so that magnetospheric hiss may be entirely produced by emissions from lightning.

Preface

If I have ever done a piece of interesting research at Stanford, or if I succeed in doing research in future, I will attribute it to the cooperative and open atmosphere I encountered in the STAR Lab. The door to the office of my advisor, Professor U. S. Inan was always open for students, and I appreciate numerous discussions with him. Professor Inan is one of the most enthusiastic persons I met, and he has always been interested to hear about new ideas a novice student like myself brought to him, even if they were of no value at all.

I am grateful my associate advisor, Dr. Tim Bell for his valuable comments. I admire his unique ability to see physics in cumbersome equations. My special thanks are to Dr. Sonwalkar who introduced me to the world of data analysis and has shown me that experimental science can be even more rewarding than pure theory. I also appreciate his help with the Stanford ray-tracing code. I thank Professors Robert Helliwell and Donald Carpenter for many stimulating and illuminating discussions, and Jerry Yarbrough for carrying out the spectral analysis of the experimental data used in this work.

A drastic change in my life from Kiev to Stanford could have resulted in a shock, if I have not received a lot of help from many American friends. I express sincere gratitude to Tom Sege for his help. Due to support and advice from other students, most notably from Lee Poulsen, John and Becky Jackson and my former roommate Eric Perozziello,

my adaptation to the US lifestyle turned out to be smooth and with a relatively few mess-ups. I enjoyed numerous conversations with and appreciate help from Yuri Taranenko, Juan Rodriguez, Bill Burgess, Tom Mielke, Steve Cummer, Victor Pasko and all other students in the VLF group of the STAR Laboratory.

Looking at the three years I have spent at Stanford, I realize that none of what I have done here would have been possible without my previous background from Kiev University. I cannot overstate the contribution of my former advisors Prof. N. Y. Kotsarenko and Dr. V. M. Chmyrev. I also learned a lot from my former colleagues A. A. Silivra and V. M. Pergamenshchik.

The contribution of my family is beyond words. My wife Luda greatly supported my every step, and listened to endless stories about hiss and whistlers every evening. Our daughter Anna provided me with many inspirational moments. In return, she was able to use old drafts of this thesis to produce her own writings and drawings. The work of my father Prof. Boris Draganov has always been an example of a lifetime commitment to science and research.

ALEXANDR B. DRAGANOV

Stanford, California
September 15, 1993

Contents

Tables

Illustrations

1

Introduction

1.1 OVERVIEW

The subject of this thesis is the origin and propagation characteristics of a particular type of incoherent extremely low frequency (ELF) and/or very low frequency (VLF) electromagnetic emission (i.e., few hundred Hz to few kHz), commonly referred to as *plasmaspheric hiss*, that permeates large regions of the Earth's near space environment.

In this chapter, we review previous experimental and theoretical work on plasmaspheric hiss. The study of this phenomenon has a shorter history compared to other wave phenomena in the Earth's *magnetosphere*, which is the region surrounding the planet within which the Earth's magnetic field dominantly influences the dynamics of charged particles. For example, electromagnetic impulses injected into the magnetosphere by lightning discharges, and which upon propagation disperse into descending tones referred to as *whistlers* [*Helliwell*, 1965], were observed as early as 1919, and later interpreted as having resulted from propagation along the earth's magnetic field lines [*Storey*, 1953]. However, the discovery of many other natural ELF/VLF emissions in the magnetosphere occurred only after the beginning of the satellite era. The list of the most common electromagnetic emissions in the magnetosphere includes *auroral kilometric radiation, auroral*

hiss, Z mode radiation, terrestrial myriametric radiation, whistlers, chorus and *plasma-spheric hiss* [*Gurnett and Inan*, 1988]. Among other ELF/VLF emissions, plasmaspheric hiss is one of a great significance due to its relatively high amplitude and its omnipresence within the relatively dense region of the magnetosphere referred to as the plasmasphere [*Carpenter*, 1973]. As the most common ELF/VLF emission, the plasmaspheric hiss has been suggested to play a fundamental role in regulating the equilibrium flux of the radiation belt [*Kennel and Petschek*, 1966].

Despite extensive study, the mechanisms of generation and sustenance of plasmaspheric hiss are not yet understood. Our review of the past work on plasmaspheric hiss study is organized as follows. We first provide in Section 1.2 the basic properties of whistler mode wave propagation in magnetoplasmas which are essential for the understanding and interpretation of plasmaspheric hiss properties. New experimental data on plasmaspheric hiss are then presented in Section 1.3, and a review of published results on the wavevector direction of plasmaspheric hiss is given in Section 1.4. Theoretical modeling work concerning plasmaspheric hiss generation and propagation are reviewed in Section 1.5, and past results concerning the interaction of plasmaspheric hiss with energetic particles are discussed in Section 1.6. Finally, Section 1.7 summarizes the scientific contributions of this dissertation.

1.2 WHISTLER MODE WAVES IN A MAGNETOPLASMA

Electromagnetic wave propagation in a plasma is considerably different from that in the free space [*Krall and Trivelpiece*, 1973]. Electromagnetically, the plasma medium is dispersive, and the dispersion affects the wave propagation for wave frequencies not very high compared to either of the two major plasma resonance frequencies, namely, the electron plasma frequency* $\omega_{pe} = (\frac{4\pi Ne^2}{m})^{1/2}$ and electron gyrofrequency $\omega_{He} = \frac{eH}{mc}$, where N is the electron density, H is the ambient magnetic field, e and m are the electron

---

* CGS units are used throughout this dissertation.

charge and mass, and c is the speed of light. Both ω_{pe} and ω_{He} vary considerably within the magnetosphere due to the spatial variation of both the plasma density and the earth's magnetic field intensity. Two major regions exist in the magnetosphere within which the wave propagation properties are drastically different due to differences in background electron density (i.e., ω_{pe}). The inner region is known as the plasmasphere [*Carpenter*, 1973], which extends to equatorial distances of 3-7 Earth radii and which is characterized by relatively high plasma densities, so that the condition $\omega_{pe} > \omega_{He}$ is satisfied. Outside the plasmasphere, this condition may be not valid since the plasma density exhibits a very steep drop at the boundary of the plasmasphere, and so does the plasma frequency. The boundary of the plasmasphere is commonly referred to as *plasmapause*. The earth's plasmasphere and magnetic field lines are sketched in Figure 1.1. The radius of the plasmasphere depends on the current magnetic activity, and is greater during magnetospherically quiet periods [*Carpenter*, 1973].

In this work, since we are mainly concerned with wave propagation phenomena within the plasmasphere, we will uniformly assume that the plasma frequency exceeds the gyrofrequency (i.e., $\omega_{pe} > \omega_{He}$). Under this condition, the wave propagation at frequencies below the electron gyrofrequency (but higher than ion gyrofrequencies) typically occurs in the whistler mode [*Krall and Trivelpiece*, 1973]. Since a complete review of wave modes of the magnetized plasma is beyond the scope of this dissertation, we concentrate below mainly on whistler mode features in a cold plasma.

An important parameter characterizing whistler mode propagation is *the wave-normal angle* ψ, which is the angle between the wave vector $\vec{k}$ and the ambient magnetic field $\vec{B}_0$. For parallel propagation with $\vec{k} \parallel \vec{B}_0$ (i.e., $\psi = 0$), the whistler wave frequency ω and wave vector k satisfy the approximate dispersion equation

$$\omega \simeq \omega_{He}\frac{c^2 k^2}{\omega_{pe}^2 + c^2 k^2} \qquad (1.2.1)$$

The parallel propagating whistler wave is circularly polarized with a refractive index $\mu = \frac{ck}{\omega}$ of several tens for typical magnetospheric parameters and with both $\vec{E}$ and
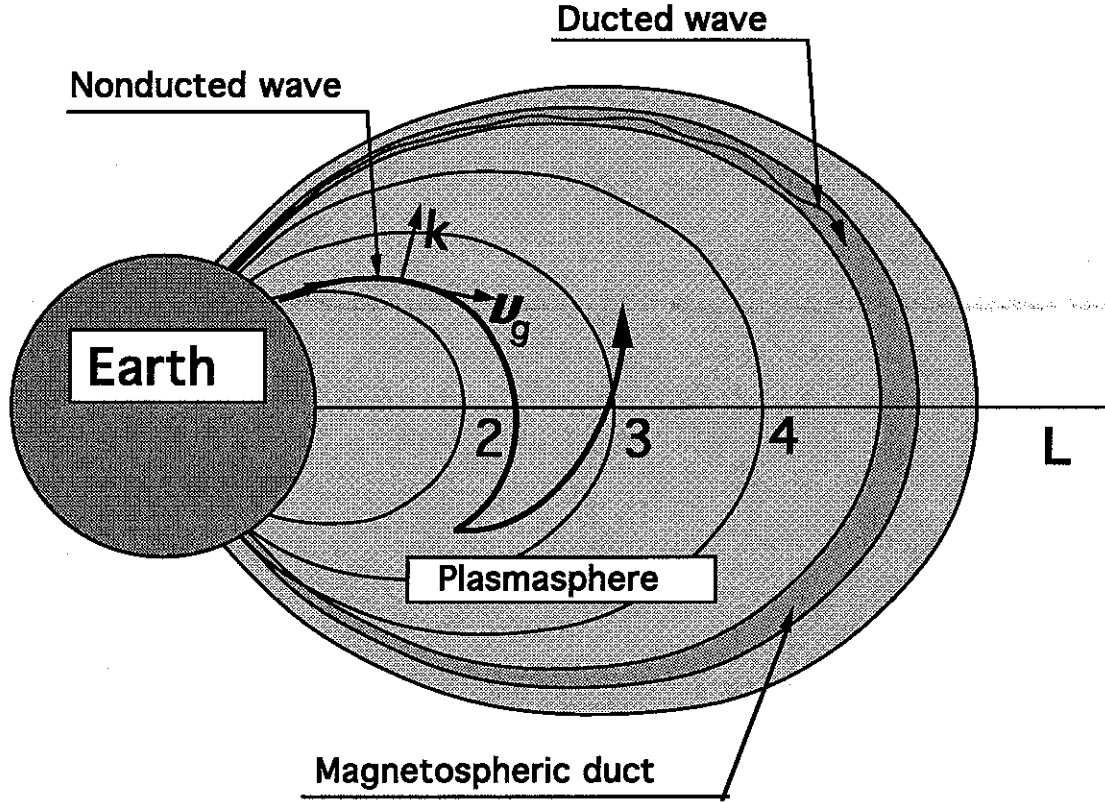
Fig. 1.1.   The earth, and the earth's magnetosphere.   The lightly shaded area designates the plasmasphere. A plasmaspheric duct is shown by darker shading. Both nonducted and ducted whistler-mode ray trajectories are shown.

$\vec{B}$ fields perpendicular to $\vec{k}$, so that the ratio of magnetic to electric field magnitudes is related to the refractive index as $\mu = \frac{cB}{E}$. However, the properties of the whistler wave are different and more complex for oblique propagation (i.e., $\psi \neq 0$). For a given frequency, there exists a so called *resonance cone angle* ψ_r such that for $\psi \rightarrow \psi_r$ the wave refractive index becomes very large ($\mu \rightarrow \infty$), and the wave becomes quasi-electrostatic $\left(\frac{B}{E} \rightarrow 0 \right)$. The resonance cone angle is given as [*Krall and Trivelpiece*, 1973]

$$ cos^2 \psi_r = \frac{\omega^2 (1 + \frac{\omega_{pe}^2}{\omega_{He}^2}) - \omega_{pi}^2}{\omega_{pe}^2} \qquad (1.2.2) $$

where $\omega_{pi} = (\frac{4\pi n e^2}{m_i})^{1/2}$ is the ion plasma frequency, and m_i is the ion mass. We can see from (1.2.2) that for ψ_r to be real we must have $\omega > \omega_{LHR}$, where $\omega_{LHR}^2 = \frac{\omega_{pi}^2 \omega_{He}^2}{\omega_{pe}^2 + \omega_{He}^2}$ is so called lower hybrid resonance (LHR) frequency. The spectra of oblique quasi-electrostatic whistler mode waves with large refractive indices thus exhibit a lower frequency cutoff below the local LHR frequency.

While the dispersion equations (1.2.1) and (1.2.2) are applicable to a homogeneous plasma only, the inhomogeneity of the magnetospheric plasma is often an important factor which determines the propagation characteristics and which therefore must be included in most models of whistler wave generation, amplification and propagation in the magnetosphere. The most common method used to account for the effects of inhomogeneity is to rely on the WKB approximation, applicable when the wave parameters at any point along a given ray trajectory are determined solely by local plasma parameters, so that the ray trajectory can be found as the solution of Hamiltonian-type differential equations [e.g., *Budden*, 1985; *Galeev, and Sudan*, 1983]. This method is based on the assumption that plasma and wave parameters do not change significantly over distances of the order of one wavelength and is widely used for ray tracing simulation of the wave propagation in space plasma [e.g., *Green et al.*, 1977; *Maggs*, 1989]. Depending on the nature of the density inhomogeneity, two major types of whistler mode ray trajectories are possible in the magnetosphere. Ducted propagation occurs within field aligned inhomogeneities (*ducts*), where the plasma density is somewhat higher (10% -30%) than the ambient plasma density [*Helliwell*, 1965]. Calculations show that whistler mode waves may propagate between hemispheres inside such ducts, with the wave vector remaining quasi parallel to the earth's magnetic field [*Helliwell*, 1965]. Since ducted propagation is quasi-longitudinal, whistler mode waves can reach the ionosphere, penetrate the sharp refractive index boundary of the lower ionosphere, and be detected on the ground. In the absence of such guiding by ducts, whistler mode wave propagation paths are governed by smooth gradients of electron density and magnetic field (Fig. 1.1), and such waves are said to propagate in the non-ducted mode [*Helliwell*, 1965]. Under typical

circumstances, the wave normal angle of nonducted waves tends to increase along the propagation path, and may reach values close to the resonance cone [*Aikyo and Ondoh*, 1971; *Huang and Goertz*, 1983; *Jasna et al.*, 1990]. Such waves reflect either within the medium at points where $\omega \simeq \omega_{LHR}$, or from the sharp lower ionospheric boundary (for $\omega > \omega_{LHR}$), and therefore are generally not detectable on the ground. Observations of ducted whistlers at ground stations indicate that whistler ducts are common within the magnetosphere [*Helliwell*, 1965], but it is unlikely that they fill a significant volume of the magnetosphere compared to regions permeated by nonducted whistlers [*Edgar*, 1972]. Therefore, in modeling plasmaspheric hiss which populates large regions of the plasma-sphere, non-ducted propagation must be considered as the primary mode of propagation. Ducted and non ducted whistler ray trajectories are illustrated in Figure 1.1.

We note that the dispersion relations (1.2.1) and (1.2.2) give real solutions for frequency if the wave number is real, corresponding to waves which are not attenuated or amplified as appropriate for wave propagation in a cold plasma, in which case the waves do not exchange energy with the particle population. The condition of resonant interaction of the waves with charged particles is in the form [*Krall and Trivelpiece*, 1973]:

$$\omega - k_{\parallel} v_{\parallel} = \nu \omega_H \qquad (1.2.3)$$

where the subscript $\parallel$ denotes vector components parallel to the ambient magnetic field, ν is an integer, and v is the velocity of the particles which interact with the wave. In the case of $\nu = 0$, equation (1.2.3) describes the Landau interaction or the Čerenkov resonance, and cases $\nu = \pm 1$ are known as the cyclotron resonance or gyroresonance. Higher order resonances ($|\nu| > 1$) result in generally weaker interactions. The interaction of the wave with the energetic particles may lead to wave growth as well as wave damping, depending on the specific features of the particle distribution in velocity space [*Krall and Trivelpiece*, 1973]. In general, non-equilibrium particle distributions (such as beams of energetic particles or loss-cone distributions) can be a source of energy for plasma instabilities and wave growth. Loss cone distributions of energetic electrons are

commonly observed in the magnetosphere [*Lyons and Williams*, 1984], being a potential source of whistler mode wave growth. In controlled VLF wave-injection experiments from Siple Station, Antarctica, whistler mode wave amplification of the order of 20 to 40 dB was detected [*Helliwell*, 1988] and is interpreted as resulting from whistler mode wave gyroresonance interaction with energetic electrons in the equatorial region of the magnetosphere.

Wave-particle interactions result not only in changes of the wave amplitude, but also in particle acceleration/deceleration, as a consequence of the energy exchange between the wave and particles [*Krall and Trivelpiece*, 1973]. In the case of particle interaction with monochromatic waves, the resonant condition at any given point is satisfied only for a single particle parallel velocity (1.2.3). Therefore, if the particle parallel velocity changes either due to the wave-particle interaction or due to the magnetic field inhomogeneity (as discussed in Section 1.6 below), the particles move away from resonance, and the interaction becomes ineffective. Therefore, the velocity of a particle interacting with coherent waves changes within relatively small ranges around their unperturbed trajectories, typically limited by the magnetic field inhomogeneity along the trajectory. In the case of interactions with broadband wave packets, particles can be in resonance with different spectral components of the wave packet as the particle velocity changes. If the different spectral components of the wave packet have random non-correlated phases, the velocity of the particle changes in a random way, so that the initial particle distribution is subject to diffusion in velocity space [*Krall and Trivelpiece*, 1973]. This phenomenon is typical for energetic electron interaction with plasmaspheric hiss, since plasmaspheric hiss is a broadband, noise-like signal without any significant known phase correlation between spectral components.

In the following sections, we discuss the application of the general features of magnetospheric whistler mode wave propagation to the interpretation of experimental data on plasmaspheric hiss and to the theoretical modeling of hiss generation and propagation.

1.3   OBSERVATIONAL DATA ON PLASMASPHERIC HISS

Plasmaspheric hiss is an incoherent, noise-like emission which is most commonly observed in the frequency range from a few hundred Hz to several kHz. Figure 1.2 shows a typical spectrogram of plasmaspheric hiss [*Gurnett and Inan*, 1988], illustrating a steady noise band without any apparent structure.
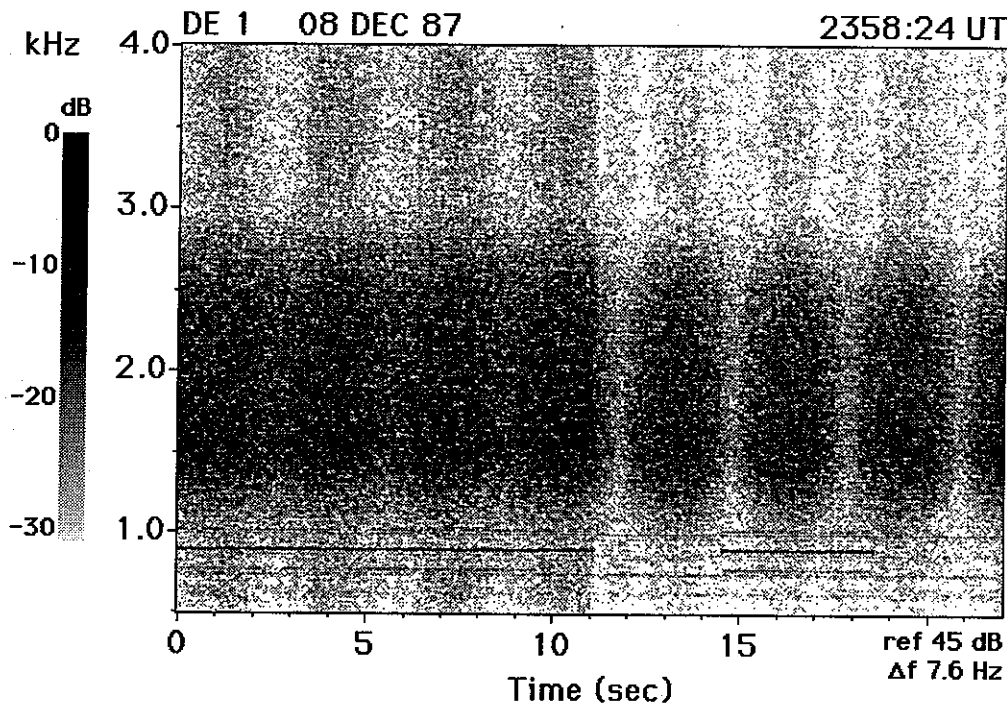
Fig. 1.2. The dynamic spectra of plasmaspheric hiss as observed by the DE-1 satellite. The data for the first ~11 seconds was acquired with the magnetic loop antenna, whereas the subsequent period was detected with the electric dipole antenna [*Shawhan et al.*, 1981]. The periodic variation of the hiss intensity with a period of ~3.05 s is due to the satellite spin with the period of ~6.09 s.

The first observations of plasmaspheric hiss by a high altitude satellite were reported by [*Dunckel and Helliwell*, 1969]. The OGO 1 satellite performed observations of whistler

mode waves in the frequency range 0.3 kHz< f < 100 kHz, covering geocentric distances from 2 to 24 R_E and geomagnetic latitudes in the range of $\pm 50^o$. Plasmaspheric hiss was typically observed in a range of L from $L \simeq 2.5$ to the vicinity of the plasmapause as a noise-like signal with a featureless spectrum exhibiting little change over several to many seconds of observation. The hiss band was typically in the range 0.3 kHz < f <3 kHz, and often occurred together with discrete emissions. *Dunckel and Helliwell* [1969] noted the abrupt upper cutoff of plasmaspheric hiss, which varied with satellite position, in one case, varying from ~ 2 kHz to ~ 500 Hz as the satellite moved from $L \simeq 6.0$ to $L \simeq 8.5$. Mapping of the peak intensity of hiss in the equatorial plane showed two regions of intense emissions near the noon meridian centered at $L \sim 4$ and $L \sim 10$. In the region beyond $L = 6$, little or no hiss was detected in the midnight to dawn sector. Strong hiss was found to develop abruptly at dawn.

A considerable amount of additional observations of plasmaspheric hiss at altitudes ranging from 430 to 900 km was made on the OGO 4 satellite [*Muzzio and Angerami*, 1972]. The intensity of ELF hiss was found to be as high as ~ $2 \times 10^{-4} \gamma^2$/Hz. Other noted characteristics of ELF hiss as observed on the OGO 4 satellite included the following:

1) Although hiss spectra extended up to 2 or 3 kHz, the highest intensity was observed at frequencies below ~ 0.6 kHz. The intense spectral components with frequencies below 0.6 kHz are referred to as band limited hiss (BLH).

2) The upper cutoff of BLH is independent of latitude.

3) Hiss was found to have a considerably smaller upper cutoff frequency in the vicinity of the magnetic equator (latitudes in range of $\pm 10^o$).

4) The range of geomagnetic latitude where hiss occurred varied from ~ $\pm 10^o$ to ~ $\pm 55^o$.

A detailed experimental study of plasmaspheric hiss in the ELF band (<1000 Hz) as observed on the OGO 5 satellite was reported by *Thorne et al.* [1973]. In this study, examples of hiss were excluded from consideration if the upper frequency of hiss

exceeded 1 kHz. A sharp lower-frequency cutoff and a more diffuse upper-frequency cutoff were observed and little variation was found of the principal hiss characteristics (peak frequency, bandwidth, low-frequency cutoff, and maximum power spectral density) throughout most of the plasmasphere. The important aspect of this particular study are the well documented measurements of hiss intensity. Although the peak power density of hiss exhibited variations of up to 2 orders of magnitude around the mean, the most typical hiss intensity was found to be $\sim 10^{-6} \gamma^2 Hz^{-1}$. Hiss was observed almost exclusively within the plasmasphere, and on the dayside passes the termination of hiss was experimentally indistinguishable from the plasmapause crossing. On nightside passes the difference between the plasmapause crossing and the location of termination of the hiss was $\sim$ $0.3 R_E$. However, in the afternoon sector at high geomagnetic latitudes ($\lambda > 35^o$), hiss was observed well outside the plasmapause. Spectra of ELF hiss presented by *Thorne et al.* [1973] typically have smooth maxima of power density at frequencies of a few hundred Hz. Sometimes unusual spectra were observed, showing additional sharp peaks superimposed on a hiss spectrum. The strongest emissions occurred between L=4 and L=6 during geomagnetically quiet conditions. A later statistical study of the data from the OGO-6 satellite shows that plasmaspheric hiss intensity peaks during the recovery phase of magnetic storms [*Smith et al.* 1974].

Some experimental data show that hiss may be observed outside the plasmapause in the regions where the plasma density may be high enough due to local density enhancements. This phenomena was first reported by *Chan and Holzer* [1976], and was further studied by *Koons* [1989]. Enhancements of up to several times the ambient density [*Chan and Holzer*, 1976] and with transverse dimensions of order of $\sim 10^3$ km [*Chan and Holzer*, 1976; *Koons*, 1989] were observed.

Koons [1981] provided experimental data suggesting that hiss can be an energy source for chorus generation. Observations were made by the SCATHA spacecraft, with a nearly equatorial plane orbit having an apogee of 7.78 R_E, and a perigee of 5.32 R_E. In 20 different cases, chorus emissions (with a frequency up to 1.3 kHz) were seen to originate

from hiss bands (with frequency of ~400 Hz). Since the spacecraft spun at a rate of once per minute, the relative orientation of the wave electric and magnetic field and the satellite antenna varied with the same angular frequency, resulting in fading patterns in the received amplitudes of the electric and magnetic fields. In the *Koons* [1981] data, hiss exhibited deep fading nulls (up to 15 dB), whereas chorus emissions had large variations in amplitude which masked any modulation of intensity with satellite spin.

The possibility of chorus generation from plasmaspheric hiss was confirmed in an experiment in which the Siple Station VLF transmitter was used to generate a noise-like signal as a model for magnetospheric hiss [*Helliwell et al.*, 1986]. In this experiment, rising tone triggered emissions (similar to chorus) were observed when the bandwidth of the simulated noise signal was less than ~100 Hz, implying that magnetospheric chorus emission can indeed be triggered by hiss.

Data from the DE-1 satellite provided new information on plasmaspheric hiss generation. In observations described by *Sonwalkar and Inan* [1989], a hiss-like signal was seen to appear after the observation of lightning-generated whistlers (see Figure 1.3). The data were collected during 22 passes of the DE-1 satellite covering $3.4 < L < 5.1$ and geomagnetic latitude of 20^oN to 40^oS in the afternoon ($\sim 1400 - 1500$ MLT) sector. The geomagnetic activity during this period was relatively quiet ($\Sigma K_p < 20$). The whistler triggered hiss emissions were observed on 16 (~70%) of the passes, and they exhibited the following characteristics:

1) The emissions were broadband, structureless and their spectra layed below ~4 kHz.

2) The duration of the whistler triggered hiss was $\sim$ 5 - 15 s.

3) The triggered hiss emissions exhibited the same type of fading as that reported earlier for plasmaspheric hiss.

4) The intensity of triggered hiss emissions was comparable to that of plasmaspheric hiss.

5) The triggered hiss signal had variable upper and lower frequency cutoffs, similar to those observed for magnetospherically reflected whistlers [*Edgar*, 1976].
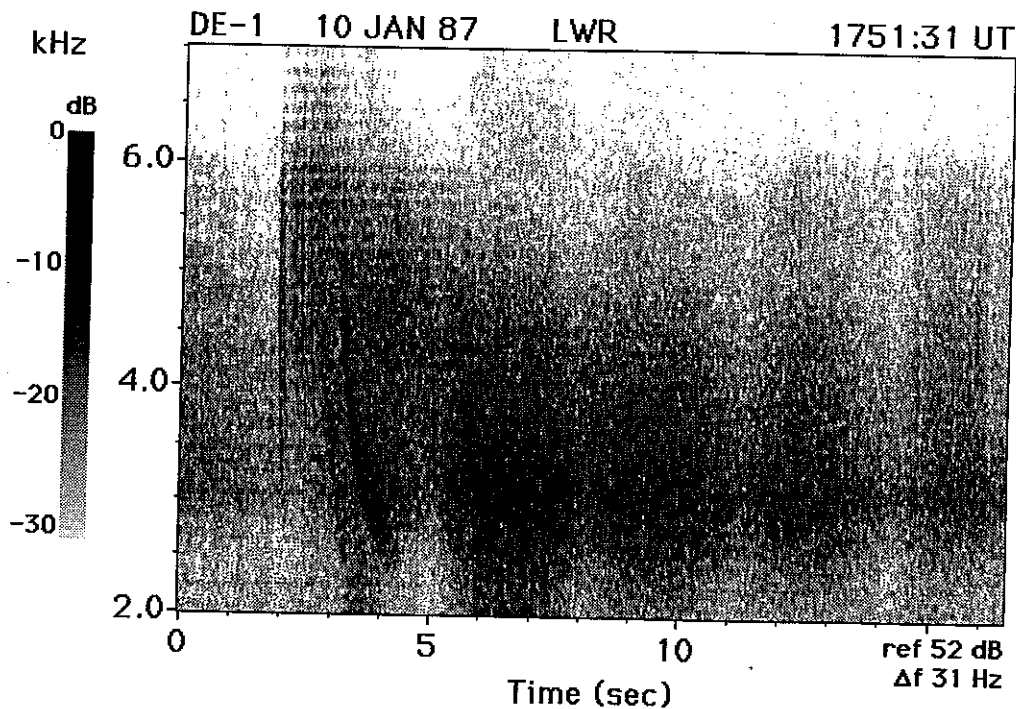
Fig. 1.3. Whistler triggered Hiss [*Sonwalkar and Inan*, **1989**] The triggered hiss lasts for ~5-15 seconds, and exhibits both lower and higher frequency cutoffs.

By combining these factors, *Sonwalkar and Inan* [1989] arrived at the conclusion that lightning generated whistlers may be an embryonic source of plasmaspheric hiss.

Though plasmaspheric hiss is generally observed at high altitudes, some interesting observational results were also obtained by low-altitude satellites and sounding rockets. Based on their analysis of hiss observed on the low-altitude Injun-3 satellite *Gurnett and Burns* [1968] arrived at the conclusion that low-altitude hiss originates at higher altitudes. Their interpretation of the sharp low-frequency cutoff of hiss was based on the reflection of downward-propagating (from a high altitude source region) extraordinary mode waves near the two-ion cutoff frequency between the proton and helium frequency. *Lefeuvre et al.* [1991] determined the direction of the Poynting flux for low-altitude hiss. Except in high-latitude regions, plasmaspheric hiss was found to propagate downwards, suggesting

once again a source region located at higher altitudes. Further analysis showed that the reflection at the two-ion cutoff frequency is a very efficient process for returning waves to higher altitudes [*Lefeuvre et al.,* 1992]. Another experimental evidence of the downward propagation of hiss, was uncovered in experiments using sounding rockets in Antarctica [*Brittain, et al.* 1983], when standing wave patterns of VLF hiss were observed at altitudes above 90 km. The wave amplitude was seen as a series of closely spaced stripes with whistler-like dispersion. This phenomenon was interpreted as a result of the reflection of downcoming plasmaspheric hiss from a sharp boundary in the ionosphere at the altitude $h \sim 90$ km. In view of the relatively low altitude of the rocket, this particular observation may have been ducted hiss also observable on the ground.

1.4 WAVE-NORMAL ANALYSES OF PLASMASPHERIC HISS

Another important hiss characteristic first determined by *Thorne et al.* [1973] is wave polarization and wave normal direction. These parameters were deducted from simultaneous measurements of all three components of the wave magnetic field. In a typical case, no average wave normal angle was found, indicating that waves may be arriving at the observation point from many directions simultaneously. However, in several examples waves exhibited nearly plane polarization; in these cases the wave normal angle was found to be relatively small, being $\psi \simeq 19^o$.

A comprehensive study of wave normal angles of plasmaspheric hiss was carried out by *Lefeuvre et al.* [1983], *Lefeuvre and Helliwell* [1985] and continued by *Storey et al.* [1991]. The wave distribution function (WDF) method was used in these studies, with the WDF specifying the distribution of electromagnetic wave energy with respect to angular frequency ω and to the direction of wave vector as characterized by the unit vector $\kappa = \vec{k}/k$ [*Lefeuvre et al.,* 1981]. The experimental data used for these analyses were obtained by the wave normal analyzer on the ISEE-1 satellite which provided amplitudes and relative phases of two components of electric field and three components of magnetic

field at the output of narrow-band filters. Comparing the ratio of amplitudes of the different field components and their relative phases with theoretically calculated values from cold plasma theory, one can reconstruct the WDF, though with limited directional resolution. This method requires a priori knowledge of the principal plasma parameters, including the plasma density. Wave data for analysis were selected on the basis of several physical criteria, including magnetospherically quiet periods ($K_p < 3$ during three previous days), and satellite passes close to the magnetic equatorial plane. The results of the WDF reconstruction showed that distributions with one, two or three maxima in wave normal angle were possible, indicating that plasmaspheric hiss in the ELF band may have a complicated distribution of wave energy with respect to the wave normal direction. In most cases, the location of the maxima corresponded to high wave normal angles ($\psi \sim 80^o - 85^o$), though during one satellite pass the WDF had a maximum at relatively small wave normal angles ($\psi \sim 20^o - 30^o$).

Results of the analysis of DE-1 data on hiss obtained in the inner magnetosphere were described by *Sonwalkar and Inan* [1988] and summarized by *Gurnett and Inan* [1988]. Observations of plasmaspheric hiss on the DE 1 satellite were made by both electric and magnetic antennas. Since the satellite spun with a period of ~6.09 s, the magnitude of the electric and magnetic field detected by the wave receivers depended on the relative orientation of the field with respect to the antenna and exhibited fading patterns with a period equal to half of the spin period. The phase and the depth of the fading patterns were analyzed to determine the wave normal angle of plasmaspheric hiss during a ~3 hour period when the satellite moved at $L \simeq 4 - 5$ from a geomagnetic latitude of $\lambda_m \simeq 40^o$N to $\lambda_m \simeq 20^o$S. During this time, plasmaspheric hiss was observed continuously below 1.8 kHz. Data analysis showed generally high values of the wave normal angle ranging from $\theta \simeq 50^o$ to $\theta \simeq 82^o$ [*Sonwalkar and Inan*, 1988].

Hattori et al. [1991] reported spectral analysis and direction finding of ELF data containing simultaneous hiss and chorus observed in the outer magnetosphere. Each chorus element was shown to have a tendency to originate from the hiss band and was

asymptotic to the hiss band. Very similar azimuthal angle values were noticed for both hiss and chorus. These facts imply that wavelets emerging from the upper edge of the hiss band can evolve into chorus emission through coherent wave-particle interaction in the outer magnetosphere, as was suggested before [e.g., *Koons*, 1981].

1.5   THEORETICAL MODELING OF PLASMASPHERIC HISS GENERATION

We now review past theoretical work concerning the mechanism of generation of plasmaspheric hiss. In all models proposed prior to our work, plasmaspheric hiss is assumed to be generated by non-equilibrium energetic particle distributions in the magnetosphere.

Muzzio and Angerami [1972] gave the first estimates of the possibility of hiss generation by energetic electrons, assumed to interact with the wave via Landau or gyroresonance. Considering the wave energy emitted by a single electron, estimates were made of the density of energetic particle population in the magnetosphere required to generate the observed levels of plasmaspheric hiss. In such a model, hiss is presumed to be generated by an incoherent process, with the total wave power being equal to the power generated by one electron multiplied by the total number of electrons. The estimates of *Muzzio and Angerami* [1972] required an excessively large number for the density of energetic electrons, illustrating that plasmaspheric hiss was not generated via an involving Landau or gyroresonance process.

Most of the other models of hiss generation are based on plasma instabilities. In order to quantitatively assess the generation of hiss from background noise, the growth rates of whistler mode waves should be integrated along the propagation path. Whistler mode waves with high wave normal angles interact with electrons via Landau resonance, leading to wave damping for typical electron distributions in the magnetosphere. On the other hand, whistler waves with low wave normal angles (quasi-parallel propagation) can be efficiently amplified via gyroresonance with energetic particles if there exist nonequilibrium particle distributions (for example, a loss cone distribution [*Kennel and Petschek*, 1966]).

Therefore, wave growth would occur mainly on those segments of the ray trajectory where the wave normal angle is small and the condition for gyroresonance with energetic electrons can be satisfied. Other segments of the trajectory would contribute to wave damping. If the path integrated growth can overcome the losses due to wave damping and wave divergence, plasmaspheric hiss can be generated from thermal noise or from an embryonic source. *Thorne et al.* [1979] and *Church and Thorne* [1983] postulated hiss generation to be based on the existence of very specific whistler mode wave ray paths (so called cyclic trajectories) which are quasi-periodic, and which cross the equatorial plane at small wave-normal angles. The net gain as calculated in *Church and Thorne* [1983] for a cyclic trajectory exceeds unity, so that the system is unstable and whistler mode waves can be generated from thermal noise, providing a possible mechanism of plasmaspheric hiss generation. In general, cyclic trajectories require reflections of the whistler wave not only from surfaces of constant LHR frequency, but also from the plasmapause. Trajectories with such specific requirements can only constitute a small fraction of possible whistler mode ray trajectories in the magnetosphere. Furthermore, divergence of the wave power (resulting in decrease of the wave amplitude during propagation) was not taken into account in the mechanism proposed by *Church and Thorne* [1983], so that their calculations overestimate the total wave growth rate. Another difficulty with this mechanism is the fact that the cyclic trajectories require small wave normal angles near the equator, whereas recent experimental data show in general high wave normal angles for hiss near the equatorial plane [*Storey et al.*, 1991]. On this basis, *Storey et al.* [1991] arrived at the conclusion that waves propagating along cyclic trajectories may play at best a minor role in generating plasmaspheric hiss. In contradiction to the results of *Church and Thorne* [1983], *Huang et al.* [1983] showed that for typical magnetospheric parameters, the integrated gain of whistler mode waves does not exceed the threshold for wave generation from background noise, although if the whistler mode wave is externally injected into the magnetosphere, it can persist there for a long time without significant damping.

One possible way to explain plasmaspheric hiss generation by energetic electrons in the magnetosphere is to assume that hiss is amplified to its observed level from thermal noise during a single pass of a whistler mode wave through the equatorial generation region. Once generated at low wave normal angles, hiss propagates in the magnetosphere in the non-ducted mode, with the wave normal angles increasing along the path and undergoing reflections from surfaces of constant LHR frequency at high wave normal angles. Such a model was presented by *Solomon et al.* [1988], combining the effectiveness of plasmaspheric hiss generation at low wave normal angles with the experimentally observed propagation at the high wave-normal angles. Based on experimental data on fluxes of energetic electrons from the GEOS-1 satellite, *Solomon et al.* [1988] evaluated the total single-pass amplification of whistler-mode waves inside the plasmasphere to be $\sim 10^2$ dB, high enough to provide the observed wave intensity of ~ 1 pT^2/Hz during a single transit of the wave through the equatorial region at magnetic latitudes of $\lambda < 20^o$. Due to the limitations of the GEOS-1 satellite orbit, the *Solomon et al.* [1988] observations were necessarily limited to high L-shells and unusually quiet geomagnetic conditions. It is thus difficult to assess the applicability of this mechanism in the bulk of the plasmasphere.

Another model of generation of plasmaspheric hiss at high wave normal angles, was developed by *Parady* [1974]. Ring current protons were suggested as the source of the free energy for plasmaspheric hiss generation. The non-equilibrium distribution of the ring current protons is unstable and a so-called "loss-cone" instability can develop in the magnetosphere. This mechanism predicts plasmaspheric hiss to consist of highly oblique waves with center frequency close to the lower-hybrid frequency. The predicted bandwidth of plasmaspheric hiss is in reasonable agreement with experimental data. The author arrived at the conclusion that the ring current instability can be a mechanism for the generation of some types of plasmaspheric hiss. This assumption is confirmed by satellite observations [*Parady et al.,* 1975] showing that the location of the outer boundary of the region where hiss was observed is correlated with the ring current index. In particular, the boundary location near midnight ranged from $L=2.5$ for $Dst = -160\gamma$

to $L=5.5$ for $Dst = 0$. The most intense hiss was observed in the recovery phase of magnetic storms at the inner edge of the ring current. In *Parady et al.* [1975], maps of hiss occurrence were presented which agree qualitatively with previous observations of plasmaspheric hiss occurrence [*Thorne et al.*, 1973].

1.6 PARTICLE PRECIPITATION FROM THE RADIATION BELTS DUE TO THE INTERACTION WITH PLASMASPHERIC HISS

As discussed in Section 1.1, resonant interactions between plasmaspheric hiss and energetic particles constitute an excellent example of a natural process involving charged particle diffusion in velocity space. In the absence of wave-particle interactions and because effects of particle collisions are negligible in the upper ionosphere and magnetosphere, the electron motion in the magnetosphere is determined primarily by the inhomogeneous magnetic field of the earth. In a slowly varying magnetic field, there exist approximate integral constants of motion, one of them (the so-called *first adiabatic invariant*) linking the transverse component of the electron velocity and the magnetic field magnitude [*Krall and Trivelpiece*, 1973]

$$\frac{v_\perp^2}{B} \simeq const \qquad\qquad (1.6.1)$$

When electrons move along the magnetic field lines and reach regions of higher magnetic field at lower altitudes, their transverse velocities increase in accordance with (1.6.1). Since the total electron energy remains constant, the increase in transverse velocity is accompanied with a decrease in longitudinal velocity. At some point along the trajectory (so-called *mirror point*) the longitudinal velocity may equal to zero, and the particle is reflected backward due to the gradient of the magnetic field [*Lyons and Williams*, 1984]. Using the conservation of electron kinetic energy $\frac{m}{2}(v_\perp^2 + v_\parallel^2)$ and the first adiabatic invariant (1.6.1) along the trajectory, one can readily relate the electron pitch angle at the equator α_{eq} to the magnetic field intensities at the equator B_{eq} and the mirror point B_m

as [*Lyons and Williams*, 1984]

$$B_m = \frac{B_{eq}}{\sin^2 \alpha_{eq}}$$

(1.6.2)

From (1.6.2) it follows that electrons having smaller equatorial pitch angles α_{eq} reach regions of higher magnetic field B_m, which correspond to lower altitudes. At altitudes below ~ 100 km, electrons may experience collisions with neutrals, preventing some of them from returning to the magnetosphere. Such electrons are removed from the magnetospheric electron population after several bounces. Since lower mirror points correspond to smaller equatorial pitch angles, the process of electron precipitation to the lower ionosphere and the atmosphere results in nearly zero values of the magnetospheric electron distribution function for pitch angles $\alpha < \alpha_l$, where α_l is the so-called *loss cone angle* [*Lyons and Williams*, 1984].

Electrons can resonantly interact with plasmaspheric hiss and diffuse in velocity space, so that some electrons with initial pitch angles outside the loss cone can diffuse inside the loss cone. Such electrons inside the loss cone reach the lower ionosphere and are precipitated. In this way, the interaction of plasmaspheric hiss with energetic electrons may significantly contribute to the precipitation of these electrons into the ionosphere. A self-consistent theory of this phenomenon was presented in the pioneering work by *Kennel and Petschek* [1966]. Later, this theory was elaborated by *Etcheto et al.* [1973], where an iteration technique was used to find a solution for the intensities of plasmaspheric hiss due to interaction with energetic electrons. In this model, the spectrum of hiss was determined by the energetic electron distribution, and the electron distribution was affected by the waves. These two processes received energy from a steady source of energetic electrons continuously compensating for the losses due to electron precipitation and the damping of waves in the magnetosphere. The principal results from this model can be summarized as follows:

1) The peak frequency of the wave spectrum is a function of the characteristic energy

of the incoming particles, approximately corresponding to that calculated from (1.2.3) with $v_\parallel$ equal to a half of the velocity of the source particles.

2) The peak intensity of the wave is directly proportional to the source intensity.

3) The solution for the equilibrium particle fluxes by [*Etcheto et al.,* 1973] is not unique, so that some other solutions are found, in addition to that put forth by *Kennel and Petschek,* [1966].

4) The equilibrium particle fluxes have the same characteristics inside and outside the plasmasphere.

Lyons et al. [1972] studied the pitch angle diffusion of radiation belt electrons due to their interaction with whistler waves having a Gaussian distribution of wave energy with respect to wave normal angle, with a maximum at $\psi = 0$. Obliquely propagating waves (corresponding to $\psi \neq 0$) interact with particles at all cyclotron harmonic resonances as well as at the Landau resonance. The particle velocity changes occurring at all geomagnetic latitudes along the particle trajectory were considered and the pitch angle changes integrated over a bounce period was found to be significant enough for a slot in the electron distribution function to be formed at $2 < L < 3$. The calculated electron distribution function was in a good agreement with the observed one.

A test particle approach was used by *Inan* [1987] to compare gyroresonant pitch angle scattering of energetic electrons by coherent versus incoherent whistler mode waves. In this study, the equations of motion for individual test particles were solved numerically. The noise-like wave field for the incoherent signal was simulated by a sequence of short monochromatic pulses. Each monochromatic pulse had a duration of 1 ms, and the frequency of such pulses was generated randomly, so that the constituted wave was a signal with nearly constant power spectral density over a bandwidth of 2 kHz centered at 5.5 kHz. Results of the numerical solution for the incoherent signal were compared to the results for the coherent signal. Though the individual particle scattering was found to be typically larger for the coherent signal, the peak precipitation fluxes induced by

the incoherent signal were found to be of the same order of magnitude since incoherent waves interact with particles over a wider range of energies.

Since recent experimental data show that hiss propagates over a wide range of wave normal angles, there must be Landau interactions between hiss and energetic electrons. *Pinto and Gonzalez* [1989] have shown that at low L values, Landau resonance with electrons near their mirror points can produce pitch angle diffusion coefficients larger than those expected for equivalent cyclotron resonances at the equator. The authors suggest that this resonance may be regarded as the most important process to explain the enhancement in energetic electron precipitation at the inner belt, at least during the recovery phase of magnetic storms.

1.7   CONTRIBUTIONS

The specific contributions to our understanding of the wave vector directions and generation mechanisms of magnetospheric hiss that resulted from our work are presented in Chapters 2-3. These can be summarized as follows:

— A new mechanism for generation and sustenance of magnetospheric hiss by whistlers from lightning is put forth and is found to be consistent with experimental data.

— It is shown that lightning generated whistlers inject sufficient wave energy into the magnetosphere to support the observed intensities of hiss on a global scale.

— Measured wave normal angles for hiss were found to be large, ranging from 45° to the resonance cone angle, consistent with the proposed mechanism. Furthermore, the hiss wave vectors are often at large angles with respect to the magnetic meridional plane.

— First measurement of wave normal directions of discrete whistlers indicate them to

be 50°-60° with respect to the magnetic field and within $< 20^o$ with respect to the meridional plane.

– A new asymptotic formulation of whistler wave propagation in three dimensions is put forth. Results of three-dimensional ray-tracing calculations show that the model of hiss generation by whistlers is in agreement with experimental data.

2

Wave normal analysis

2.1 INTRODUCTION

In this chapter we describe the method used for the analysis of VLF wave data from the DE-1 satellite to extract information on wave normal direction, and we provide results of the wave vector direction measurements for plasmaspheric hiss and nonducted whistlers. The DE-1 satellite had a spin period of ~6.09 s, so that the magnitude of the electric and magnetic fields detected by the onboard wave receivers depended on the relative orientation of the wave field and the antennas, and the resultant recorded signal intensity exhibited a fading pattern with a period equal to half the spin period [*Sonwalkar and Inan,* 1986]. This concept is illustrated in Figure 2.1, where both the satellite electric antenna and the polarisation ellipse of the wave field are shown. The spacecraft spin changes the projection of the electric field polarisation ellipse on the antenna, resulting in signal fading. Analysis of the phase and the depth of the fading patterns, together with the full knowledge of the three dimensional attitude of the satellite, allows the determination of the wave vector direction [*Sonwalkar and Inan,* 1986]. In this chapter, we generalize this method to the measurement of the average wave vector direction of short duration signals (e.g., whistlers). Other modifications include taking into account (i) the effects
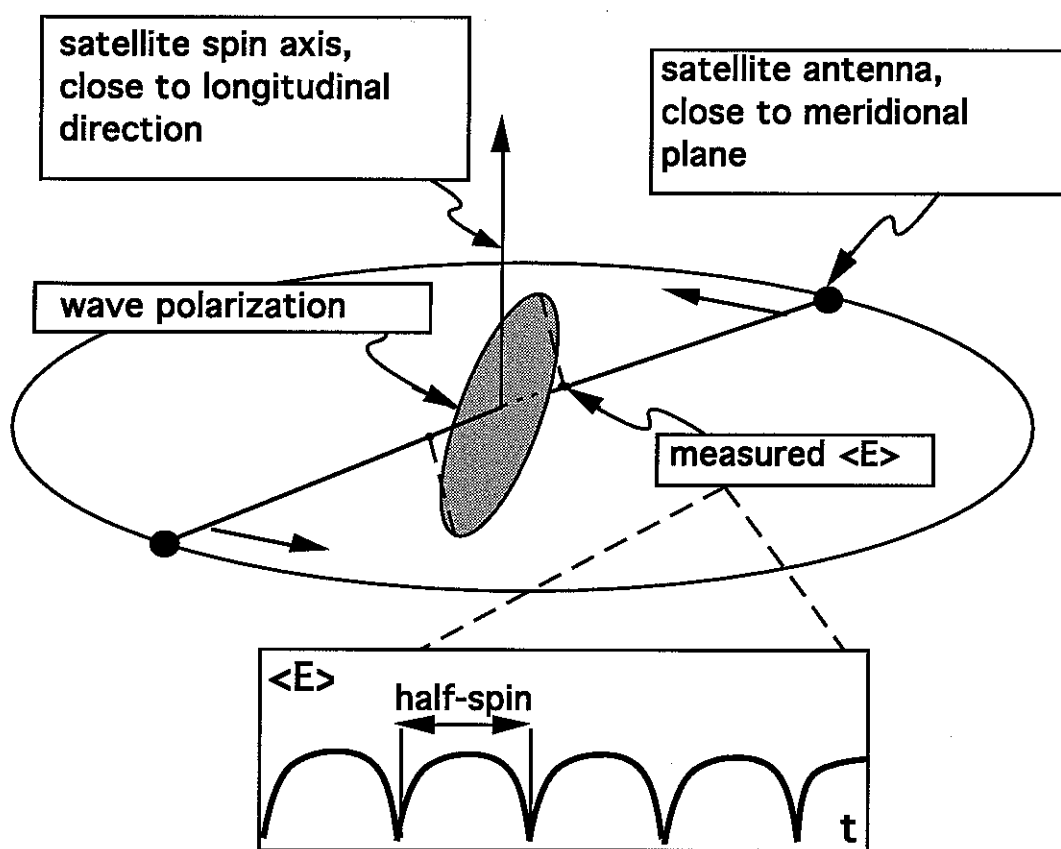
Fig. 2.1.   The geometry of the DE-1 satellite orbit and the spinning electric antenna.
The whistler wave polarisation ellipse is sketched with respect to the antenna orientation.
The measured intensity of the wave depends on the relative orientation of the spinning
antenna with respect to the wave electric field.

of ion motion in the wave-normal angle analysis, and (ii) use of the full envelope of the signal pattern rather than just the measurement of the depth and phase of the fading.

This chapter is organized as follows. In Section 2.2 we provide a derivation of the expression for the fading pattern as observed by the DE-1 satellite in a narrow frequency window. We then show that within certain approximations the relation for wideband signals (e.g., hiss or whistlers) should be similar to that for monochromatic signals. In section 2.3 we evaluate the depth and the phase of fading resulting from the wave vector direction and satellite spin. We arrive at an expression which links the unknown direction of the wave vector to the observable characteristics of signal fading at the antenna terminals. Input parameters in this expression are local cold plasma density, magnetic field intensity and direction, and the satellite orientation. Section 2.4 describes the method for the numerical solution of the equation for the wave vector directions. Section 2.5 provides the results of the wave normal measurements of plasmaspheric hiss at different locations in the magnetosphere and under different magnetospheric conditions. Results of the first simultaneous measurement of wave propagation direction of plasmaspheric hiss and nonducted whistlers are presented in Section 2.6, and are the subject of the theoretical modeling discussed later in Chapter 3.

2.2 FADING PATTERN FOR WIDEBAND SIGNALS

For a given incident wave electric field $\vec{E}$, the instantaneous voltage at the terminals of a linear dipole antenna is given by

$$U = \mathcal{L}\vec{E} \cdot \vec{e}_a \tag{2.2.1}$$

where $\mathcal{L}$ is the effective length of the dipole antenna, and $\vec{e}_a$ is the unit vector in the direction of the dipole. However, (2.2.1) is not useful in the analysis of the wide-band data when the fading due to the satellite spin is measured as the intensity of the broad-band signal in a narrow frequency window. In the following, we derive the relationship

between the signal dynamic spectra as observed by a satellite and the actual wave spectra and antenna orientation. This problem was considered by *Sonwalkar and Inan* [1988], where it was shown that the method of wave normal direction analysis can be applied to noise-like signals (e.g., hiss). We generalize the method of *Sonwalkar and Inan* [1988] and demonstrate its applicability to a wide range of signals.

We consider a wave packet with energy distributed over a range of frequencies (and corresponding wave numbers). The electric field of the wave is given by

$$\vec{E}(\vec{r}, t) = \int \int d\vec{k} d\omega \vec{\mathcal{E}}(\vec{k}, \omega) \exp\left(i(\omega t - \vec{k} \cdot \vec{r})\right) \qquad (2.2.2)$$

where $\vec{\mathcal{E}}(\vec{k}, \omega)$ is the wave spectral density. In general, the wave packet may have different orientations of the wave vector for a given frequency ω. While we are able to determine the fading at the antenna terminals in the general case, we assume in the following that the wave spectral components have a unique orientation of the wave vector for any given frequency. In this case, the wave vector is uniquely determined by the wave frequency, and the spectral density function can be expressed as

$$\vec{\mathcal{E}}(\vec{k}, \omega) = \vec{\mathcal{E}}(\omega)\delta(\vec{k} - \vec{k}_0(\omega)) \qquad (2.2.3)$$

where $\delta(.)$ is the Dirac delta function, and $\vec{k}_0(\omega)$ is a function describing the wave vector dependence on frequency as can be derived from the dispersion relation for the wave.

Since the satellite moves with the velocity $\vec{V}_s$, we can substitute $\vec{r} = \vec{V}_s t$ in (2.2.2) and using also (2.2.3) find

$$\vec{E}(t) = \int d\omega \vec{\mathcal{E}}(\omega) \exp\left(i(\omega - \vec{k}_0 \cdot \vec{V}_s)t\right) \qquad (2.2.4)$$

The voltage waveform at the antenna terminals is defined as

$$U(t) = \int d\omega \mathcal{L}(\omega)\vec{\mathcal{E}}(\omega) \cdot \vec{e}_a(t) \exp\left(i(\omega t - \vec{k}_0 \cdot \vec{V}_s)t\right) \qquad (2.2.5)$$

Note that the antenna orientation vector $\vec{e}_a$ varies slowly (compared to $\frac{2\pi}{\omega}$) with t due to the satellite spin. In general, the effective length of the antenna may be a function of both the wave frequency and the antenna orientation. In the following we consider the case for which $\mathcal{L}$ is constant.

In order to evaluate the voltage variation in a narrow frequency band, we need to first find the spectrum of U in a time window. This procedure is defined by the following formula

$$\mathcal{U}(\Omega, t_0) = \frac{1}{2\pi} \int dt \exp(-i\Omega t) U(t) \Pi\left(\frac{t - t_0}{\Delta t}\right) \qquad (2.2.6)$$

where Π is the window function*, and $\mathcal{U}(\Omega, t_0)$ is the dynamic spectra of the voltage at the antenna terminals measured at $t = t_0$. Substitution of (2.2.5) in (2.2.6) yields

$$\mathcal{U}(\Omega, t_0) = \frac{1}{2\pi}\mathcal{L} \int d\omega \vec{\mathcal{E}}(\omega) \int dt \vec{e}_a(t) \exp\left[i(\omega - \vec{k}_0 \cdot \vec{V}_s)t\right] \exp(-i\Omega t) \Pi\left(\frac{t - t_0}{\Delta t}\right) \quad (2.2.7)$$

We can simplify this expression by performing an approximate integration with respect to t. Note, that $\vec{e}_a(t)$ is a slowly varying function as compared to the exponent. In all practical cases, the width of the time window is small compared to the period of the satellite revolution, so that $\vec{e}_a(t)$ is the slowest function on the right-hand side of (2.2.7). With this realization, we can use an asymptotic expansion for the integral of a product of a slow $f_s(t)$ and fast $f_f(t)$ varying functions

$$\int^t d\tau f_s(\tau) f_f(\tau) \simeq f_s(t) \int^t d\tau f_f(\tau) - f_s'(t) \int^t d\tau \int^\tau d\xi f_f(\xi) + \ldots \qquad (2.2.8)$$

This asymptotic expansion can be easily shown to be valid using integration by parts. Expanding the right-hand side of (2.2.7), we find

$$\mathcal{U}(\Omega, t_0) = \frac{1}{2\pi}\mathcal{L} \int d\omega \vec{e}_a(t_0) \cdot \vec{\mathcal{E}}(\omega) \int dt \exp\left[i(\omega - \Omega - \vec{k}_0 \cdot \vec{V}_s)t\right] \Pi\left(\frac{t - t_0}{\Delta t}\right) \quad (2.2.9)$$

---

* Typically, $\Pi(t) = 1$ for $-\frac{1}{2} < t < \frac{1}{2}$, zero otherwise.

The integration with respect to t yields a function with a sharp impulsive maximum. We note that the integral with respect to t can be written as the Fourier transform

$$\frac{1}{2\pi}\int dt \exp\left(i(\omega - \Omega - \vec{k}_0 \cdot \vec{V}_s)t\right)\Pi\left(\frac{t-t_0}{\Delta t}\right) = \mathcal{F}(-\omega) \qquad (2.2.10)$$

where $\mathcal{F}(\omega)$ denotes the Fourier transform of the function of time $f(t) = \exp\left(i(-\Omega - \vec{k}_0 \cdot \vec{V}_s)t\right)\Pi\left(\frac{t-t_0}{\Delta t}\right)$. Using this definition of $\mathcal{F}$, equation (2.2.9) can be written as

$$\mathcal{U}(\Omega, t_0) = \mathcal{L}\vec{e}_a(t_0) \cdot \int d\omega \vec{\mathcal{E}}(\omega)\mathcal{F} \qquad (2.2.11)$$

Using Parseval's Theorem [e.g., *Bracewell*, 1986]

$$\int d\omega \mathcal{F}_1(\omega)\mathcal{F}_2(-\omega) = \int dt F_1(t)F_2(t) \qquad (2.2.12)$$

equation (2.2.11) yields

$$\mathcal{U}(\Omega, t_0) = \mathcal{L}\vec{e}_a(t_0) \int dt \vec{E}(t)\exp\left(i(-\Omega - \vec{k}_0 \cdot \vec{V}_s)t\right)\Pi\left(\frac{t-t_0}{\Delta t}\right) \qquad (2.2.13)$$

The integral with respect to t in (2.2.13) is by definition the dynamic spectra of the electric field $E(t)$ as measured in a frequency window centered at $\Omega + \vec{k}_0 \cdot \vec{V}_s$ so that with reference to (2.2.6) we can write

$$\mathcal{U}(\Omega, t_0) = \mathcal{L}\vec{e}_a(t_0) \cdot \vec{\mathcal{E}}(\Omega + \vec{k}_0 \cdot \vec{V}_s, t_0) \qquad (2.2.14)$$

which is a simple expression, allowing the evaluation of the dynamic spectra of a signal observed by a satellite in terms of the dynamic spectra of the actual electric field of the wave at the Doppler-shifted frequency, multiplied by the spinning antenna orientation vector. Since the relative orientation of the antenna and the wave electric field changes as the satellite spins, formula (2.2.14) implies that there would be a fading pattern in the measured voltage. In the following we analyze the shape of the fading pattern to determine the wave polarisation and the wave vector direction.

Expression (2.2.14) shows that what is observed is not just the variation of the voltage $\mathcal{U}$ due to the satellite spin ($\vec{e}_a(t_0)$), but the product of $\vec{e}_a(t_0)$ with the changing magnitude of the wave electric field dynamic spectra $\vec{\mathcal{E}}$. To measure the fading itself we should either (i) assume that the wave electric field magnitude remains constant over at least one spin period, or (ii) use superposed epoch technique or statistical averaging to reduce possible variations in $\vec{\mathcal{E}}$. In the following, we assume the former to analyze wave data on hiss, and the latter for analysis of wave data on discrete nonducted whistlers.

In applying (2.2.14) to the analysis of experimental data one should keep in mind the approximations inherent in the derivation. Basically, we assume a hierarchy of fast and slow variables

$$T_a \gg T_w \gg \frac{1}{\omega} \tag{2.2.15}$$

where T_a is the characteristic time scale of the satellite spin and T_w is the width of the window used to obtain the dynamic spectra.

The physical interpretation of the inequality

$$T_a \gg T_w$$

is clear. If one chooses the integration window wide enough to be compared to the period of the satellite spin ($T_a \sim T_w$), the fading pattern is smoothed out by the time integration. In the limiting case of the opposite inequality ($T_a \ll T_w$), there would be no fading pattern at all. Therefore, the width of the integration window should be small enough to bring out the fading of the signal. In turn, the inequality

$$T_w \gg \frac{1}{\omega}$$

sets a lower limit on T_w, to allow for sufficient frequency resolution. For the DE-1 satellite, $T_a \sim \frac{6.09}{2\pi} \sim 1$ s and $\frac{1}{\omega} \sim 10^{-4}$ s, therefore, the window width can be chosen $\sim 10^{-2}$ s, retaining the validity of (2.2.14).

Equation (2.2.14) can be further simplified if the wave vector magnitudes are assumed to be moderate, and if the wave parameters (e.g., wave normal angle) do not change sharply with frequency. In such a case, we can neglect the Doppler-shift term in (2.2.14) to obtain

$$\mathcal{U}(\Omega, t_0) \simeq \mathcal{L}\vec{e}_a(t_0) \cdot \vec{\mathcal{E}}(\Omega) \qquad (2.2.16)$$

As we will see below, this approximation is well justified by the results of the wave vector direction analysis in all cases analyzed here.

2.3   DEPTH AND PHASE OF FADING RESULTING FROM THE WAVE PROPAGATION DIRECTION AND SATELLITE SPIN

In this section, we derive an expression for the functional variation of the voltage fading observed at the terminals of a spinning antenna produced by an elliptically polarized electromagnetic wave. We start with the formula derived above for the voltage at the antenna terminals

$$\mathcal{U} = \mathcal{L}\vec{\mathcal{E}} \cdot \vec{e}_a \qquad (2.3.1)$$

where $\mathcal{L}$ is the antenna effective length, and $\vec{e}_a$ is the unit vector in the direction of the dipole. In order to evaluate $\mathcal{U}$, we need to determine both the orientation of the antenna and the electric field in the same frame of reference x, y, z.

Figure 2.2 shows the coordinate system used. The ambient magnetic field $\vec{B}$ is taken to be along the z-axis, and the electric antenna spin axis $\vec{a}$ is assumed to lie in the x-z plane. The direction of the wave vector $\vec{k}$ is determined by the angles ψ and β. In the formulas below, we also use (x', y', z') axes, which are defined in such a way that z' is parallel to z and $\vec{k}$ is in the (x', z') plane. Another frame of reference is constituted by x_a, y_a, z_a, and is defined in such a way that the antenna spin axis is parallel to $\vec{x}_a$ (Figure 2.2).
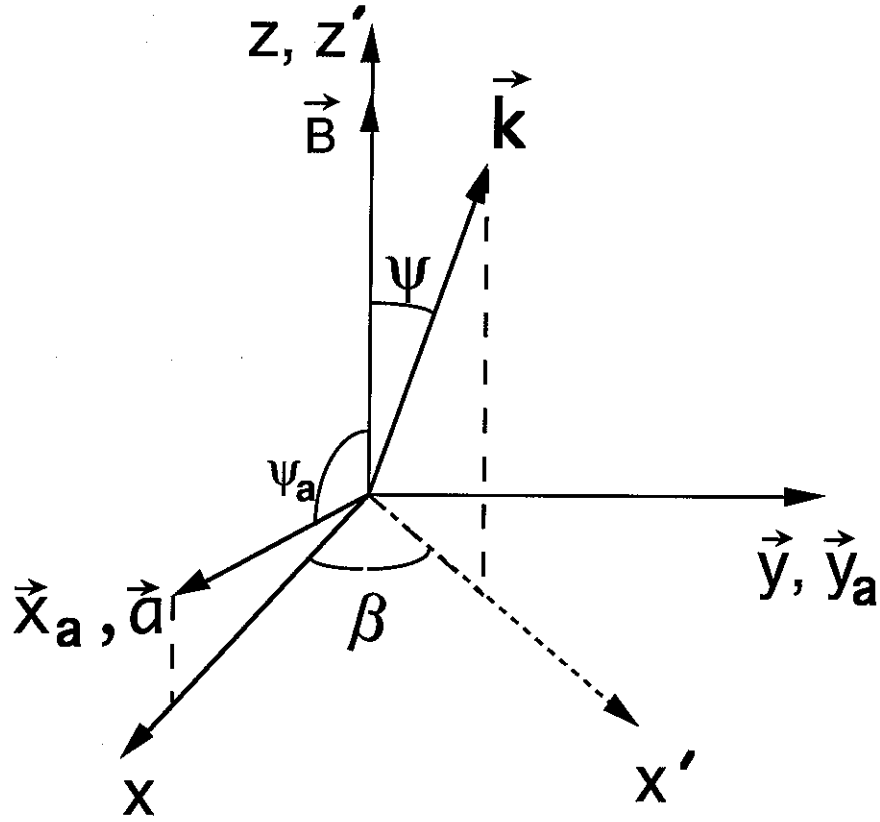
Fig. 2.2. The frame of reference used in the satellite data analysis. The magnetic field is parallel to the $\vec{z}$ axis. The satellite spin axis $\vec{a}$ is in the x, z plane, forming an angle of ψ_a with the magnetic field. The magnetic meridional plane is within a few degrees of the y, z plane. The wave vector orientation is characterized by the wave normal angle ψ and azimuthal angle β.

We start with the determination of the orientation of the antenna in the x_a, y_a, z_a frame of reference. In the following, we choose $t = 0$ as the moment at which the antenna is perpendicular to the earth's magnetic field. Since the antenna spins in x_a, z_a plane, its orientation is given by

$$e_y^a = \cos \omega_s t \qquad\qquad (2.3.2a)$$

$$e_z^a = \sin \omega_s t \qquad\qquad (2.3.2b)$$

$$e_x^a = 0 \qquad\qquad (2.3.2c)$$

We note that the x, y, z frame of reference is rotated by $(\frac{\pi}{2} - \psi_a)$ with respect to the x_a, y_a, z_a frame of reference (Figure 2.2), so that the antenna orientation in the x, y, z frame is

$$e_{x,a} = \sin \omega_s t \cdot \cos \psi_a \qquad\qquad (2.3.3a)$$

$$e_{y,a} = \cos \omega_s t \qquad\qquad (2.3.3b)$$

$$e_{z,a} = \sin \omega_s t \cdot \sin \psi_a \qquad\qquad (2.3.3c)$$

In the x', y', z' frame, the wave electric field vector can be expressed through the complex unit polarisation vector $\vec{e}'$. The expression for the instantaneous value of the wave electric field in terms the unit polarisation vector $\vec{e}'$ is

$$\vec{\mathcal{E}}' = E_m Re\left(\vec{e}' \exp(i\omega t - \vec{k} \cdot \vec{r})\right) \qquad\qquad (2.3.4)$$

where E_m is the electric field magnitude. Expressions for $e'_{1,2,3}$ can be obtained as a solution of a system of three linear equations

$$k^2 e_i' - \sum_{j=1}^{3} (k_i k_j e_j' + \frac{\omega^2}{c^2} \epsilon_{ij} e_j') = 0 \qquad\qquad (2.3.5)$$

where $k_1 = k_{x'} = (k_x^2 + k_y^2)^{\frac{1}{2}}, k_2 = k_{y'} = 0, k_3 = k_{z'} = k_z$, and $\epsilon_{ij}(\omega, \vec{k})$ is the dielectric tensor for the magnetized plasma [Krall and Trivelpiece, 1973] in the same system of reference (x', y', z') where e_i' are defined. The dielectric tensor is defined as

$$\epsilon_{ij} = \delta_{ij} + \sum_{\alpha=1}^{n} \epsilon_{ij}^{\alpha} \qquad\qquad (2.3.6)$$

where $\delta_{ij} = 1$ if $i = j$ and $\delta_{ij} = 0$ otherwise. The summation in (2.3.6) is carried out with respect to different particle species (which in the following are assumed to be electrons

and protons), and the partial dielectric permittivities ϵ_{ij}^{α} are defined as

$$\epsilon_{11}^{\alpha} = -\frac{\omega_{p\alpha}^2}{\omega^2 - \omega_{H\alpha}^2} \qquad (2.3.7a)$$

$$\epsilon_{12}^{\alpha} = -\frac{i\omega_{H\alpha}\omega_{p\alpha}^2}{\omega(\omega^2 - \omega_{H\alpha}^2)} \qquad (2.3.7b)$$

$$\epsilon_{33}^{\alpha} = -\frac{\omega_{p\alpha}^2}{\omega^2} \qquad (2.3.7c)$$

$$\epsilon_{22}^{\alpha} = \epsilon_{11}^{\alpha} \qquad (2.3.7d)$$

$$\epsilon_{21}^{\alpha} = -\epsilon_{12}^{\alpha} \qquad (2.3.7e)$$

$$\epsilon_{31}^{\alpha} = \epsilon_{13}^{\alpha} = \epsilon_{32}^{\alpha} = \epsilon_{23}^{\alpha} = 0 \qquad (2.3.7g)$$

We note that (2.3.6) accounts for contributions from both electron and ion species in the dielectric tensor. Ion motion effects may be important since hiss is often observed at frequencies close to the lower hybrid frequency [*Thorne et al.*, 1973], in which case the propagation of the plasma waves is supported by the motion of both ion and electron species. Using ϵ_{ij} in the form of (2.3.6) is an improvement over previous methods of wave normal measurements using spin fading patterns [*Sonwalkar and Inan*, 1986; 1988] which did not account for the ion motion.

We assume that the $\vec{x}'$ axis makes an angle ϕ with respect to the $\vec{x}$ axis. Transforming the complex unit polarisation vector in the x, y, z frame, we find

$$e_x = e_x' \cos\phi - e_y' \sin\phi \qquad (2.3.8a)$$

$$e_y = e_x' \sin\phi + e_y' \cos\phi \qquad (2.3.8b)$$

$$e_z = e_z' \qquad (2.3.8ac)$$

In the x, y, z frame of reference, the instantaneous value of the wave electric field is given by

$$\mathcal{E}_x = E_m Re\left((e'_x \cos\phi - e'_y \sin\phi)\exp(i\omega t - \vec{k}\cdot\vec{r})\right) \qquad (2.3.9a)$$

$$\mathcal{E}_y = E_m Re\left((e'_x \sin\phi + e'_y \cos\phi)\exp(i\omega t - \vec{k}\cdot\vec{r})\right) \qquad (2.3.9b)$$

$$\mathcal{E}_z = E_m Re\left(e'_z \exp(i\omega t - \vec{k}\cdot\vec{r})\right) \qquad (2.3.9c)$$

These expressions may be used to determine the magnitude of the voltage at the antenna terminals. For the average magnitude of the voltage we can readily find from (2.3.1) that

$$\mathcal{U}_m = \mathcal{L}\left[<(\vec{\mathcal{E}}\cdot\vec{e}_a)^2>\right]^{\frac{1}{2}} \qquad (2.3.10)$$

where $<>$ denotes averaging with respect to time. Substituting in (2.3.10) the expressions for $\vec{\mathcal{E}}$ from (2.3.9) and $\vec{e}_a$ from (2.3.3) and averaging the square of their scalar product, we find

$$\mathcal{U}_m(t) = 2\mathcal{E}_m\mathcal{L}|(e'_x \cos\phi - e'_y \sin\phi)\sin\omega_s t \cdot \cos\psi_a$$

$$+(e'_x \sin\phi + e'_y \cos\phi)\cos\omega_s t + e'_z \sin\omega_s t \cdot \sin\psi_a| \qquad (2.3.11)$$

where $|(.)|$ denotes the absolute value of a complex variable. Note that the value of the complex unit polarisation vector $\vec{e}'$ depends on the plasma parameters and on the wave normal angle ψ (see (2.3.5) - (2.3.7)), so that (2.3.11) expresses the voltage at the antenna terminals through the antenna effective length $\mathcal{L}$, the actual electric field magnitude $\mathcal{E}_m$, the angle of the antenna spin axis orientation ψ_a, the wave vector orientation angles ϕ, ψ, and the plasma parameters. This equation is a starting point for the wave normal analysis of the DE-1 data, since it links a measurable quantity $\mathcal{U}_m$ with the unknown angles ϕ, ψ of the wave vector orientation.

Before we proceed to solve equation (2.3.11) to determine the wave vector orientation, we analytically consider some limiting cases to obtain insight on how the wave vector

orientation manifests itself in the fading pattern of the voltage measured at the terminals of the spinning dipole antenna. For the sake of simplicity, we assume $\psi_a = \frac{\pi}{2}$ in our analytical estimates of the fading pattern, which is a good approximation for the typical DE-1 satellite ephemeris. Note, however, that in the numerical solution of (2.3.11) for the actual data we use the precise values of ψ_a as derived from satellite ephemeris data.

As our first limiting case, we consider a quasi-electrostatic whistler mode wave with wave vector close to the resonance cone. In this case, the solution of equations (2.3.5) for the complex unit polarisation vector gives real values for e'_x, e'_z and a small imaginary value for e'_y, the latter approaching zero as the wave vector approaches the resonance cone. Qualitatively, this behavior is understandable by the fact that whistler mode waves exhibit almost linear polarisation in the direction of their wave vector for wave vectors close to the resonance cone [*Krall and Trivelpiece*, 1973]. Therefore, the two components of the polarisation vector which lie in the wave vector plane x, z must be in phase (so that both are real), and the third component e'_y must be small. Using the real values of the $e'_{x,z}$ components and considering e'_y as a small parameter, we find for U_m

$$\mathcal{U}_m \simeq 2\mathcal{E}_m\mathcal{L}\left(\frac{R + (\cos\phi \cdot e'_y)^2}{2R}\right) \tag{2.3.12}$$

where

$$R = |e'_x \sin\phi \cdot \cos\omega_s t + e'_z \sin\omega_s t| \tag{2.3.13}$$

and $(\cos\phi \cdot e'_y)^2$ is a small term due to the small e'_y component of the wave polarisation. In obtaining (2.3.12) we used $\psi_a = \frac{\pi}{2}$. Since both e'_x and e'_z are real, we can rewrite the expression for R as

$$R = R_0 |\sin(\omega_s t + \gamma)| \tag{2.3.14}$$

where $R_0 = \left((e'_x \sin\phi)^2 + (e'_z)^2\right)^{\frac{1}{2}}$ and γ is given by

$$\tan\gamma = \frac{e'_x \sin\phi}{e'_z} \tag{2.3.15}$$

The expression for R in the form of (2.3.14) is useful, since some qualitative features of the fading pattern are brought out. The depth of fading is defined as the ratio of the maximum and minimum values of $\mathcal{U}_m$. From (2.3.12), this ratio can be estimated as

$$\frac{\mathcal{U}_{max}}{\mathcal{U}_{min}} \simeq \frac{2R_0^2}{(e_y' \cos\phi)^2} \qquad (2.3.16)$$

We first note that if the wave vector is very close to the resonance cone, then the quantity $(e_y' \cos\phi)^2$ is small, and thus the variation of $\mathcal{U}_m$ is defined primarily by the R term, resulting in deep fading of the voltage due to the antenna spin. The closer the wave vector is to the resonance cone, the smaller the value of $(e_y' \cos\phi)^2$ is, and the deeper the fading must be as observed at the antenna terminals. Therefore, near the resonance cone, the wave normal angle ψ directly affects the observed modulation depth. In a contrast to ψ, the azimuthal angle ϕ affects both the phase of fading (see expression (2.3.16) for γ) and the depth of fading. Measurements of both the depth and the phase of fading allows the determination of the wave vector directions ϕ and ψ.

The above derivation of (2.3.15) is valid only for a plane wave. We complete this section by estimating the applicability of the method to the analysis of wave packets consisting of individual components propagating in different directions in the space plasma. For the sake of simplicity, we consider just two plane waves with equal amplitudes and wave normal angles, propagating with different azimuthal angles ϕ_1 and ϕ_2. Following the same procedure as above, the derivation for the fading in the presence of two waves yields

$$\frac{\mathcal{U}_{1+2,max}}{\mathcal{U}_{1+2,min}} \simeq \frac{2R_{1+2}^2}{((\cos\phi_1 + \cos\phi_2)e_y')^2} \qquad (2.3.17)$$

where

$$R_{1+2} = \left((e_x'(\sin\phi_1 + \sin\phi_2))^2 + (e_z')^2\right)^{\frac{1}{2}} \qquad (2.3.18)$$

Analysis of (2.3.17) and (2.3.18) shows that in the case of two propagating waves
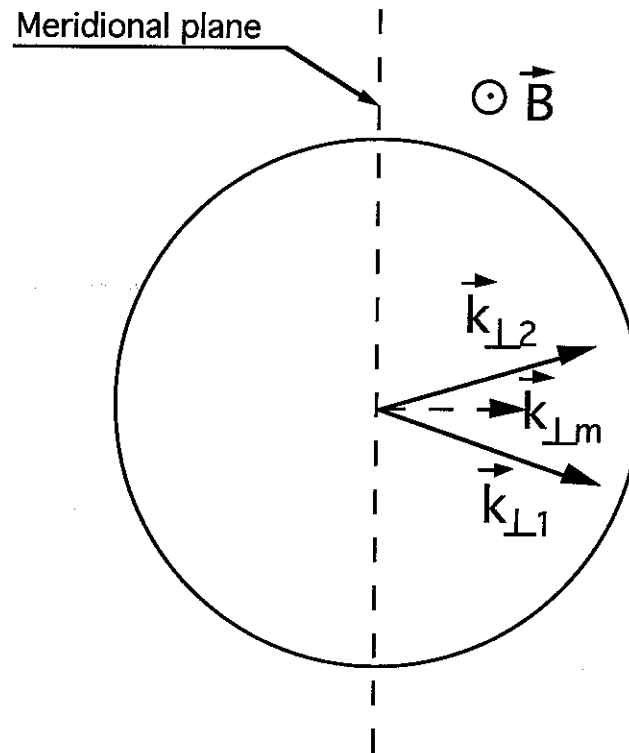
Fig. 2.3. The sketch of the wave vector orientation from the single wave analysis $k_{\perp m}$ as results from data corresponding to two waves with wave vectors $k_{\perp 1}$ and $k_{\perp 2}$. The measured wave vector direction is generally in the same direction, but with a smaller wave normal angle (as indicated by a $\vec{k}$ vector of smaller magnitude).

with azimuthal orientation almost perpendicular to the magnetic meridional plane, the single wave analysis gives the value of the average wave vector direction azimuthally as generally the same direction, but with a somewhat smaller wave normal angle. This situation is sketched in Figure 2.3, where the actual and the calculated wave normals are shown. Thus, the single wave analysis may result in somewhat underestimated wave normal angles.

2.4   EXTRACTION OF THE WAVE VECTOR DIRECTION FROM EXPERIMENTAL DATA

2.4.1   Satellite antenna orientation

Equation (2.3.11) for the voltage at the antenna terminals is derived under the assumption that time $t = 0$ corresponds to the antenna orientation perpendicular to the ambient magnetic field. The necessary information on the instanteneous three-dimensional orientation of the DE-1 satellite can be retrieved from the satellite ephemeris database, using the OAREAD subroutine. The output of the OAREAD subroutine contains an array of variables describing satellite position and orientation, the local earth magnetic field intensity and direction, etc. Though neither of these parameters directly gives an angle between the satellite antenna orientation and the Earth's magnetic field, the $t = 0$ moment can be unambiguously determined from other available parameters. Some of the OAREAD parameters in GEI coordinates [*Shawhan et al.*, 1981] are listed in Table 2.1.

OAREAD Parameters		
Parameter	element #	Description
$\vec{V}$	26–28	Satellite velocity vector
$\vec{M}$	68-70	Angular momentum
$\vec{B}$	42-44	Magnetic field
$\vec{N}$	8-10	Unit vector normal to the satellite orbit plane
Ψ	71	The angle between the X-axis of the satellite and $\vec{V}$

Table 2.1. Parameters of the ephemeris of the DE-1 satellite used for data analysis.

The so-called X-axis of the DE-1 satellite lies in the satellite spin plane [*Shawhan et al.*, 1981], and forms an angle of 130° with the dipole electric antenna. We use the parameters listed in Table 2.1 to determine the X-axis orientation. We start from two obvious equations for $\vec{X}$

$$\vec{X} \cdot \vec{M} = 0 \tag{2.4.1}$$

$$\left(\vec{X} \times \vec{V}\right)^2 = X^2 V^2 \sin^2 \Psi \tag{2.4.2}$$

The latter equation readily results from the definition of angle Ψ. The two equations (2.4.1) and (2.4.2) contain three unknown components of $\vec{X}$, providing an infinite number of solutions for $\vec{X}$. In fact, (2.4.1) and (2.4.2) determine only the orientation of $\vec{X}$, but not its magnitude, so that different solutions for $\vec{X}$ have the same orientation and different magnitudes. Since we are interested only in the orientation of $\vec{X}$, we can find any of the solutions of equations (2.4.1),(2.4.2) by arbitrarily selecting the magnitude of $\vec{X}$ or any of the three components of $\vec{X}$. In our calculations below we let $X_z = 1$ to find

$$X_x M_x + X_y M_y = -M_z \tag{2.4.3}$$

$$(V_y - V_z X_y)^2 + (V_x - V_z X_x)^2 + (V_x X_y - V_y X_x)^2 = (X_x^2 + X_y^2 + 1)V^2 \sin^2 \Psi \tag{2.4.4}$$

These two equations yield a quadratic equation for the X_y component, the remaining X_x component being defined through X_y;

$$AX_y^2 + BX_y + C = 0 \tag{2.4.5}$$

$$X_x = -\frac{M_z}{M_x} - X_y \frac{M_y}{M_x} \tag{2.4.6}$$

where

$$A = V_z^2(1 + \frac{M_y^2}{M_x^2}) + (V_x + V_y \frac{M_y}{M_x})^2 - (1 + \frac{M_y^2}{M_x^2})V^2 \sin^2 \Psi \tag{2.4.7}$$

$$B = 2\left(-V_y V_z + (V_x + V_z \frac{M_z}{M_x})V_z \frac{M_y}{M_x} + V_y \frac{M_z}{M_x}(V_x + V_y \frac{M_y}{M_x}) - \frac{M_z M_y}{M_x^2}V^2 \sin \Psi\right) \quad (2.4.8)$$

$$C = V_y^2 + (V_x + V_z \frac{M_z}{M_x})^2 + V_y^2 \frac{M_z^2}{M_x^2} - (1 + \frac{M_z^2}{M_x^2})V^2 \sin^2 \Psi \qquad (2.4.9)$$

Since equation (2.4.5) for X_y has two roots, it is not possible to determine $\vec{X}$ unambiguously from a single set of values of $\vec{V}, \vec{M}$. Assuming that we retrieve two solutions for $\vec{X}$, the algorithm described below is used to determine the correct solution.

Analysis shows that the two solutions for the vector $\vec{X}$ correspond to two opposite directions of the satellite spin. Since the actual direction of the satellite spin is known, we can extrapolate both solutions for $\vec{X}$ in time to get a sequence of values of $\vec{X}$ corresponding to different instances of time, so that the two solutions for $\vec{X}$ at $t = t_0$ would generate two time sequence of $\vec{X}$ values. One of these time sequences would correspond to the actual revolution of the $\vec{X}$ vector, another one corresponding to the incorrect solution of equation (2.4.5).

For all time instances in these two sequences, we can again retrieve information from the satellite ephemeris database to get two additional values for $\vec{X}$, resulting in four time sequences of possible $\vec{X}$ values: (i) two sequences resulting from the evolution of the solutions of (2.4.5) from $t = t_0$ to $t > t_0$, and (ii) two sequences as determined from the satellite ephemeris database at every time moment $t > t_0$. Within each of these pair of time sequences one sequence describes the actual satellite spin, another one being incorrect. If we plot all four time sequences for $\vec{X}$ on the same figure, we would see that the two "true" time sequences for $\vec{X}$ would match, while the values for the two other "incorrect" sequences would be widely scattered. An example of the four time sequences of X_x derived as described above is shown in Figure 2.4. We see that the exact match of the two "true" sequences unambiguously determine the actual X_x value. This method allows the identification of the correct solution of equation (2.4.5) to be used in our data analysis.

After we determine the correct solution for the satellite X-axis orientation, we can
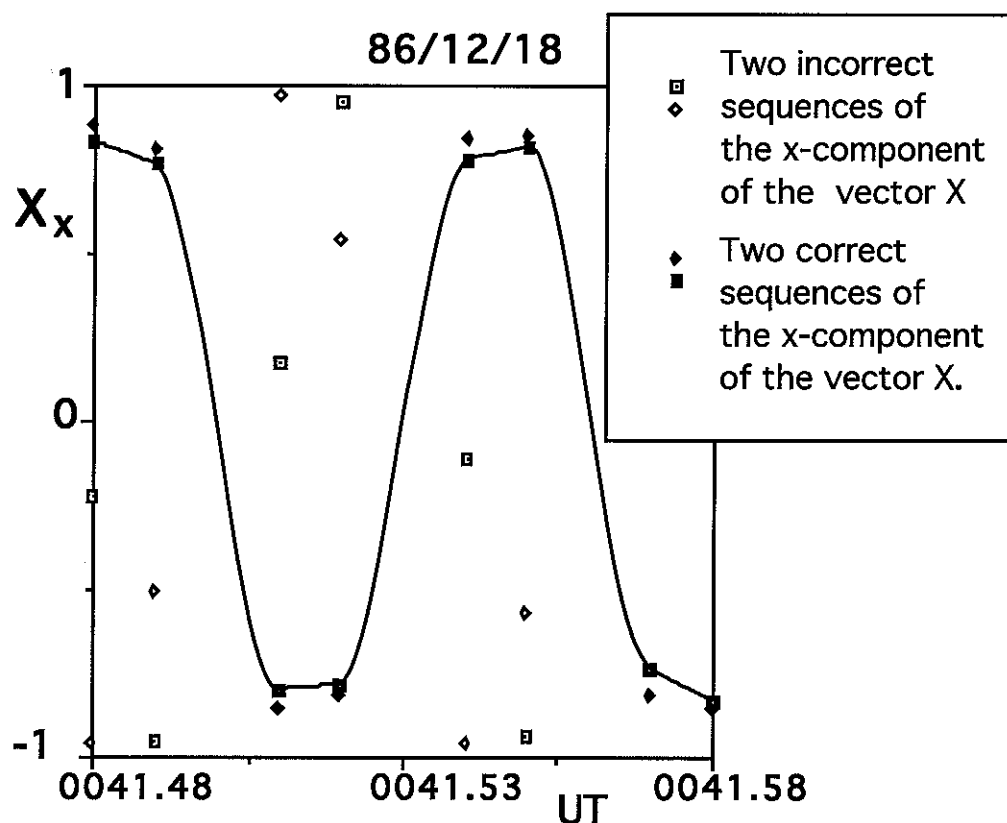
Fig. 2.4. **Four time sequences of the** x **component of** $\vec{X}$**.** Values of $\vec{X}$ result from (i) advancement of two solutions of equation (2.4.5) from $t = 0041.00$ UT to $0041.58 > t > 0041.48$ UT and (ii) solution of equation (2.4.5) at different time moments in the time interval of $0041.58 > t > 0041.48$ UT. Note that two of the four solutions (connected by the curve) nearly coincide, which indicate that they represent the actual orientation of $\vec{X}$.

easily determine the instant of time when the X-axis of the satellite was perpendicular to the Earth's magnetic field by computing the scalar product $\vec{X} \cdot \vec{B}$ and plotting it versus time and noting the intersections with the horizontal axis as the times corresponding to $\vec{X} \perp \vec{B}$ moments. Finally, we note that since the electric dipole antenna forms an angle of 130° with the X-axis of the satellite, the antenna becomes perpendicular to $\vec{B}$ ~0.85 seconds before the time when $\vec{X} \perp \vec{B}$ (accounting for 1.03 rad/s angular velocity of the satellite spin).

In addition to determining the $t = 0$ moment, the equations for the wave normal angle require the knowledge of the satellite spin axis orientation with respect to the magnetic field. The angle ψ_a between the spin axis and $\vec{B}$ is readily calculable, since both the angular momentum vector (aligned along the spin axis) and magnetic field vector are available as OAREAD output parameters (see Table 2.1 above). Therefore, DE-1 ephemeris database provides all the necessary information on satellite position and orientation that are needed in our wave vector direction analysis.

2.4.2   Numerical determination of the wave vector direction

For given plasma parameters and angles ψ and β, equation (2.3.11) defines the envelope of fading of the wave intensity at the frequency ω. The fading pattern is observed as a series of voltage values $U_{ex,j}$ measured at given instants of time t_j. The goal of our analysis is to determine values of the wave vector orientation angles ψ and β which provide the best fit to the experiment. Mathematically, we minimize the value of the function Φ representing the mean squared difference between the theoretical fading values $U_j = U(t_j)$ and the experimentally observed values $U_{ex,j} = U_{ex}(t_j)$ at times t_j for $j = 1, 2, ..., j_{max}$. The function Φ is defined as;

$$\Phi(C, \psi, \beta; \omega, \omega_p, \omega_H) = \sum_{j=1}^{j_{max}} (20 \log_{10} U_j - 20 \log_{10} U_{ex,j} - C)^2 \qquad (2.4.10)$$

where

$$U_j = \mathcal{U}_m(t_j) \tag{2.4.11}$$

and $\mathcal{U}_m(t)$ is defined by (2.3.11), C is an unknown normalization constant, $U_{ex,j}$ is the field intensity observed at times t_j in a frequency window centered at ω, and the values of the parameters ω, ω_p and ω_H are assumed to be known. The global minimum value of Φ corresponds to the closest agreement between theoretical values U_j and experimental ones $U_{ex,j}$, in the mean squared sense. This minimum can be found by numerical methods for any set of experimental data $U_{ex,j}$. In our numerical scheme we use the diffusive equilibrium model [*Angerami and Thomas,* 1964] for the electron plasma density (which determines ω_p), and the centered tilted dipole field model for the magnetic field (which determines ω_H).

The value of C which provides a local minimum of Φ for fixed values of ψ and β can be obtained from $\frac{\partial \Phi}{\partial C} = 0$ as;

$$C = \frac{1}{j_{max}} \sum_{j=1}^{j_{max}} (20 \log_{10} U_j - 20 \log_{10} U_{ex,j}) \tag{2.4.12}$$

In view of the above, the orientation of the wave vector can be determined from experimental data by finding the values of ψ and β which provide the minimum value of Φ, the normalization constant C being given by (2.4.12) and U_j being defined by (2.4.11) and (2.3.11).

This method of determining the wave vector direction is different from that used by *Sonwalkar and Inan* [1986; 1988], since we take into account not only the depth and the phase, but the entire shape of the fading pattern. Thus, for a large number of experimentally observed values j_{max}, our method averages random fluctuations in the signal amplitude, and leads to better accuracy in the determination of the wave normal angle. This improved algorithm is particularly important in our study of nonducted

whistlers (see below) in which a large number of individual whistler magnitudes was used to statistically extract the average wave vector direction.

2.4.3   Numerical methods and error margins

Special consideration should be given to the numerical method of solution of equation (2.3.11). Any numerical method for finding the minimum value of a function employs an algorithm to evaluate the function itself. In our case, we need to evaluate Φ as given in (2.4.10), in terms of U_j, which in turn are functions of the polarisation unit vector $\vec{e}$ as defined by (2.3.5). In the latter equation, k_j and ω must satisfy the dispersion equation for the magnetized plasma. Therefore, to evaluate the function Φ, one should first solve the dispersion equation. In our analysis, the wave frequency is known, and the orientation of the wave vector is to be determined so that we can solve the dispersion equation for one component of the wave vector only, namely, for $k_\parallel$, by the modified Newton method [e.g., *Press et al.*, 1992].

Most numerical methods for finding a minimum of a function use algorithms for calculating partial derivatives of this function with respect to its variables. Typically, such derivatives are evaluated numerically, by subtracting computed values of the function in closely spaced points. However, in our analysis the numerical estimation of the derivatives is not appropriate, since subtraction of Φ values at closely spaced points is very sensitive to small errors in the values of the function. Since the function Φ is evaluated as a result of the solution of the dispersion equation, a small random error is introduced for every computed Φ value, with the magnitude of the error corresponding to the numerical precision of the solution. This small error is magnified significantly when derivatives of Φ are calculated. In our calculations, we avoided numerical evaluation of the derivatives of Φ and used the Nelder-Meade method, which is much less sensitive to errors in calculating the function Φ [*Himmelblau*, 1972].

Another source of errors in evaluating Φ is linked with experimental errors in the
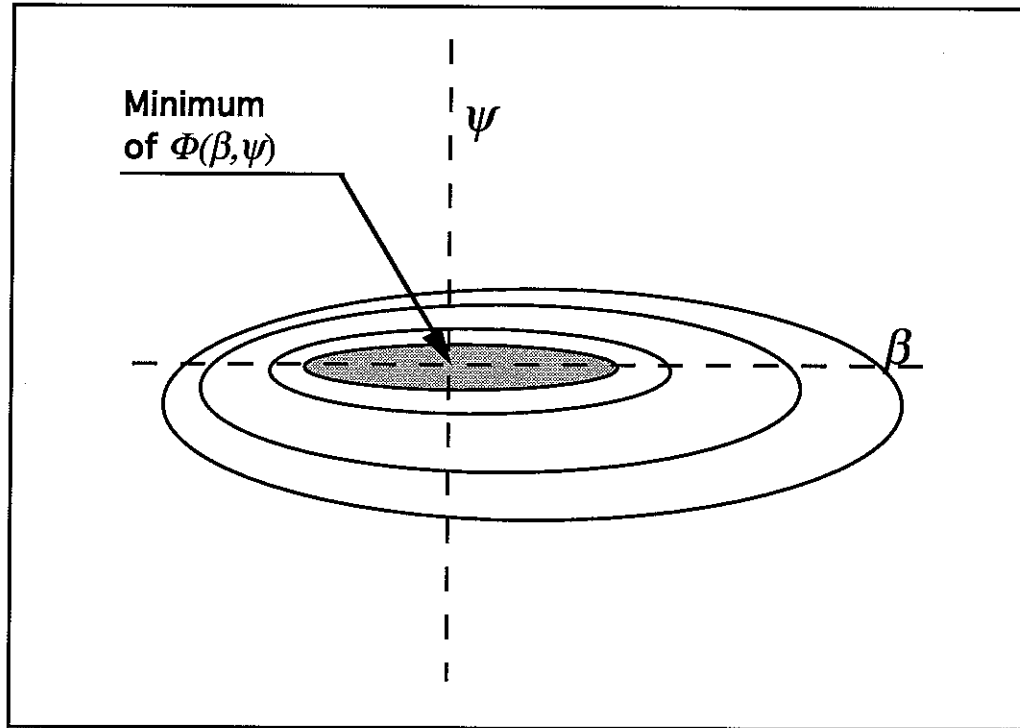
Fig. 2.5. Sketch of contours of values of Φ with respect to the wave normal angle ψ and the azimuthal angle β. The exact location of the minimum is shown by the arrow. The shaded area sketches the possible margin of errors in the theoretical determination of the minimum of Φ. Note that the margin of errors in determining β is larger than that for ψ.

measurements and with the uncertainty in plasma parameters at the point of measurement. To estimate roughly the error in the wave vector direction due to uncertainties in measurement or plasma parameters, we considered the behavior of Φ near the minimum. Contour plots of Φ with respect to the wave normal angle and the azimuthal angle are given in Figure 2.5. We see that the minimum of Φ is much more elongated in the β direction than in the ψ direction, meaning that any error in evaluating Φ would probably shift the location of its minimum mainly in the β direction, rather than in the ψ direction. On this basis, the margin of errors in determining the wave normal angle ψ is believed to be smaller compared to that of the azimuthal angle β. In practice, it is simpler to estimate the margin of errors for the wave vector direction by performing test calculations with

slightly different values of plasma parameters and slightly distorted experimental values. This approach confirms the lower margin of errors for the wave normal angle, and allows us to numerically estimate the margin of errors in each case analyzed.

2.5   WAVE VECTOR DIRECTIONS OF PLASMASPHERIC HISS AS DETERMINED FROM DE-1 DATA

In this section we discuss the results of the application of the method developed above to the measurement of hiss wave vector directions at different locations within a broad range of L-shells ($3 < L < 5$). In individual cases reported so far, wave normal angles for plasmaspheric hiss have been measured to be generally high [*Lefeuvre et al.*, 1983; *Sonwalkar and Inan*, 1988; *Storey et al.*, 1991]. *Storey et al.*, [1991] reported wave distribution function analyses in which one, two or three maxima were observed for different wave frequencies and satellite locations. In *Sonwalkar and Inan* [1988] the wave vector of plasmaspheric hiss was found to be at a high angle with respect to the meridional plane, as in some cases presented below. Our results constitute the first comprehensive measurement of hiss wave vector directions at multiple locations within the plasmasphere.

The cases considered here for hiss wave normal analysis were chosen primarily to cover a broad range of L shells. In order to facilitate the type of analysis described in previous sections it was necessary to have DE-1 data available in wideband form acquired by the Linear Wave Receiver (LWR) instrument [*Shawhan et al.*, 1981]. As noted previously [*Sonwalkar and Inan*, 1988] this receiver maintains constant gain which makes it possible to quantitatively measure the spin fading pattern. Due to LWR data availability, the latitudinal locations of the selected cases were generally limited to the region near the magnetic equator ($|\lambda_m| < 30^o$). We analyzed 22 cases, providing sufficient data to make conclusions on the general trends of hiss wave vector directions. The parameters of the cases studied are summarized in Table 2.2.
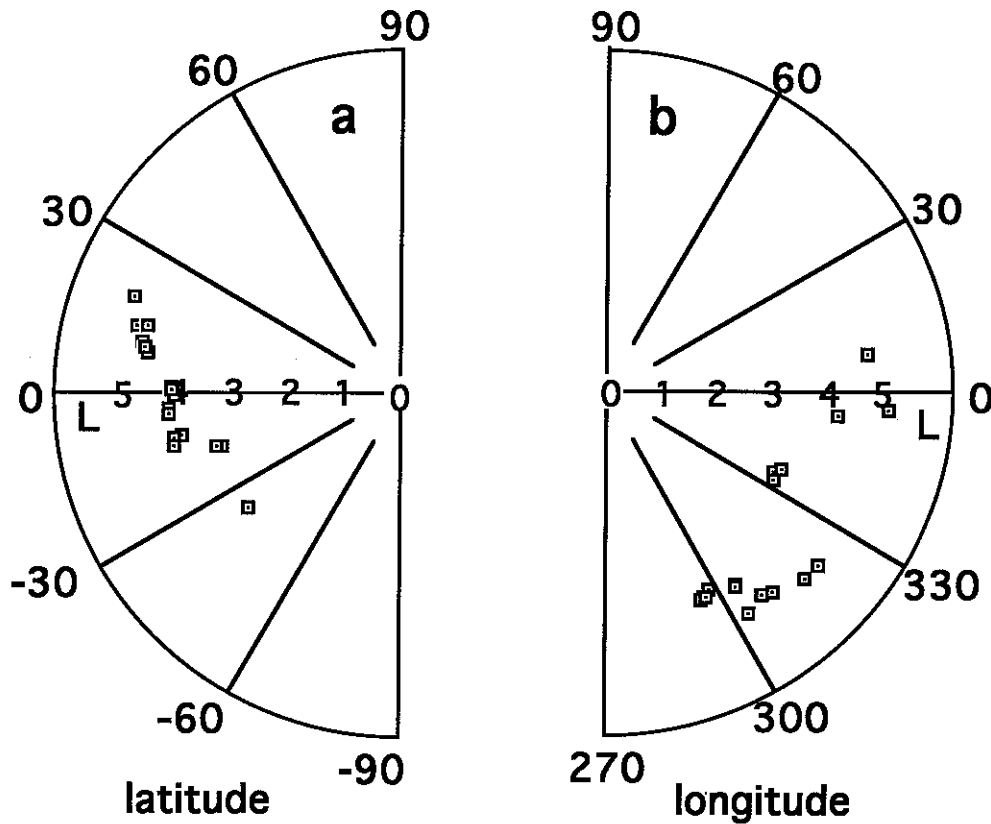
Fig. 2.6. L **values versus magnetic latitude (a) and magnetic longitude (b) of the locations of hiss wave vector direction measurements.** Measurements were made within the broad range of L-shells (approximately $3 < L < 5$), though in a limited range of magnetic longitude.

Figures 2.6 shows L values and geomagnetic latitude and longitude of the DE-1 satellite locations in the 22 cases studied. Measurements were made within a broad range of L-shells (approximately $3 < L < 5$), but in a rather limited range of magnetic longitudes, due to availability of LWR data, which was acquired primarily in the vicinity of the North American continent for coordinated experiments with the Siple Station, Antarctica transmitter [*Rastani et al.*, 1985] .

Figure 2.7 shows the results of our analyses of the distribution of the perpendicular
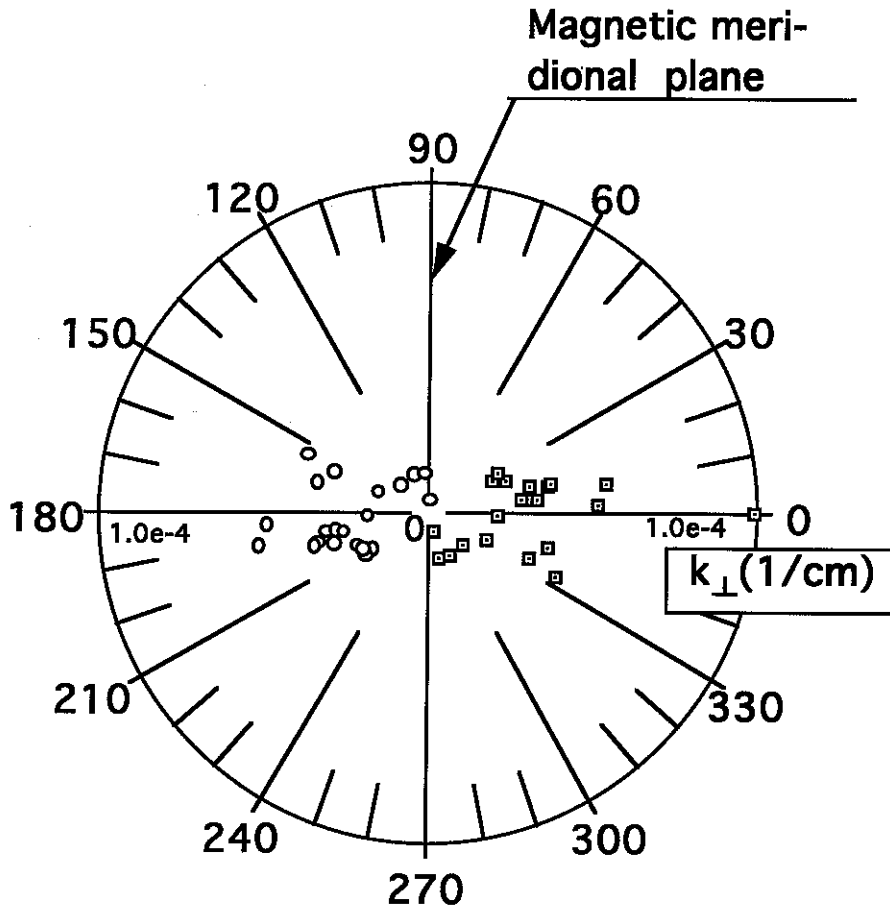
Fig. 2.7. Perpendicular components of the wave vectors of plasmaspheric hiss. Note that hiss often propagates at a large angle with respect to the meridional plane.

components of the wave vectors* of plasmaspheric hiss. Since our method of wave normal analysis entails a 180° ambiguity in ψ and does not resolve between waves propagating with wave vectors $\vec{k}$ and $-\vec{k}$, any of the measured wave vectors may correspond to either the actual wave vector of hiss, or its image counterpart reflected through the origin. In Figure 2.7, measured values of the wave vector are shown as squares, and reflected values are shown by circles for reference. In the following we assume that actual orientations of the wave vectors are randomly split between the measured and "reflected" values.

---

* Numerical values of the wave vectors and frequency are given in rad/sec throughout this dissertation.
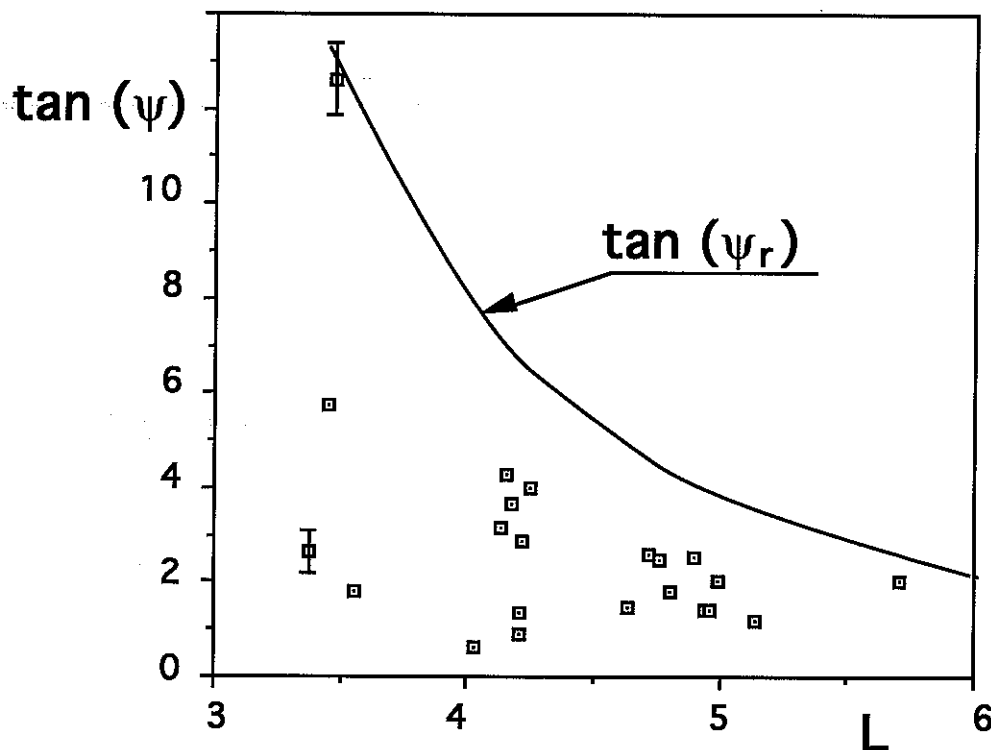
Fig. 2.8. The tangent of hiss wave normal angles ψ as determined from 22 measurements of hiss wave vector direction. For comparison, the tangent of the resonance cone angle ψ_r is shown by a curve. The measured wave normal angles are generally high, ranging from 45° (which corresponds to $\tan\psi = 1$) to the vicinity of the resonance cone $\psi \simeq \psi_r$.

We see from Figure 2.7 that hiss wave vectors span a broad range of azimuthal angles, covering virtually the entire 360° of azimuth. As we will see below, this result is in qualitative agreement with our hypothesis of hiss generation by multiply reflected whistlers originating in lightning. According to this model, plasmaspheric hiss generation is due to the accumulation of wave energy from a large amount of non-ducted whistlers, bouncing back and forth in the magnetosphere. If whistlers are produced by lightning from different thunderstorm centers, they would be expected to have different magnitude and orientation of their wave vectors as measured at the observation point in the magnetosphere. This concept is investigated in more detail in the next chapter, where it is shown that for hiss formation at high wave normal angles (i.e., large $k_\perp$) and at

frequencies considerably higher than the local lower hybrid frequency, the wave normal angle of hiss is likely to have a considerable azimuthal component. This trend is clearly visible in Figure 2.7.

Figure 2.8 shows the tangent of the measured wave normal angle ψ as a function of L-shell. For comparison, the tangent of the resonance cone angle at the geomagnetic equator (as calculated from a dipole model) is shown by a curve. We see from the figure that the wave normal angles observed are generally high, ranging from 45° to the vicinity of the resonance cone angle $\psi \simeq \psi_r$.

Data presented in this section represent 22 cases spanning a large range of L-shell, providing solid evidence that magnetospheric hiss typically propagates at large wave normal angles. As we mentioned in Chapter 1, this is in contradiction with the models of hiss generation by energetic electrons [*Church and Thorne*, 1983]. Therefore, our measurements show the need for a mechanism for hiss generation which would account for high wave normal angles of hiss. These and other experimental data (in particular, hiss association with whistlers as observed by [*Sonwalkar and Inan*, 1989]) serve as the basis for our new model of hiss generation by lightning generated whistlers, which is presented in Chapter 3.

Table 2.1.

yy/mm/dd	UT	λ (deg)	ϕ (deg)	MLT	λ_m (deg)	ϕ_m (deg)	L	ΣK_p	k_x (cm^{-1})	$k_{\|}$ (cm^{-1})	$\tan(\psi)$	β (deg)
86/12/20	01:29	-16	-134	16:30	-11	-62	4.03	15	9.18e-6	1.47e-5	6.22e-1	239
86/12/04	02:09	-18	-129	17:45	-11	-56	4.21	14	1.33e-5	1.48e-5	8.97e-1	293
87/01/09	20:09	9	-74	14:52	20	-4	5.14	17	1.74e-5	1.48e-5	1.17e+0	260
86/12/04	22:38	-16	-76	17:27	-4	-6	4.21	14	1.97e-5	1.45e-5	1.35e+0	391
86/12/02	01:00	5	-108	17:34	14	-39	4.96	16	2.28e-5	1.61e-5	1.41e+0	388
86/12/10	00:50	6	-112	16:57	14	-43	4.94	20	2.32e-5	1.63e-5	1.42e+0	386
86/12/20	00:37	2	-121	16:14	9	-52	4.64	15	2.31e-5	1.57e-5	1.47e+0	395
86/12/28	22:10						3.55		1.61e-5	8.97e-6	1.79e+0	273
86/12/02	21:52	0.0	-62	17:36	11	8	4.8	16	3.27e-5	1.80e-5	1.81e+0	366
86/12/29	23:52						4.99		2.91e-5	1.44e-5	2.01e+0	367
86/12/28	20:52						5.71		2.70e-5	1.34e-5	2.02e+0	368
87/01/08	23:39	9	-124	14:41	15	-57	4.76	15	3.47e-5	1.38e-5	2.50e+0	329
86/12/22	00:17						4.9e		3.75e-5	1.47e-5	2.53e+0	373
86/12/18	00:41	3	-119	16:22	10	-50	4.72	10	3.94e-5	1.53e-5	2.57e+0	339
87/01/07	21:50	-27	-96	15:06	-17	-25	3.38	9	1.78e-5	6.75e-6	2.64e+0	324
86/12/02	22:10	-20	-129	17:57	-13	-56	4.22	16	3.07e-5	1.07e-5	2.85e+0	375
87/01/05	00:27	-6	-135	15:09	-1	-64	4.13	5	3.90e-5	1.23e-5	3.16e+0	374
87/01/09	00:12	-3	-135	14:50	1	-65	4.17	17	4.62e-5	1.25e-5	3.68e+0	328
86/12/10	01:40	-11	-127	17:11	-5	-56	4.25	20	5.52e-5	1.37e-5	4.01e+0	362
87/01/07	00:15	-4	-134	14:59	1	-64	4.15	9	5.85e-5	1.37e-5	4.26e+0	369
87/01/09	22:02	-47	-103	15:11	-37	-28	3.45	17	1.81e-5	3.15e-6	5.7e+0	353
87/01/05	21:46	-27	-95	15:14	-16	-24	3.47	5	1.19e-4	9.48e-6	1.26e+1	359

2.6 SIMULTANEOUS MEASUREMENTS OF WAVE VECTOR DIRECTIONS OF HISS AND WHISTLERS

In this section we provide a detailed analysis of one particular case of wave data from the DE-1 satellite when plasmaspheric hiss and discrete whistlers were observed simultaneously. In this case, it was possible to measure for the first time the average wave vector direction of whistlers by using statistical methods as described in Section 2.2. The use of statistical methods for the measurement of whistler wave vector direction was facilitated due to the relatively high rate of whistlers observed in this case, providing a sufficient amount of whistler data during a short period of observation and sufficient sampling of whistlers during a single spin period. The results of the measurements reported here are theoretically interpreted in Chapter 3 and serve as new experimental evidence which supports our proposed model of hiss generation by multiply reflecting nonducted whistlers.

The data analyzed covers the time interval from 2104 UT to 2110 UT on March 24, 1982. At the time shown, the satellite was at $L = 3.8$, with a geographic latitude and longitude of $\lambda_g = -12^o$ and $\phi_g = 23^o$, and magnetic latitude of $\lambda = -26^o$. The satellite orbit plane was close to the meridional plane. The satellite spin period was ~ 6.09 s, the spin axis being perpendicular to the orbit plane. Due to the satellite spin the measured intensity of whistler waves should be subject to periodical variation, as was conceptually illustrated in Figure 2.1.

The wave data were once again obtained by the Linear Wave Receiver [*Shawhan et al.*, 1981]. A representative 10 second period of the data is presented in Figure 2.9. Whistlers ($f > 3$ kHz), as well as plasmaspheric hiss ($f < 3.5$ kHz) with spectra similar to that shown in Figure 2.9 were observed from 2104 UT to 2110 UT. Although individual whistler intensities vary, the periodic change in the average amplitude associated with the satellite spin is clearly visible in Figure 2.9. A narrow band emission seen near 4 kHz occasionally appeared during the period of observation. This emission band exhibited spin fading similar to that for whistlers and hiss and is similar in nature to
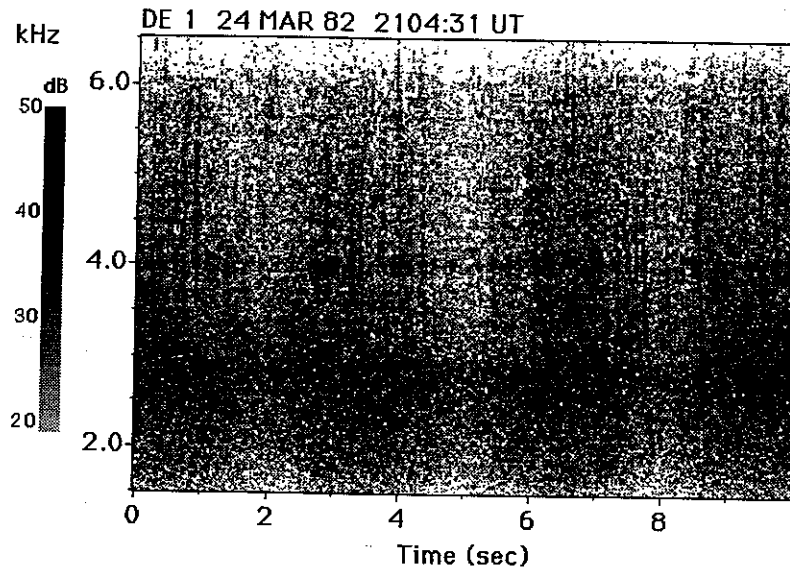
Fig. 2.9. **A spectrogram of the data from the linear wave receiver at the DE-1 satellite.** The satellite was at $L = 3.8$, geographic latitude and longitude of $\lambda_g = -12°$ and $\phi_g = 23°$, and magnetic latitude of $\lambda = -26°$. Whistlers ($f > 3$ kHz), as well as plasmaspheric hiss ($f < 3.5$ kHz) are seen on the spectrogram.

narrowband emissions previously seen in DE-1 and ISEE-1 satellite data [*V. Sonwalkar, private communication*, 1993]. The wave normal analysis of whistlers at 4.5 and 3.5 kHz and hiss at 3.5 and 2.5 kHz is not affected by the presence of this narrow band signal at $\sim$4.0 kHz. Figure 2.9 shows that the hiss intensity exhibits a drop at frequencies above $\sim$2.9 kHz. A possible mechanism of this cutoff is discussed at the end of Section 3.4.

To determine the average wave normal angle of whistlers, we measured whistler amplitudes for 147 identified whistlers in the data at $f = 4.5$ kHz and for 133 whistlers at $f = 3.5$ kHz. Figure 2.10 shows whistler amplitudes at 4.5 kHz plotted versus the satellite
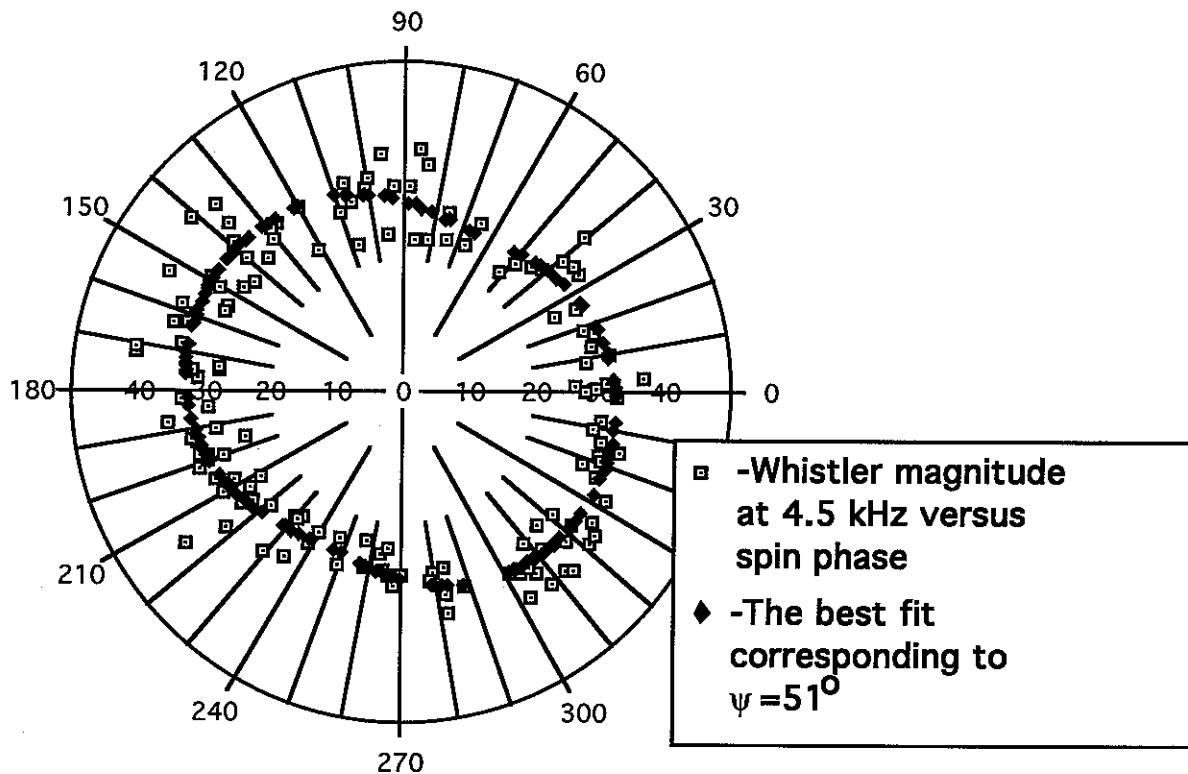
Fig. 2.10. Amplitudes at f = 4.5 kHz of 147 individual whistlers measured during
the time period from 2104 UT to 2110 UT on March 24, 1982 are shown as squares
on a polar plot of radial distance (in dB) versus the satellite spin phase. The zero
angle corresponds to the dipole electric antenna orientation perpendicular to the magnetic
field. The theoretically computed best fit values are shown by diamonds, corresponding
to the average wave vector direction of whistlers with an angle of ψ=51° with respect to
the magnetic field and at $90° - \beta$=20° angle with the magnetic meridional plane.

spin phase, with zero phase corresponding to the satellite electric dipole antenna being perpendicular to the Earth's magnetic field. Individual whistler intensities exhibit ~10 dB spread for any fixed satellite spin phase, but the locus of all the measured intensities describes an ellipse as seen in Figure 2.10.

Figure 2.11 shows whistler amplitudes at 3.5 kHz plotted in a similar way. There is more spread in the distribution of whistler intensities for this frequency, perhaps due to the relatively high level of the background hiss, which introduced error in our measurements. An elliptical shape is nevertheless evident.

Figures 2.12 and 2.13 show hiss amplitude versus the satellite spin phase at frequencies 3.5 kHz and 2.5 kHz respectively. During these observations, the Linear Wave Receiver was operating in 3-6 kHz mode, so that in measuring intensities of signals below 3 kHz the filter roll-off characteristics (~30 dB/kHz in the 2.2 to 3.0 kHz range) had to be taken into account. However, in the case of wave normal measurements, only relative changes in the signal levels as a function of the satellite spin are important and therefore constant offset in gain due to the filter roll off has little effect on our results, especially since the hiss emission is quite intense at 2.5 kHz.

An important feature of the data presented in Figure 2.9 is that nearly all whistlers have the same dispersion pattern corresponding to a direct path from the source to the satellite without any magnetospheric reflections (only 5% of observed whistlers exhibited larger dispersion). Based on this observation, we assume that most whistlers have approximately the same wave parameters, including their wave normal angles.

Using the method described above, the average wave normal angles (ψ) of whistlers shown in Figures 2.10 and 2.11 were determined to be ~51° at $f = 4.5$ kHz and ~60° at $f = 3.5$ kHz. The corresponding theoretical best fit (as defined in Section 2.4.2) values E_j versus the satellite phase spin are shown in Figures 2.10 and 2.11 as dots on top of experimental values represented by squares. The whistler intensity measurement at 3.5 kHz (Figure 2.11) exhibited a higher level of background noise, so that it was not
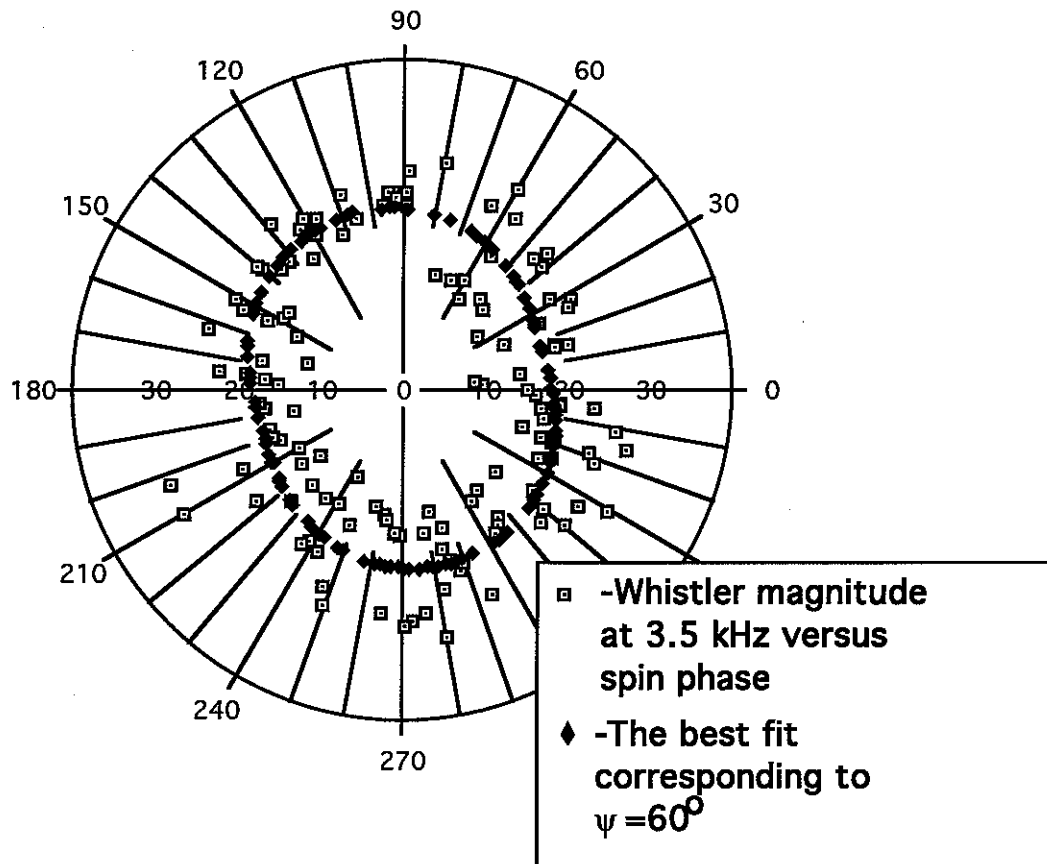
Fig. 2.11. Amplitudes of 133 individual whistlers measured at $f = 3.5$ **kHz during the same time period as in Figure 2.9 are shown in same format as in Figure 2.9.** The best fit values to the experimentally observed amplitudes correspond to the average wave vector direction of whistlers with an angle of $\psi=60°$ with respect to the magnetic field. Due to higher noise level at 3.5 kHz, it was not possible to determine the azimuthal angle between the wave vector and the meridional plane.
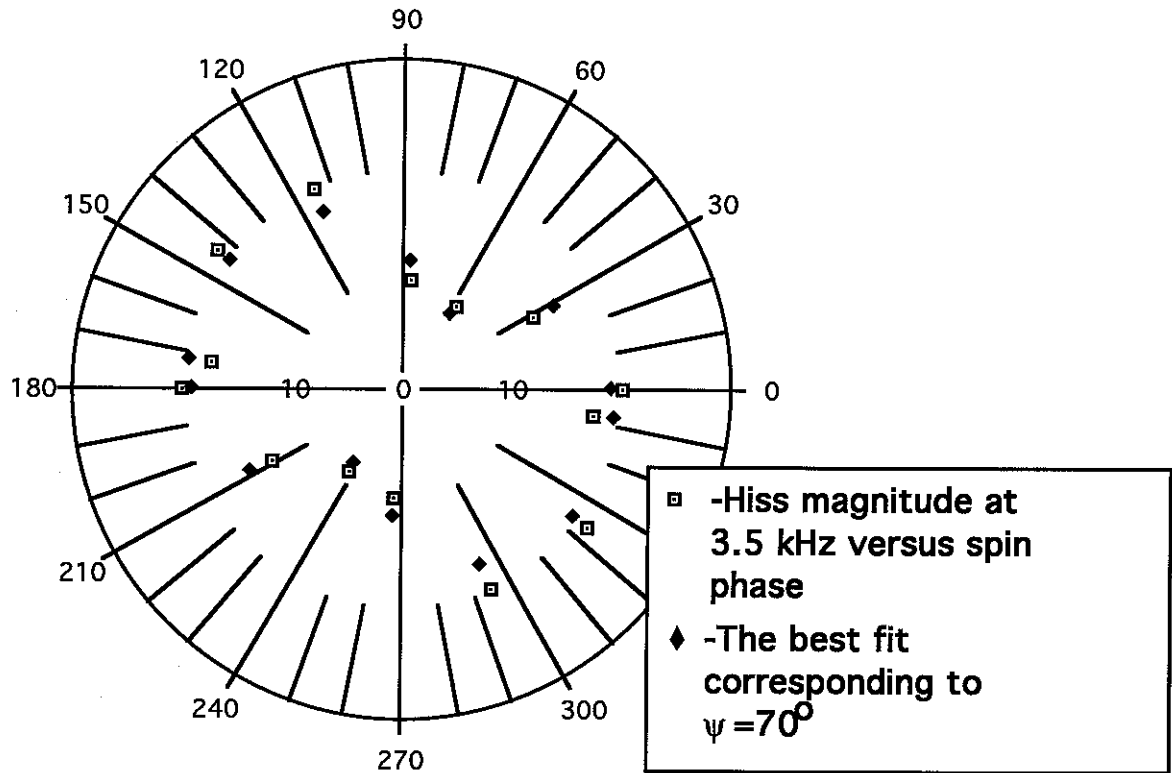
Fig. 2.12. Amplitudes of hiss measured at $f = 3.5$ **kHz during the same time period as in Figures 2.9, 2.10 shown in the same format.** The best fit values to the experimentally observed amplitudes correspond to the average wave vector of hiss with an angle of $\psi=70^o$ with respect to the magnetic field, with the perpendicular component tilted at the angle of $\sim80^o$ with respect to the magnetic meridional plane.

possible to accurately measure the angle between the wave vector and the meridional plane ($\sim (90^o - \beta)$ in Figure 2.4). However, for 4.5 kHz the whistler wave vector was determined to be at an angle of $(90^o - \beta) \sim20^o$ with respect to the meridional plane.

The measured wave normal angle of whistlers can be compared to the wave normal angle of plasmaspheric hiss, which was measured to be $\sim77^o$ at $f = 2.5$ kHz and $\sim70^o$ at $f = 3.5$ kHz, using the same method. Figures 2.12 and 2.13 show computed best fit values at 3.5 kHz and 2.5 kHz respectively together with the measured values, in a way similar
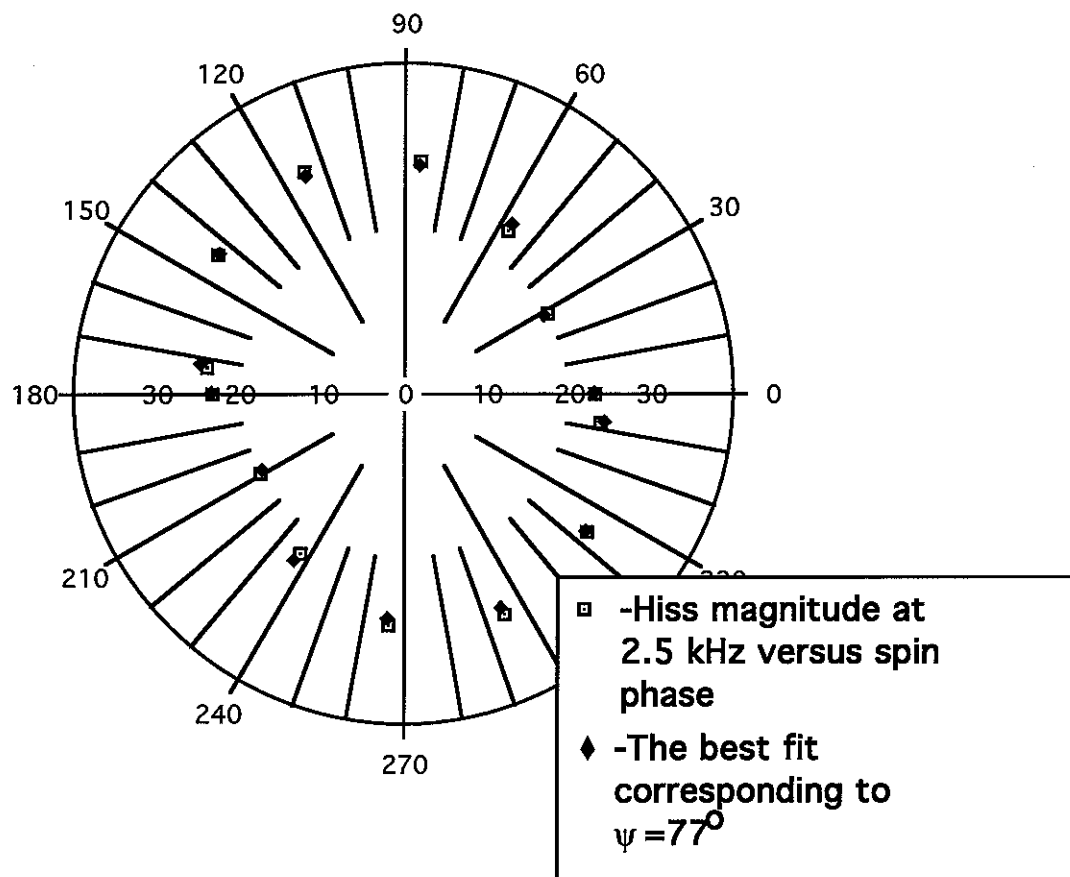
Fig. 2.13. Amplitude of hiss measured at $f = 2.5$ kHz during the same time period as in Figures 2.9, 2.10 shown in the same format. The best fit values to the experimentally observed amplitudes correspond to the average wave vector of hiss with an angle of $\psi=77°$ with respect to the magnetic field, with the perpendicular component tilted at the angle of $\sim80°$ with respect to the magnetic meridional plane.

to Figures 2.10 and 2.11. In both cases, the hiss wave vector was nearly perpendicular to the meridional plane, the azimuthal angle of the wave vector tilt with respect to the magnetic meridional plane being $\sim80°$. Figure 2.14 sketches the wave vectors for whistlers at 4.5 kHz and for hiss at 2.5 kHz as determined from the data, showing that while whistlers propagate at an angle of $\sim20°$ with respect to the meridional plane, hiss propagates nearly orthogonal to the same plane, and that whistlers have generally smaller wave normal angles than hiss. We can compare the above results with the previous work on the measurement of wave normal angles of signals injected from the Siple

Station VLF transmitter [*Sonwalkar and Inan*, 1986]. Experimental parameters in our case (i.e., *L*-value, frequency) are similar to those of Siple Station signals. The wave normal angles for Siple signals observed on DE-1 were found to be $\sim$50 $-$ 60° with the wave vector being located nearly in the meridional plane [*Sonwalkar and Inan*, 1986], in good agreement with our measurements for whistlers. The wave vector magnitudes for hiss and for whistlers in Figure 2.14 are $\sim$2.5 $\times$ 10^{-5} cm^{-1} and $\sim$1.6 $\times$ 10^{-5} cm^{-1} respectively.

Assuming that whistler rays enter the ionosphere almost along the magnetic field lines, an azimuthal component of the wave vector of whistlers would only arise if there exist considerable density gradients in azimuth (as it follows from the azimuthal component of the WKB equation (3.3.2*a*) for the wave vector, provided in the next chapter). One way that this can happen involves wave scattering from field aligned irregularities, which commonly exist in the ionospheric plasma over a wide range of length scales [*Bell and Ngo*, 1990]. Such scattering of initially vertical whistler waves can produce oblique whistler waves with wave vectors of different magnitude distributed in all directions [*Sonwalkar et al.*, 1984]. Depending on the azimuthal component of the wave vector, whistler mode rays would then drift in longitude during their propagation in the magnetosphere. If the observation point (i.e., the satellite) is located at a longitude different from that of the ionospheric illumination region by a lightning source, only those rays which drift in longitude from the source to the satellite would be observed. Since the direction and magnitude of the longitudinal drift of whistler rays is determined by the azimuthal component of their wave vector, the satellite would observe only those rays for which the azimuthal component of the wave vector has the right polarity.

Since whistler rays continue to drift in longitude after they pass the observation point during their first hop, they would be at a different longitude during their second and consecutive hops, and therefore may not be observed on the satellite. This circumstance may have been in effect in the case of the data presented in Figure 2.9, where the majority of whistlers exhibited dispersion corresponding to a direct path of propagation. The
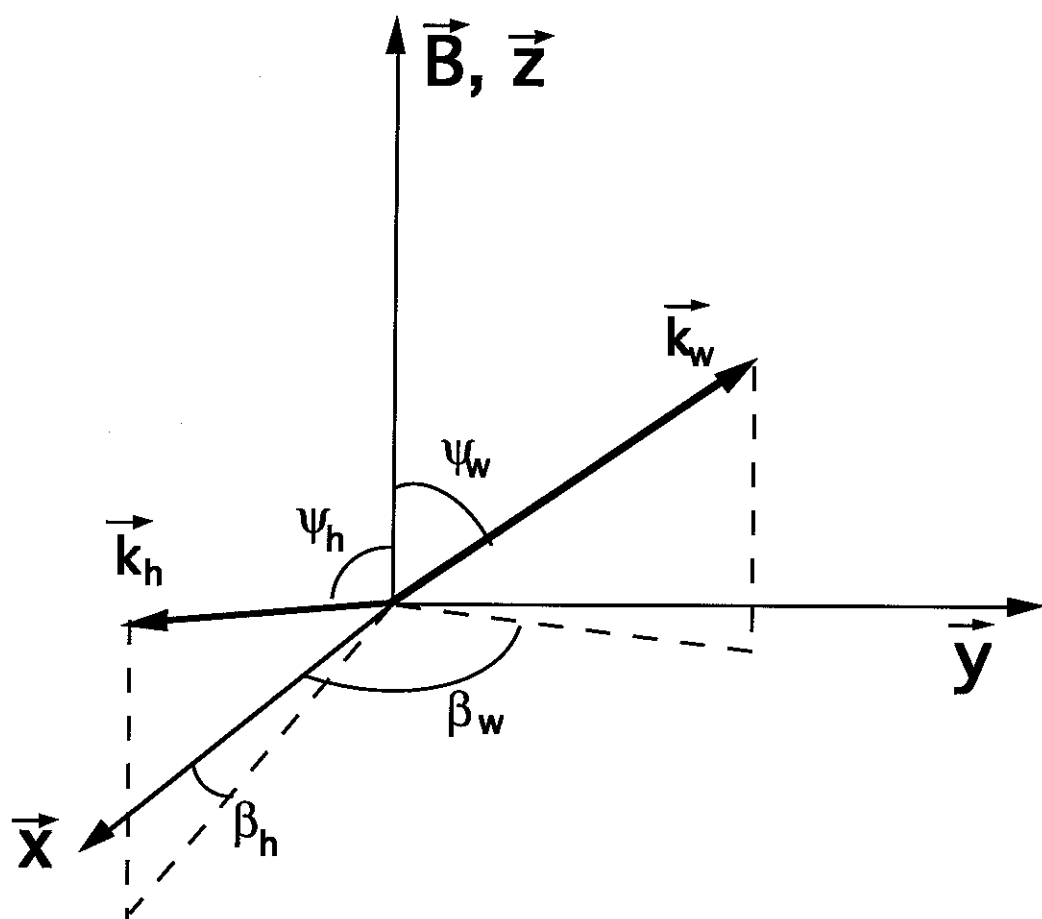
Fig. 2.14. The sketch of orientation of the wave vectors of hiss $\vec{k}_h$ for $f = 2.5$ kHz and whistlers $\vec{k}_w$ for $f = 4.5$ kHz as determined from the data. Note that while whistlers are propagating close to the magnetic meridional plane ($\beta_w \sim \frac{\pi}{2}$), hiss propagates with a high angle with respect to the meridional plane.

fraction of whistlers with greater dispersion (corresponding to either reflected whistlers, or whistlers from a different thunderstorm center) did not exceed a few percent.

The existence of an azimuthal component of the wave normal direction for both whistlers and hiss implies that further assessment of any connection between whistlers and hiss must be based on three dimensional ray tracing. In the next chapter, we develop an approximate three-dimensional ray tracing technique, which is then used to show how plasmaspheric hiss might be produced as a result of nonducted whistler propagation, consistent with the measured wave normal angles of both hiss and whistlers as described in this chapter.

3

A new mechanism for generation of plasmaspheric hiss

3.1 INTRODUCTION

In this chapter, we interpret the results of our measurement of hiss and whistler wave vector directions on the basis of ray-tracing calculations and propose a new mechanism for the generation of plasmaspheric hiss. We show that nonducted whistlers, propagating back and forth between magnetospheric reflection points, may persist for a long time ($\sim 10^2$ s for $f = 1$ kHz) in the magnetosphere without considerable damping. Whistler waves originating in the same lightning discharge, but entering the magnetosphere at a distributed set of points and with an the initial spread in wave vectors (due possibly to irregularities) propagate along different paths and arrive at an observation point (i.e., a satellite) at different times. The superposition of such a collection of whistler rays forms a continuous hiss-like signal in the magnetosphere, as observed at a fixed point. Accounting for the high average rate of lightning activity on a global scale ($\sim 10^2$ lightning discharges per second [*Uman*, 1987]), we arrive at the conclusion that a major part of plasmaspheric hiss may be formed as a result of propagation and evolution of a large number of nonducted, magnetospherically reflected, whistlers.

In Section 3.2 we analyze the propagation of whistler mode waves in the magnetosphere using a two-dimensional ray-tracing formulation. By tracing the trajectories of a large number (several hundreds) of whistler rays we investigate the formation of a continuous noise-like signal via superposition of nonducted, magnetospherically reflected, whistlers. These two-dimensional ray tracing calculations are necessarily limited to the cases in which the wave vector is confined to the magnetic meridional plane.

As was discussed in connection with the wave normal analysis presented in the previous chapter, the two-dimensional assumption is only applicable under limited circumstances. Therefore, comprehensive modeling of nonducted whistler propagation and its role in the establishment of plasmaspheric hiss should include three-dimensional effects. Accurate three dimensional ray tracing is a complicated problem and in general can be performed only by numerical methods [*Green et al.*, 1977] which do not easily lend themselves to the analysis of a large number of raypaths. These techniques also utilize large complicated numerical codes that mask the physical properties of the raypath behavior. Especially in the case of multiple magnetospheric reflections, as the wave vector approaches the resonance cone, the numerical solutions often become unstable. On the other hand, in this regime when $\psi \sim \psi_r$, considerable analytical simplifications can be made to describe the behavior of the raypaths in a physically insightful manner. In Section 3.3, we put forth an approximate analytical formulation to describe the three dimensional propagation of whistler waves with wave vectors close to the resonance cone. The equations so derived are then used in Section 3.4 to investigate the generation of plasmaspheric hiss via multiple reflections of nonducted whistlers, using experimental values extracted from our wave normal analysis (Section 2.6). The association between hiss and nonducted whistlers delineated by the ray-tracing calculations is discussed in Section 3.5, whereas qualitative aspects of the nonducted propagation of whistler mode waves with frequencies below the local lower hybrid resonance frequency are presented in Section 3.6.

3.2   RESULTS OF TWO DIMENSIONAL RAY-TRACING CALCULATIONS

Two-dimensional ray-tracing calculations were carried out with the Stanford VLF ray-tracing program [*Smith and Angerami*, 1968; *Inan and Bell*, 1977] using a diffusive equilibrium model for the plasmaspheric electron density [*Angerami and Thomas*, 1964] consisting of a mixture of 30% H^+ and of 70% O^+ at 1000 km, with a plasma density of 500 cm^{-3} at L=4 and a uniform plasma temperature of 2000°K. The earth's magnetic field was taken to be that of a tilted dipole. The raypaths traced were those for which initial wave energy was assumed to enter the magnetosphere at 400 km altitude at 16 discrete frequencies ranging from 500 Hz to 4.0 kHz over a finite range of geomagnetic latitudes ($40^o - 51^o$) and with initial spread in wave-normal angles of up to $\pm 10^o$ around the vertical. Since for the typical ionospheric parameters, the wave vector magnitude is of order of $k \sim 10^{-5}$ cm^{-1}, the $\pm 10^o$ spread in wave normal angles correspond to transverse wave vector components of $k_\perp \sim 10^{-6}$ cm^{-1}, so that the scale of an inhomogeneity of the electromagnetic field in the transverse direction can be estimated as $\frac{2\pi}{k_\perp} \sim 10^2$ km. Such distributions of wave-normal angles can thus be expected to result from mild inhomogeneities or irregularities in the lower ionosphere [*Sonwalkar et al.*, 1984].

In the presence of typical plasmaspheric density and magnetic field gradients, the wave-normal angle of whistler-mode wave approaches the Gendrin angle [*Gendrin*, 1961] after several magnetospheric reflections (i.e., reflections near the point where the wave frequency is equal to the local lower hybrid frequency), with the wave energy thereafter propagating almost along the magnetic field line [*Edgar*, 1976]. Due to this behavior, rays injected into the medium at different latitudes and with different initial parameters tend to settle down at the same L-shell after several reflections [*Jasna et al.*, 1990], with the L-value depending only on wave frequency, rather than on the injection latitude or initial wave normal angle. A typical raypath illustrating this behavior is shown in Figure 3.1.

While the eventual L-shell on which the raypath settles down is dependent only on
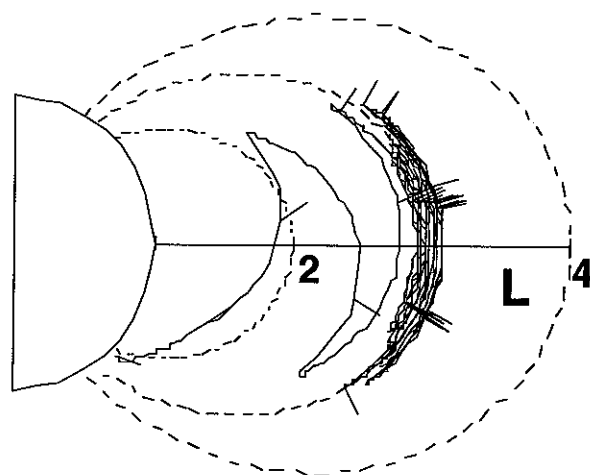
Fig. 3.1.   A typical trajectory of a whistler ray of 1 kHz frequency originating at 46° latitude with initial vertical orientation of the wave vector.   Small segments on the trajectory show the orientation of the wave vector.

frequency, the group time delay between the arrival of a ray at a given point and the initial lightning flash depends sensitively on the point of entry of the ray into the medium and the initial wave-normal angle, as illustrated in Figure 3.2. The crosses in Figure 3.2a represent the L value at the equatorial plane crossings of the trajectories of 1 kHz whistler mode wave packets (that have entered the medium at different latitudes and with different wave normals as discussed above) as a function of hop number (i.e., the number of reflections that the wave packet has undergone). It is evident that trajectories with different initial parameters propagate on different L-shells during the first 15-20 hops but eventually settle down to propagation at $L \simeq 2.8$. The group time delays (as observed at at the equatorial plane) of the same set of trajectories are given in Figure 3.2b and show substantial variation between the different trajectories. This diversity in group time delay
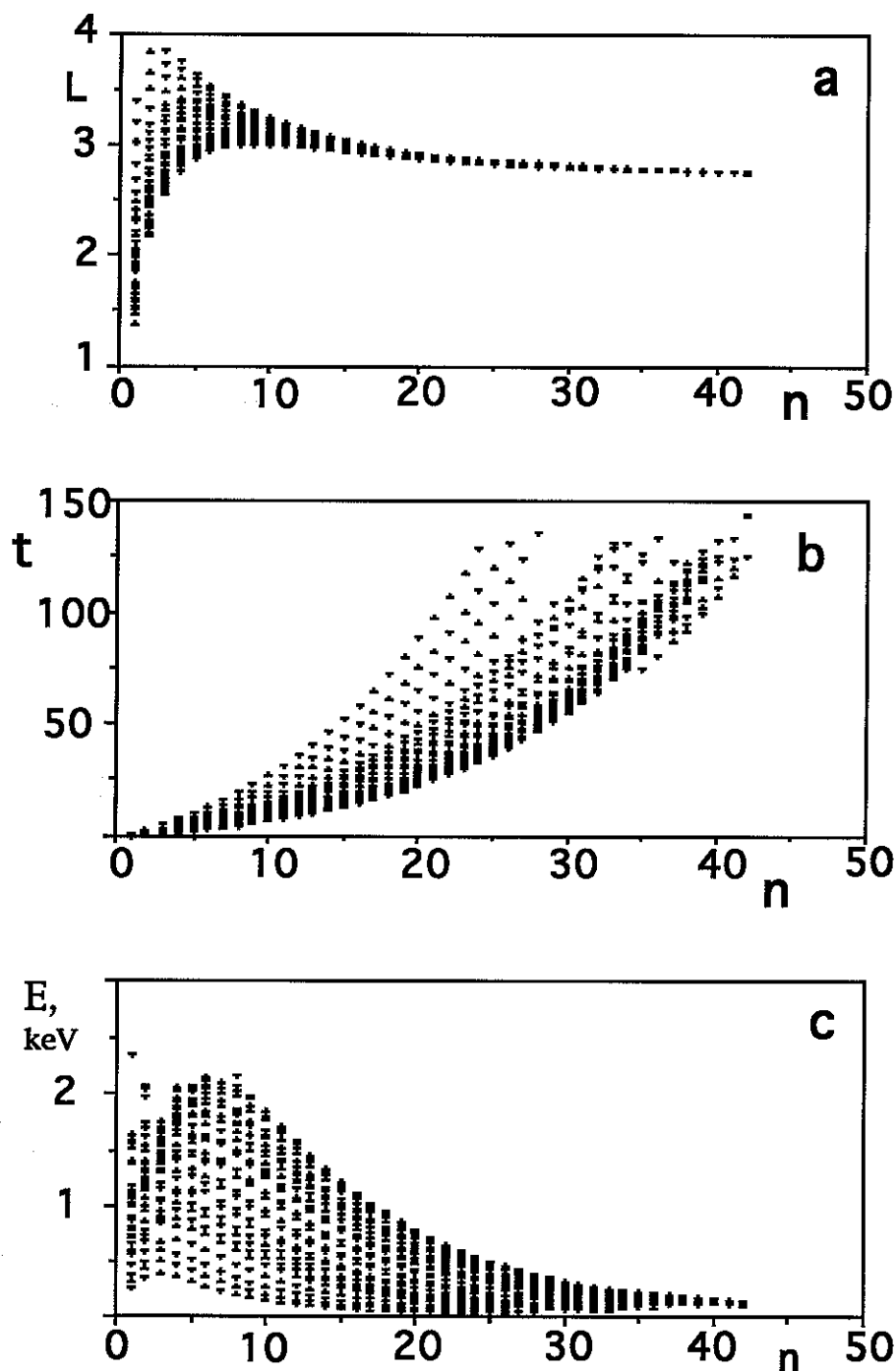
Fig. 3.2. Results of ray tracing simulation for whistler mode waves originating from a single lightning flash.   The rays with frequency $f = 1$ kHz were injected with initial wave-normal angles of ±10 ° around the vertical and initial geomagnetic latitudes ranging from $40°$ to $51°$ at 400 km altitude. (a) L values for rays at the equatorial plane versus hop number n. (b) Group time delay at the equatorial plane versus hop number. (c) Landau resonant electron energy at the equatorial plane versus hop number.

is precisely the property which leads to the formation of a nearly continuous signal as observed at a given point in the magnetosphere.

While the raypath calculations indicate the trajectory of the wave energy, the total lifetime of a wave packet propagating along such a path is limited by wave damping. While, in general, raytracing formulations that includes the growth or decay of the wave along the raypath [e.g. *Horne*, 1989] would be needed, relatively straightforward evaluation of the potential for wave damping can be made by examining the Landau resonant* electron energy $\mathcal{E} = \frac{m}{2}(\frac{\omega}{k_{\parallel}})^2$ corresponding to the raypath locations of Figure 3.2*a,b*. This quantity is plotted in Figure 3.2*c* where we note that the Landau resonant energy approaches the thermal electron energies (i.e., <10 eV) only after several tens of hops, indicating that the damping along these raypaths would be small. In our analysis, we have carried the ray-tracing calculations up to the point where $\mathcal{E}$=40 eV, so that we can safely assume Landau damping to be negligible. We computed whistler wave damping numerically for a Maxwellian plasma with $T_e = 5$ eV, and magnetic field and density corresponding to a point at the magnetic equator at L=3.0 in the above diffusive equilibrium model. The wave refractive index and the imaginary part of the wave frequency (which corresponds to the wave damping rate) for a 1.273 kHz wave are shown in Figure 3.3. Significant damping of the wave (Imω**> 10^{-2} s^{-1} corresponding to lifetimes of whistler waves in the magnetosphere below ~100 seconds) occurs for large refractive indexes only ($k \sim 0.05$ m^{-1} which corresponds to $\mu = ck/\omega \sim 10^4$). Ray tracing calculations presented in Figure 3.2 correspond to considerably lower refractive indexes $\mu \sim 10^3$, so that we can safely assume that the damping for wave packets in Figure 3.2 is negligible.

We note that in the model described above, any frequency component of the continuous noise-like signal observed at a given time at any point propagates along a raypath

---

* The Landau interaction between plasma waves and charged particles occurs when the parallel particle velocity $v_{\parallel}$ satisfies the condition $\omega - k_{\parallel}v_{\parallel} = 0$, i.e., particles move along the magnetic field with the phase speed of the wave [*Krall and Trivelpiece*, 1973].

** Here Imω represents the decay rate for a wave expressed as exp($i\omega t$) with ω =Reω + iImω.
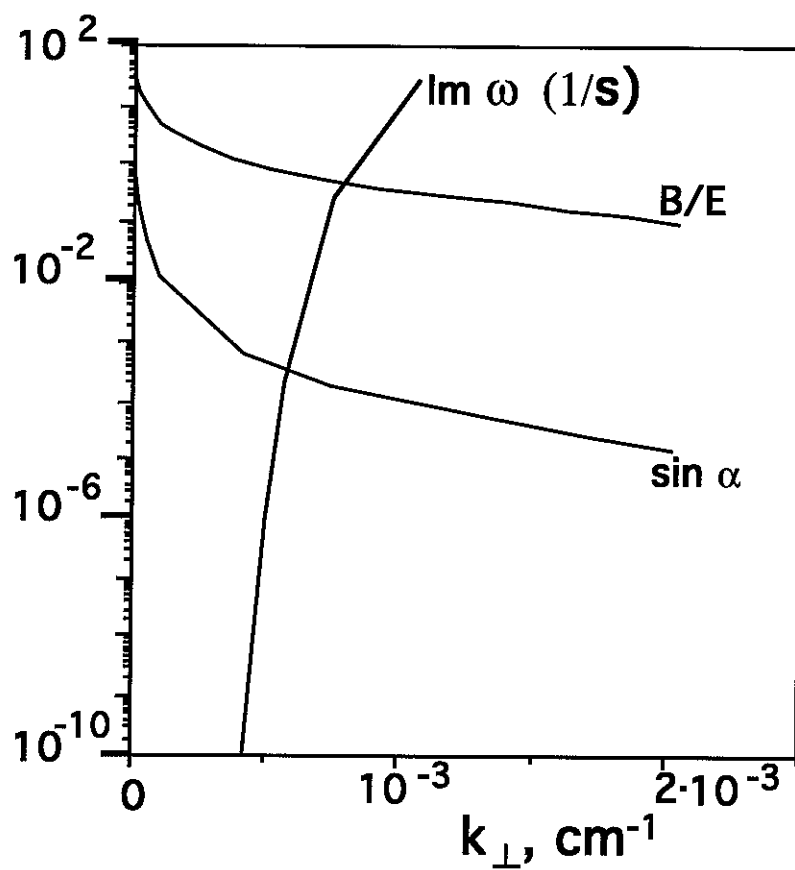
Fig. 3.3. Wave damping, sine of the angle between $\vec{E}$ and $\vec{B}$, and (B/E) ratio for $\mathrm{Re}\omega = 2\pi \times 1273$ rad/s (1273 Hz) at $L=2.82$.   A Maxwellian plasma with 5 eV temperature was assumed.

that extends from the ground to the observation point. The large number of ray trajec-
tories analyzed represent a sample of waves originating at the same lightning discharge,
but differing in their point of entry into the medium, initial wave normal angle and/or
frequency. This finite sample of ray trajectories can be used to determine the correspond-
ing frequency-time spectrum which would be observed by a satellite located at several
selected regions in the magnetosphere by identifying all rays which pass through these
regions. Wave packets propagating along raypaths with different initial parameters pass
through any such region at different times. The resulting frequency-time spectrum in
each region can thus be reconstructed from a subset of our computed ray trajectories by
mapping on a frequency-time plane the frequency of wave packet versus the group time
delay at the time of ray crossing of the observation region.

Figures 3.4 through 3.6 show frequency-time diagrams for different selected observa-
tion regions that are reconstructed by means of tracking the position of ray trajectories at
each of the 16 discrete frequencies (ranging from 500 Hz to 4.0 kHz) for which waves
were injected into the magnetosphere under different conditions (geomagnetic latitude,
wave normal angle), with each cross representing an equatorial plane crossing at a se-
lected region by an individual ray trajectory. The 36 trajectories used for each frequency
allow for enough resolution without having the crosses overlap in Figures 3.4 through
3.6.

The observation regions were selected as $1.90 < L < 1.91$, $2.82 < L < 2.83$, and
$3.47 < L < 3.48$ and were chosen to have a radial extent small enough so that the results
would be representative of what would be observed on a spacecraft, but large enough so
that a reasonably representative number of the considered raypaths crossed the regions.
Detailed analysis of the results of ray-tracing simulations shows that, as observed in a
fixed region, signals from consequent hops do overlap after the first several hops and,
over a long time scale, the subset of trajectories that arrive at the observation region form
an enduring hiss-like signal with distinctive upper and lower frequency cutoffs. These

Fig. 3.4. Frequency-time diagram for rays crossing the equatorial plane at observation regions in the magnetosphere defined as $1.90 < L < 1.91$. Initial wave-normal angles and latitudes of injection of the rays are the same as in Figure 3.2. Sixteen different frequencies ranging from 500 Hz to 4.0 kHz were considered. The highlighted envelope constitutes the continuous hiss-like spectrum that would be observed.

continuous signals, as sampled by our finite set of points and sketched in Figures 3.4-3.6 as shaded areas for the different observation regions. Discrete magnetospherically reflected whistlers formed by the first several hops of the initial whistler [*Edgar*, 1976] are not shown in Figures 3.4-3.6 since we emphasize the long-time scale behavior of whistler waves. The continuous hiss-like signal does not immediately follow the initial magnetospherically reflected whistlers, but develops after a substantial time interval (~ 10 s) after the initial lightning flash.

From Figures 3.4 through 3.6 we note that higher frequency hiss-like signals would be observed at lower L-shells ($f \sim 3.5$ kHz at $L \simeq 1.90$ compared to $f \sim 0.6$ kHz at $L \simeq 3.47$). The spectral widths of the continuous hiss-like signals, as predicted by our ray-tracing simulations, ranges from ~ 1 kHz for the highest observation region (L=3.47) (Figure 3.6) to $\sim 10^2$ Hz for the lowest one (L=1.90) (Figure 3.4). Another important
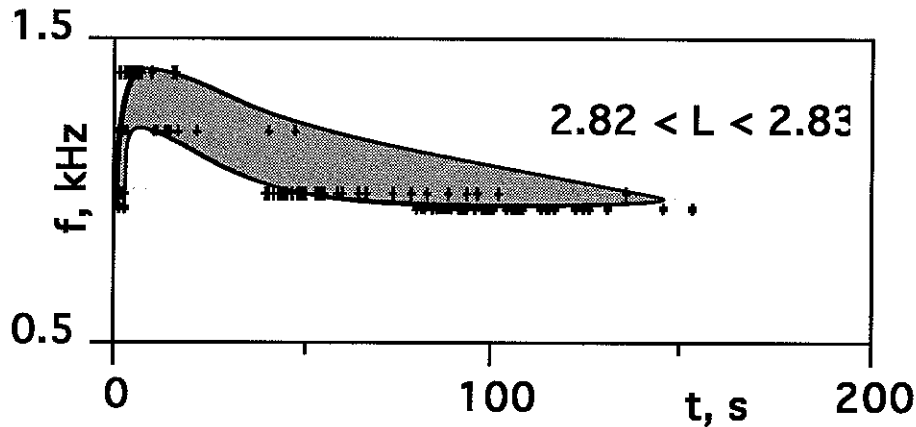
Fig. 3.5. Frequency-time diagram for rays crossing the equatorial plane at observation regions in the magnetosphere defined as $2.82 < L < 2.83$. Initial wave-normal angles and latitudes of injection of the rays are the same as in Figure 3.2. Sixteen different frequencies ranging from 500 Hz to 4.0 kHz were considered. The highlighted envelope constitutes the continuous hiss-like spectrum that would be observed.

feature is the duration (limited by the Landau damping condition of $\mathcal{E} > 40$ eV) of the continuous signals produced by a single lightning flash, which ranges from $\sim$30 s for higher frequencies observed at L=1.90 (Figure 3.4) to $\sim$200 s for the lower frequencies observed at L=3.47 (Figure 3.6). If a subsequent lightning flash occurs during this time, the hiss-like signal from the second flash would overlap that from the first one, as is commonly observed in experimental data [*Sonwalkar and Inan*, 1989]. It thus appears that a continuous hiss signal would be more likely to be formed by whistlers only, if successive lightning discharges occur with a frequency of at least one flash in several tens of seconds. Such a rate of flash occurrence within each thunderstorm is common [*Peckham et al.*, 1984]. Since the general trend of the results is that low-frequency (high L-shell) signals from a given lightning flash endure longer than high-frequency (low L-shell) signals, it appears that we can expect lightning to be a more likely contributor to the
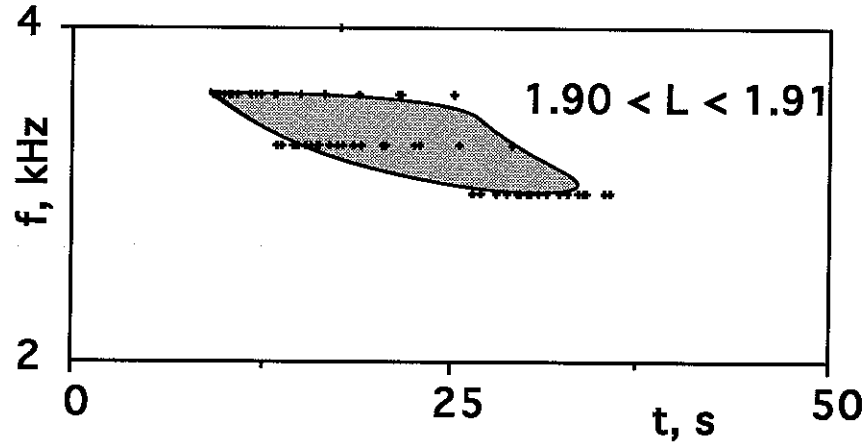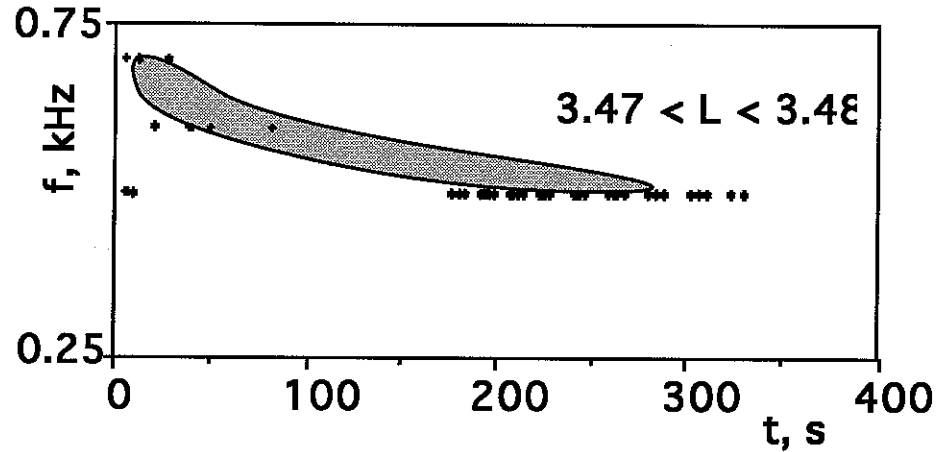
Fig. 3.6. Frequency-time diagram for rays crossing the equatorial plane at observation regions in the magnetosphere defined as $3.47 < L < 3.48$. **Initial wave-normal angles and latitudes of injection of the rays are the same as in Figure 3.2. Sixteen different frequencies ranging from 500 Hz to 4.0 kHz were considered. The highlighted envelope constitutes the continuous hiss-like spectrum that would be observed.**

sustenance of low-frequency hiss-like signals ($f < 1$ kHz) at high L-shells ($L \sim 3 - 4$), in qualitative agreement with reported observations of plasmaspheric hiss [*Thorne et al.*, 1973].

3.3 WHISTLER WAVE PROPAGATION IN THREE DIMENSIONS: ANALYTICAL FORMULATION

The two-dimensional ray tracing calculations presented above show that plasmaspheric hiss can at least in part be formed by multiply reflecting whistlers. However, further assessment of this mechanism of hiss generation and its application to the existing experimental data is limited by the assumption that the wave vector of hiss and whistlers lies in the magnetic meridional plane. As was shown in Chapter 2, wave normal angles of hiss and whistlers are often found to lie at an angle to the magnetic meridional

plane. Therefore, comprehensive modeling of whistler and hiss propagation in the mag-
netosphere should include effects of three dimensional propagation, to account for cases
in which the wave vector is not in the magnetic meridional plane. In this and subse-
quent sections we put forth a new analytical formulation and apply it to examine oblique
whistler ray paths in the magnetosphere. The results of this theoretical model are used to
assist in interpretation of the experimental data, in particular simultaneous measurement
of whistlers and hiss wave vector directions as described in Section 2.6.

We start from the approximate dispersion equation for quasi-electrostatic whistler
waves in a cold plasma, obtained from Maxwell equations and equations of motion
for the electron and ion species [*Krall and Trivelpiece*, 1973]

$$D(\omega, \vec{k}) = -1 + \frac{\omega_{pi}^2}{\omega^2} + \frac{\omega_{pe}^2}{\omega^2} \cos^2 \psi - \frac{\omega_{pe}^2}{\omega_{He}^2} = 0 \qquad (3.3.1)$$

where $\cos \psi = k_\parallel / k$, ψ is the wave normal angle, $\omega_{pe,i}$ are plasma electron and ion
frequencies respectively, ω_{He} is the electron gyrofrequency, and $k_\parallel$ is the wave vector
component parallel to the ambient magnetic field. Since we are primarily interested in
wave propagation at high altitudes, we consider a purely hydrogen plasma. The equations
for the ray trajectory in the inhomogeneous magnetoplasma can be obtained in parametric
form as $\vec{k} = \vec{k}(\tau)$, $\vec{r} = \vec{r}(\tau)$, $t = t(\tau)$ by differentiating the function $D(\omega, \vec{k})$ [*Galeev and Sudan*, 1983]

$$\frac{d\vec{k}}{d\tau} = \frac{\partial D(\omega, \vec{k})}{\partial \vec{r}} \qquad (3.3.2a)$$

$$\frac{d\vec{r}}{d\tau} = -\frac{\partial D(\omega, \vec{k})}{\partial \vec{k}} \qquad (3.3.2b)$$

$$\frac{dt}{d\tau} = \frac{\partial D(\omega, \vec{k})}{\partial \omega} \qquad (3.3.2c)$$

where τ is a parameter. We start our analysis of equations (3.3.2) by evaluating the
right-hand side of equation (3.3.2c). After differentiating of $D(\omega, \vec{k})$ with respect to ω,

we use the fact that $D(\omega, \vec{k}) = 0$ along the trajectory to obtain

$$\frac{dt}{d\tau} = -\frac{2}{\omega}\left(1 + \frac{\omega_{pe}^2}{\omega_{He}^2}\right) \tag{3.3.3}$$

Since for typical plasmaspheric parameters (see discussion in Chapter 1 and references therein) $\frac{\omega_{pe}^2}{\omega_{He}^2} \gg 1$, we have

$$\frac{dt}{d\tau} = -\frac{2}{\omega}\frac{\omega_{pe}^2}{\omega_{He}^2} \tag{3.3.4}$$

To evaluate the group velocity of the wave, we use both (3.3.4) and evaluate the change of r with parameter τ by differentiating the right hand side of (3.3.2b), where $D(\omega, \vec{k})$ is in the form of (3.3.1) and depends on $\vec{k}$ through $\cos\psi$

$$v_{g\perp} = \frac{dr_\perp}{d\tau}\left(\frac{dt}{d\tau}\right)^{-1} = -\frac{\omega_{He}^2}{\omega}\frac{k_\parallel^2 k_\perp}{k^4} \tag{3.3.5a}$$

$$v_{g\parallel} = \frac{dr_\parallel}{d\tau}\left(\frac{dt}{d\tau}\right)^{-1} = \frac{\omega_{He}^2}{\omega}\frac{k_\parallel k_\perp^2}{k^4} \tag{3.3.5b}$$

Note that equation (3.3.5) includes $k_\parallel, k_\perp$, the values of which can be determined from equation (3.3.2a). In calculating the derivatives with respect to $\vec{r}$ in (3.3.2a), we take into account the dependence of $D(\omega, \vec{k})$ on the coordinates $\vec{r}$ through the parameters $\omega_{pe}, \omega_{pi}, \omega_{He}$ of the inhomogeneous media. A first simplification of equation (3.3.2a) can be made by separately evaluating the contributions from the inhomogeneity of the plasma density and the inhomogeneity of the magnetic field. To evaluate the former quantity, we note that since $\omega_{pe}^2, \omega_{pi}^2$ are proportional to the plasma density N and find

$$\frac{\partial\omega_{pe}^2}{\partial\vec{r}} = \frac{\omega_{pe}^2}{N}\frac{\partial N}{\partial\vec{r}}$$

$$\frac{\partial\omega_{pi}^2}{\partial\vec{r}} = \frac{\omega_{pi}^2}{N}\frac{\partial N}{\partial\vec{r}}$$

Therefore, for the contribution due to the density inhomogeneity we find

$$\left(\frac{\partial D(\omega, \vec{k})}{\partial \vec{r}}\right)_n = \frac{1}{N}\frac{\partial N}{\partial \vec{r}}\left(\frac{\omega_{pi}^2}{\omega^2} + \frac{\omega_{pe}^2}{\omega^2}\cos^2\psi - \frac{\omega_{pe}^2}{\omega_{He}^2}\right)$$

Since $D(\omega, \vec{k}) = 0$ along the trajectory, the quantity in the parenthesis is equal to unity (compare to (3.3.1)), yielding

$$\left(\frac{\partial D(\omega, \vec{k})}{\partial \vec{r}}\right)_N = \frac{1}{N}\frac{\partial N}{\partial \vec{r}} \tag{3.3.6}$$

The evaluation of the contributions from the inhomogeneity of the inhomogeneity of the magnetic field is straightforward

$$\left(\frac{\partial D(\omega, \vec{k})}{\partial \vec{r}}\right)_H = \frac{2}{H}\frac{\omega_{pe}^2}{\omega_{He}^2}\frac{\partial H}{\partial \vec{r}} \tag{3.3.7}$$

Since for typical plasmaspheric parameters $\frac{\omega_{pe}^2}{\omega_{He}^2} \gg 1$, we have $(\frac{\partial D(\omega, \vec{k})}{\partial \vec{r}})_H \gg (\frac{\partial D(\omega, \vec{k})}{\partial \vec{r}})_N$, meaning that the ray trajectory is primarily determined by the magnetic field gradients, rather than by those of the electron and ion density. In this derivation we assumed that the density profile does not have any abrupt changes along the ray trajectory (e.g., the wave does not encounter whistler ducts or the plasmapause during its propagation), so that the characteristic scale of the change of the density $\left(\frac{1}{N}\frac{\partial N}{\partial r}\right)^{-1}$ is large enough (of the order of the Earth radius), which is a good approximation for any plasmaspheric density model in the absense of the plasmapause and ducts.

We can use the approximation above to determine the radial component k_r of the wave vector in the spherical coordinate system with z-axis aligned with the dipole moment of the earth's magnetic field (Figure 3.7). Since we only have to evaluate the derivative with respect to the magnetic field, and since in the dipole approximation the magnetic field intensity is proportional to the inverse third power of radial distance $H = \frac{const}{r^3}$ (which yields $\frac{1}{H}\frac{\partial H}{\partial \vec{r}} = -\frac{3}{r}$), we find by substituting (3.3.7) in (3.3.2a)

$$\left(\frac{d\vec{k}}{d\tau}\right)_r = -\frac{\omega_{pe}^2}{\omega_{He}^2}\frac{6}{r} \tag{3.3.8}$$
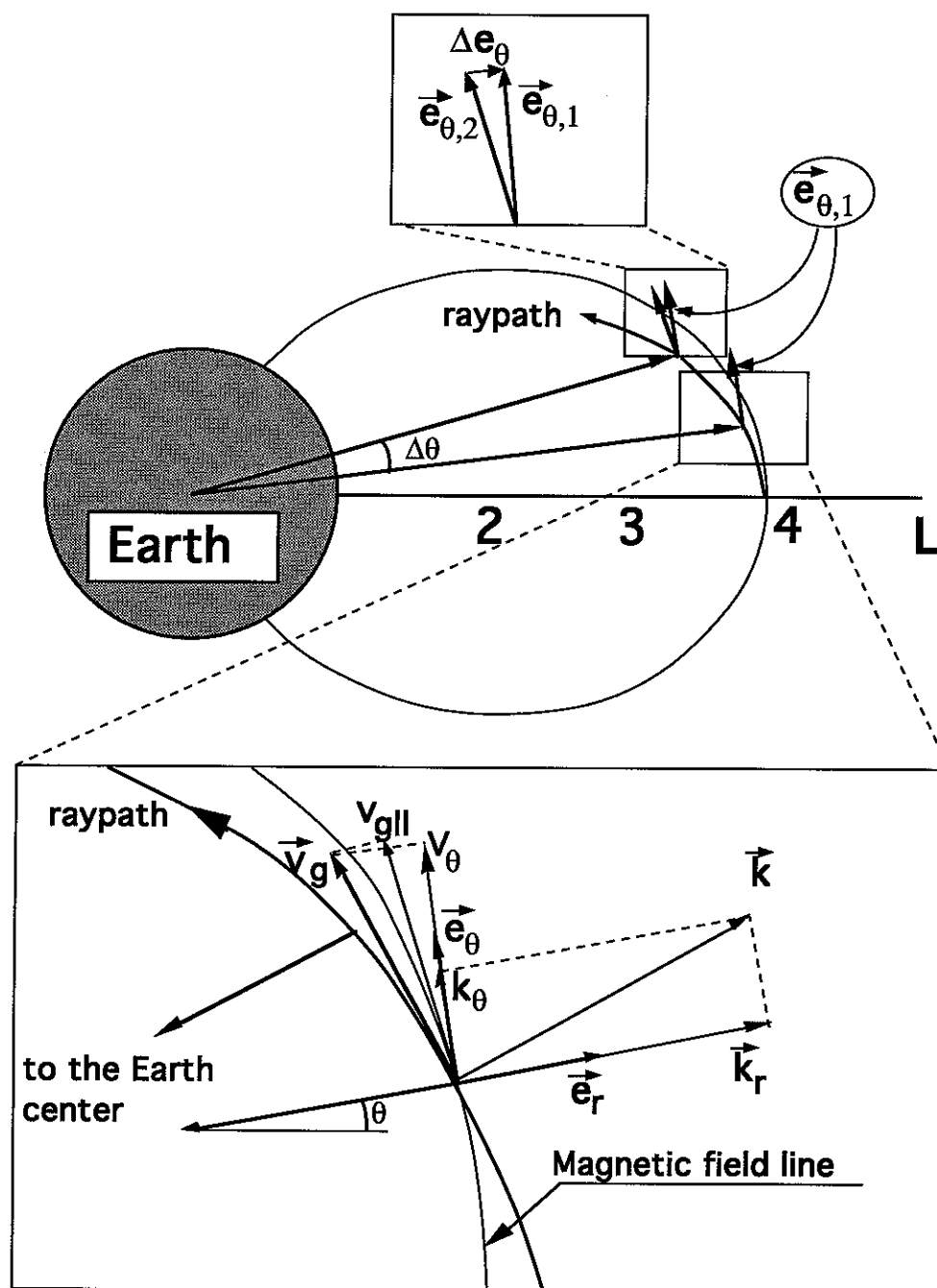
Fig. 3.7. The spherical coordinate system used for the three-dimensional ray-tracing and the variation of the wave packet position, the wave vector and unit vectors $\vec{e}_{r,\theta}$. The unit vector $\vec{e}_\phi$ is normal to the plane of the figure. The unit vector $\vec{e}_\theta$ is shown at points 1 and 2 along the raypath, showing the change $\Delta\vec{e}_\theta$. Note that due to the primarily θ-direction of the propagation and due to the fact that we consider regions which are not too far from the magnetic equator, the wave vector component $\vec{k}_\theta$ and the change in the wave packet position (which is in the direction of the group velocity $\vec{v}_g$) are approximately equal to the projection of these vectors to the direction of the magnetic field.

where r is the radial distance from the center of the Earth. Substituting $\frac{dt}{d\tau}$ from (3.3.4), we find a surprisingly simple equation for $\left(\frac{d\vec{k}}{d\tau}\right)_r$ as

$$\left(\frac{d\vec{k}}{dt}\right)_r = \left(\frac{d\vec{k}}{d\tau}\right)_r \left(\frac{dt}{d\tau}\right)^{-1} = \frac{3\omega}{r} \qquad (3.3.9)$$

Now we turn to the evaluation of the left-hand side of (3.3.9). In an earth centered spherical coordinate system (see Figure 3.7), the direction of unit vectors depends on the ray location. We therefore have

$$\left[\frac{d}{d\tau}(\vec{e}_r k_r + \vec{e}_\theta k_\theta + \vec{e}_\phi k_\phi)\right]_r = \frac{dk_r}{d\tau}\vec{e}_r + k_r\left(\frac{d\vec{e}_r}{d\tau}\right)_r + k_\theta\left(\frac{d\vec{e}_\theta}{d\tau}\right)_r + k_\phi\left(\frac{d\vec{e}_\phi}{d\tau}\right)_r \qquad (3.3.10)$$

where $\vec{e}_{r,\theta,\phi}$ are unit vectors along the local directions of the axis of the spherical coordinate system. We can estimate the relative contribution of different terms in the right-hand side of (3.3.10). The second term is identically equal to zero, because the projection of the unit vector $\vec{e}_r$ to the radial direction is equal to unity by the definition of $\vec{e}_r$, so that the derivative of this quantity is zero. The fourth term is typically much less than the third one, since ray propagation is typically in the θ-direction so that the e_ϕ change is smaller. Thus, only contributions of the first and the third terms must be estimated. The contribution of the third term can be evaluated as

$$k_\theta\left(\frac{d\vec{e}_\theta}{d\tau}\right)_r \simeq k_\theta\left(\frac{d\vec{e}_\theta}{d\theta}\right)_r \frac{d\theta}{d\tau} = k_\theta\frac{d\theta}{dt}\frac{dt}{d\tau} \simeq \frac{k_\parallel v_{g\parallel}}{r}\frac{\partial D(\omega, \vec{k})}{\partial\omega} \qquad (3.3.11)$$

where we use (3.3.4) and again assume that ray propagation occurs primarily in θ direction, which is close to the direction of the magnetic field lines for a typical magnetospherically reflected whistler ray, so that $k_\parallel \simeq k_\theta$ and $\Delta\theta \simeq \Delta r_\parallel/r$ (see Figure 3.7). We then substitute in (3.3.11) the value of $v_{g\parallel}$ from (3.3.5a) and $\frac{\partial D}{\partial\omega}$ from the right-hand side of (3.3.4) to find

$$k_\theta\left(\frac{d\vec{e}_\theta}{d\tau}\right)_r \simeq \frac{2}{r}\frac{k_\parallel^3 k_\perp}{k^4}\frac{\omega_{pe}^2}{\omega^2} \qquad (3.3.12)$$

For typical parameters of whistler rays considered here the dispersion equation (3.3.1) gives $\left(\frac{k_\parallel}{k}\right)^2 < \left(\frac{\omega}{\omega_{He}}\right)^2$. Substituting in (3.3.12) along with $\frac{k_\perp}{k} < 1$, we have

$$k_\theta \left(\frac{d\vec{e}_\theta}{d\tau}\right)_r < \frac{2}{r}\frac{k_\parallel}{k}\frac{\omega_{pe}^2}{\omega_{He}^2} \tag{3.3.13}$$

Comparing this formula to the right-hand side of (3.3.8), we see that for highly oblique whistler waves ($k_\parallel \ll k$), the term $k_\theta(\frac{de_\theta}{d\tau})_r$ makes a negligibly small contribution in (3.3.10) and therefore in (3.3.9). Thus, we can rewrite equation (3.3.9) as

$$\frac{dk_r}{dt} \simeq 3\frac{\omega}{r} \tag{3.3.14}$$

Since in a dipole field magnetic field gradients in the azimuthal direction are equal to zero, the azimuthal component k_ϕ of the wave vector satisfies the conservation law

$$k_\phi r \sin\theta = const \tag{3.3.15}$$

Since the direction of the magnetic field line is known for any given point, all three components of the wave vector can be determined from k_r, k_ϕ, and the following expression for the $k_\parallel/k$ ratio obtained from (3.3.1)

$$\frac{k_\parallel}{k} = \frac{\omega}{\omega_{pe}}\sqrt{\left(1 + \frac{\omega_{pe}^2}{\omega_{He}^2} - \frac{\omega_{pi}^2}{\omega^2}\right)} \tag{3.3.16}$$

Equations (3.3.14) through (3.3.16), and the known magnetic field line direction and plasma parameters, fully determine the wave vector at any point along the ray trajectory. Although equations (3.3.5) specify only two quantities, all three components of the group velocity can be determined by using the fact that the group velocity vector is perpendicular to the wave vector and lies in the same plane with the wave vector and the ambient magnetic field (which follows from (3.3.5)). Therefore, the set of equations (3.3.5),(3.3.14), (3.3.15), and (3.3.16) fully define the ray trajectory and can be easily solved numerically.

Equations (3.3.5), (3.3.14), (3.3.15), and (3.3.16) have a scaling property in that they remain valid upon substitution of $\vec{k} = \alpha \vec{k}'$, $t = \alpha t'$, noting that $\vec{v} = \frac{d\vec{r}}{dt}$. In other words, two rays originating at the same point with the same frequency and wave normal angle, but with different magnitudes of wave vectors, propagate along the same trajectory, but with different group velocities. This property can be used to greatly reduced the amount of calculations needed to trace a set of ray trajectories which originate at the same point with the same initial orientation of the wave vector. Instead of solving (3.3.5), (3.3.14), (3.3.15), and (3.3.16) for each ray trajectory separately, we can numerically solve the ray tracing equations (3.3.5), (3.3.14), (3.3.15), and (3.3.16) for one ray from the set only, and then determine group time delays for all other rays from the set of trajectories using the scaling property.

3.3.1 Asymptotic behavior of whistler ray trajectories

Using equations (3.3.5), (3.3.14), (3.3.15), and (3.3.16), we can analytically investigate the asymptotic behavior of whistler rays in the earth's magnetosphere. We start by substituting the expression for $\frac{k_\parallel}{k}$ into (3.3.5b)

$$v_{g\parallel} = \frac{\omega_{He}^2 k_\perp^2}{k^3 \omega_{pe}} \left(1 + \frac{\omega_{pe}^2}{\omega_{He}^2} - \frac{\omega_{pi}^2}{\omega^2} \right)^{\frac{1}{2}} \qquad (3.3.17)$$

We can express $v_{g\parallel}$ as $v_{g\parallel} = \frac{ds}{dt}$, where s is the distance along the magnetic field line. Note, that in (3.3.17) the right hand side depends on s, through the dependence of plasma parameters on s. There is also a dependence of the right-hand side of (3.3.17) on t, in accordance with the dependence of k on t. Asymptotically, the value of k is large (see (3.3.14)), and therefore does not change significantly during one whistler ray hop between magnetospheric reflection points in the two hemispheres. Therefore, we can consider the dependence of (3.3.17) on t to be slow for large t, so that (3.3.17) is a first-order differential equation for s where the right-hand side depends on s and slowly depends on t. This equation resembles the equation of motion for a particle of unit mass,

bouncing in a potential well [*Landau and Lifshitz*, 1976]

$$\frac{ds}{dt} = \left\{ 2[E_{eff} - \phi_{eff}(s,t)] \right\}^{\frac{1}{2}} \tag{3.3.18}$$

where $E_{eff} = const$ is the "particle energy", and the effective potential $\phi_{eff}(s,t)$ is a function of s and slowly depends on t. Taking advantage of the slow dependence on t, an analytical solution of (3.3.18) can be obtained as an adiabatic approximation. While the closed form solution is complicated [*Landau and Lifshitz*, 1976], the expression for the period of the particle oscillations in the "potential well" (i.e., in our case the period of the wave motion between the magnetospheric reflection points) is in the adiabatic approximation identical to that for the case when ϕ_{eff} does not depend on t [*Landau and Lifshitz*, 1976]

$$T_{bounce} = 2\pi \left(\frac{\partial^2 \phi_{eff}}{\partial s^2} \right)_{s=s_{eq}}^{-\frac{1}{2}} \tag{3.3.19}$$

where the derivative is evaluated at the "equilibrium" point $s = s_{eq}$ (i.e., in our case at the magnetic equator). Evaluating $\frac{\partial^2 \phi_{eff}}{\partial s^2}$ and substituting into (3.3.19), we find

$$T_{bounce} = 2\pi \left(\left(\frac{4\phi_{eff}}{\omega_{He}} + \frac{2\omega_{He} k_\perp^4}{k^6} \right) \frac{\partial^2 \omega_{He}}{\partial s^2} - \frac{2\omega_{He}^4 k_\perp^4}{k^6 \omega_{pe}^3} \frac{\partial^2 \omega_{pe}}{\partial s^2} \right)^{-\frac{1}{2}} \tag{3.3.20}$$

Taking into account that k increases with t in accordance with (3.3.14), we see that the period T_{bounce} grows with t as well. Although the actual distance between reflection points in both hemispheres for a typical raypath such as that in Figure 3.1 decreases* from reflection n to $n + 1$, the asymptotic results presented above show that it takes a constantly increasing time for the ray to travel between successive reflection points. This trend is also evident from Figure 3.2b as well. Physically, it results from the decrease of the group velocity due to the increased magnitude of the wave vector.

---

* This effect is not visible from the Figure 3.1 due to many overlapping raypaths.

3.4   NUMERICAL RESULTS OF THREE-DIMENSIONAL RAY-TRACING

Numerical solution of (3.3.5) and (3.3.14)-(3.3.16) were carried out using a diffusive equilibrium model for the plasmaspheric electron density [*Angerami and Thomas*, 1964] with a plasma density of 500 cm^{-3} at $L=4$. The earth's magnetic field was taken to be that of a tilted dipole.

Comparison of the numerical solution of the two-dimensional ray-tracing equations (see Section 3.2) and the approximate analytical approach developed in Section 3.3 provides an opportunity to test both methods. Figure 3.8 shows L values and group delays plotted versus the number of magnetospheric reflections n for the equatorial crossings of a 1 kHz ray originating at 45° latitude (this is one ray from a set of rays traced in Section 3.2). We see excellent agreement for a large number of crossings, though the numerical technique based on the two-dimensional Stanford ray-tracing program shows an obviously incorrect plateau in Figure 3.8 around $n = 32 - 35$, possibly due to difficulties in handling waves with wave vectors close to the resonance cone. We note that this discontinuity occurs only after several tens of hops of the ray, which is totally appropriate for our applications.

The typical trajectory of quasi-electrostatic whistler waves bounces between LHR reflection surfaces (defined as surfaces where the wave frequency is equal to the local lower hybrid resonance frequency) while the average trend is characterized by an azimuthal drift and an asymptotic decrease in L-shell with time. The magnitude of the wave vector steadily grows in accordance with (3.3.14). The lifetime of quasi-electrostatic whistler mode waves in the magnetosphere can be estimated using (3.3.14), since when the wave vector is sufficiently large, the parallel component of the wave velocity becomes small enough for Landau damping to be significant. Landau damping is negligible [*Krall and Trivelpiece*, 1973] if

$$\mathcal{E} = \frac{m}{2}\left(\frac{\omega}{k_{\|}}\right)^2 \gg E_{th} \qquad (3.4.1)$$

where E_{th} is the electron thermal energy. Substituting $k_{\|}$ from (3.3.16) and $k \sim k_r \sim 3\frac{\omega}{r}t$ from (3.3.14), and conservatively using $\mathcal{E} = 20$ eV, the lifetime of a 2.5 kHz wave
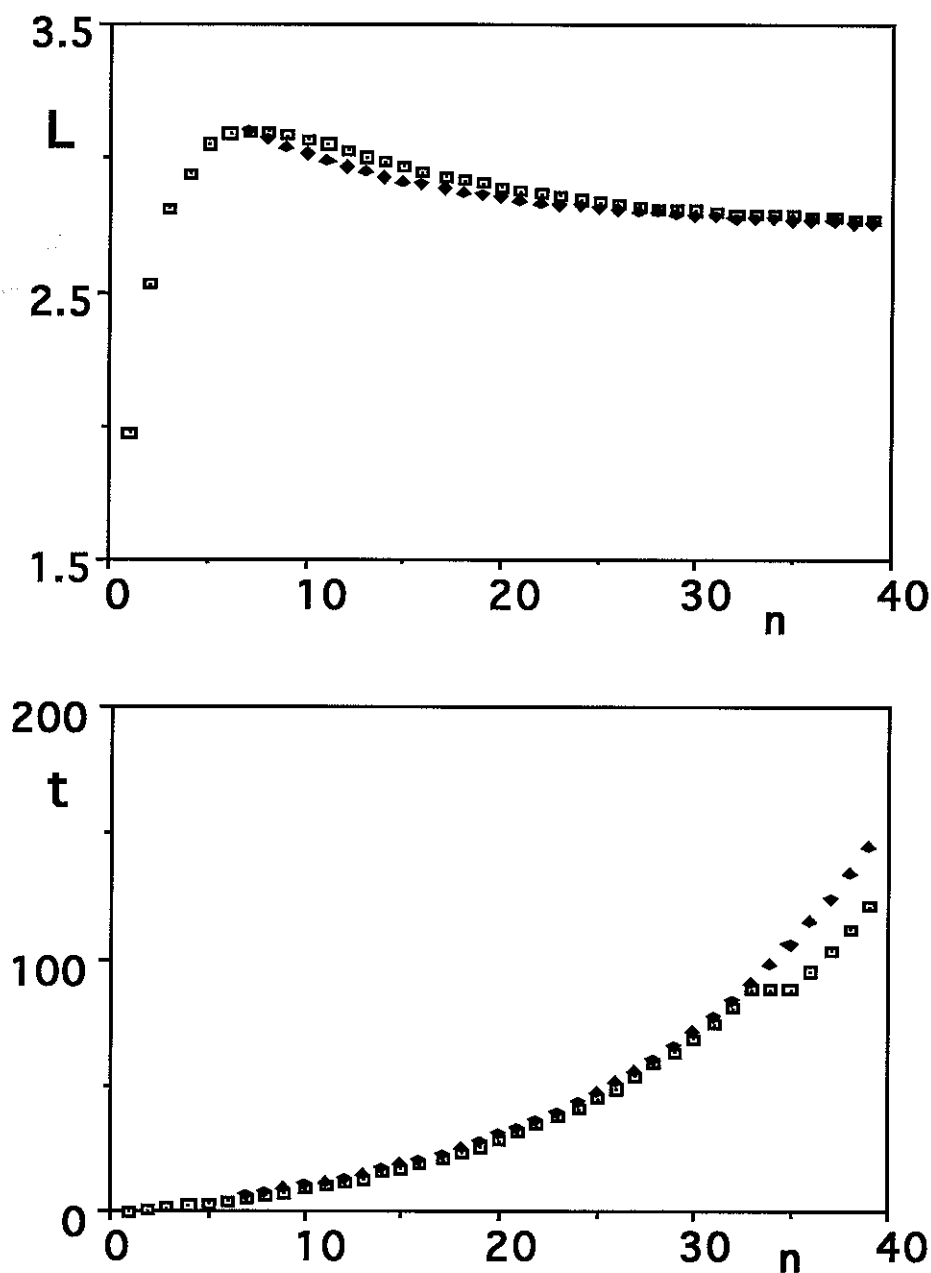
Fig. 3.8. Comparison of two-dimensional (shown by squares) and three-dimensional (shown by diamonds) ray-tracing results. The top and bottom panels respectively show the L-shell and the group time delay at equatorial crossings for the nth hop. Both techniques generally agree for large n, t, though the two-dimensional program shows a plateau at $n = 32 - 35$, possibly due to numerical difficulties in handling waves with wave vectors close to the resonance cone.
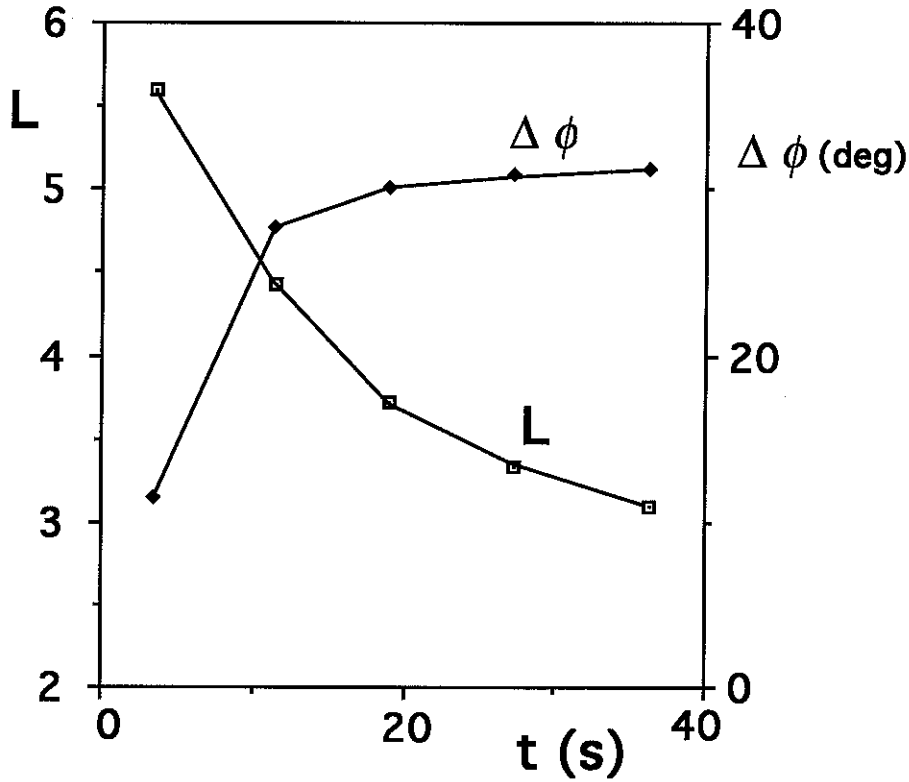
Fig. 3.9. L **values and the longitude drift** $\Delta\phi$ **of a 2.5 kHz quasi-electrostatic whistler mode wave in the magnetosphere.** The initial magnitude of the wave vector ($k = 0.75 \times 10^{-4}$ cm^{-1}) was chosen so as to provide a group time delay of $\sim$20 s at the third hop.

propagating at $L \sim 4$ is estimated as $t_{max} > 20$ s. The lifetimes for lower frequency waves propagating at lower L-shells can be substantially larger, up to $\sim 10^2$ s for a 1 kHz quasi-electrostatic whistler propagating at $L < 3$, in agreement also with numerical two-dimensional ray tracing calculations (see Section 3.2).

Figure 3.9 shows L values and drift in magnetic longitude $\Delta\phi$ for the first 5 equatorial plane crossings of a 2.5 kHz ray originating at a magnetic latitude of $\lambda = 45^o$. The initial wave vector was chosen to be $k = 0.75 \times 10^{-4}$ cm^{-1}. With the frame of reference as shown in Figure 2.2, the orientation of the transverse component of the wave vector

(parallel to the x' axis) was chosen to form the angle of 135° with the y axis. The magnitude of the initial azimuthal component of the wave vector under this condition was thus $k_\phi = k \cos 135^o \sim 5 \times 10^{-5}$ cm^{-1}. The electron Landau resonance energy $\mathcal{E} = \frac{m}{2}\left(\frac{\omega}{k_\parallel}\right)^2$ along the trajectory was determined numerically, and it was well above the thermal plasma energy for the first three equatorial plane crossings with $\mathcal{E} > 20$ eV, in general agreement with our analytical estimations. We note that the third hop of the wave propagated at $L \simeq 3.8$, i.e., where the observations reported in Figure 2.9 were made. The initial magnitude of the wave vector was chosen so as to provide a group time delay of $\sim$20 s. Rays with considerably greater initial values of k would be damped earlier and would not reach $L = 3.8$. However, rays originating from the same point and with the same frequency, but with smaller initial magnitude of the wave vector may propagate even further, executing the fourth and subsequent hops. As predicted by the scaling feature of (3.3.5), (3.3.14), (3.3.15), and (3.3.16), such rays would follow the same trajectory but would arrived at the same locations with smaller group delays. Figure 3.10 shows the range of group delays of the rays with different initial wave vectors in the range $k_{min} < k < k_{max}$ at their third crossing of the equatorial plane at L=3.8. Smaller group delays of the order of several seconds correspond to small initial magnitudes of the wave vector, where the quasi-electrostatic approximation is not valid, and are sketched by a dashed line.

The direction of propagation of whistler waves as observed at any point in the magnetosphere is determined by the propagation path of the wave energy from the source region to the observation point. Although whistler waves may initially have different wave vector orientations as a result of scattering from plasma irregularities, they may have approximately the same wave vector directions as observed on a satellite. Figure 3.11 shows positions of the third equatorial crossing of 2.5 kHz whistler rays with different initial wave vector directions as computed using our three-dimensional ray tracing model. The initial magnitude of the wave vector and the point of injection of the rays for Figure 3.11 are the same as those for Figure 3.9. We see that rays originating at
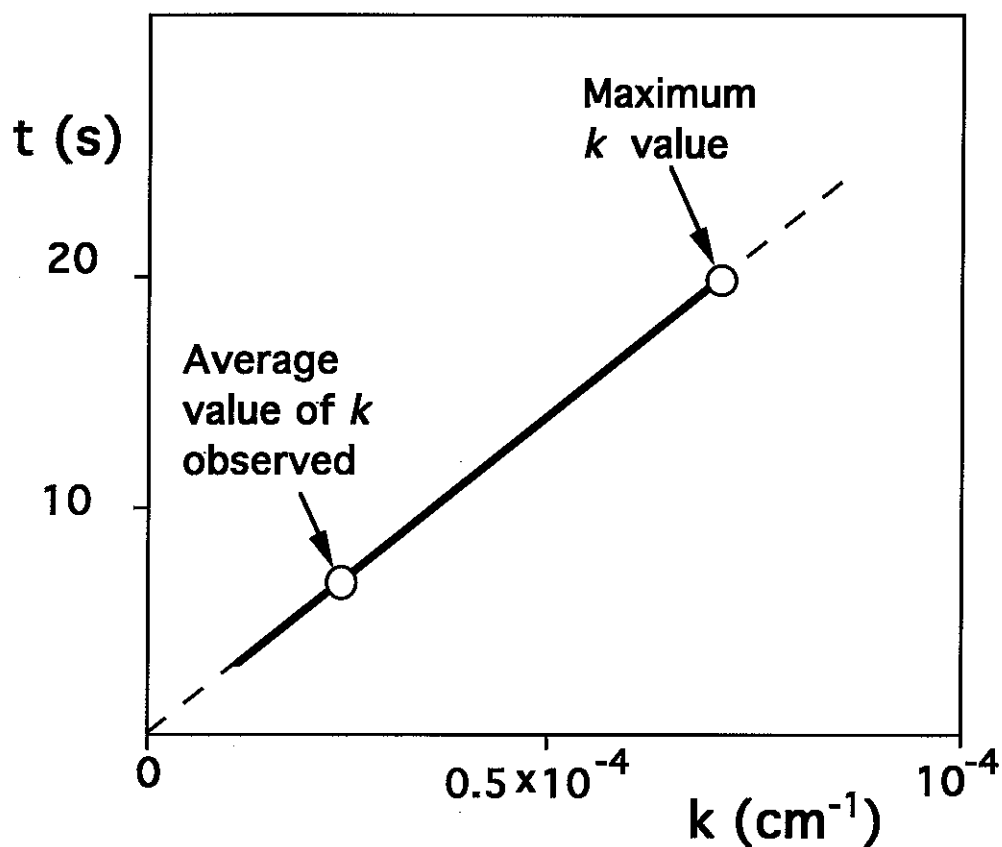
Fig. 3.10.   Calculated group delays and wave vectors of the third hop 2.5 kHz whistler waves as observed at $L=3.8$ in the magnetosphere. Maximum value of the wave vector k corresponds to the largest delay and is limited by Landau damping of the wave. The measured average magnitude of the wave vector for hiss corresponds to about one third of the maximum possible value and is shown by an arrow. Our analytical formulas are not valid for small values of k and t; this section is shown in a dashed line.
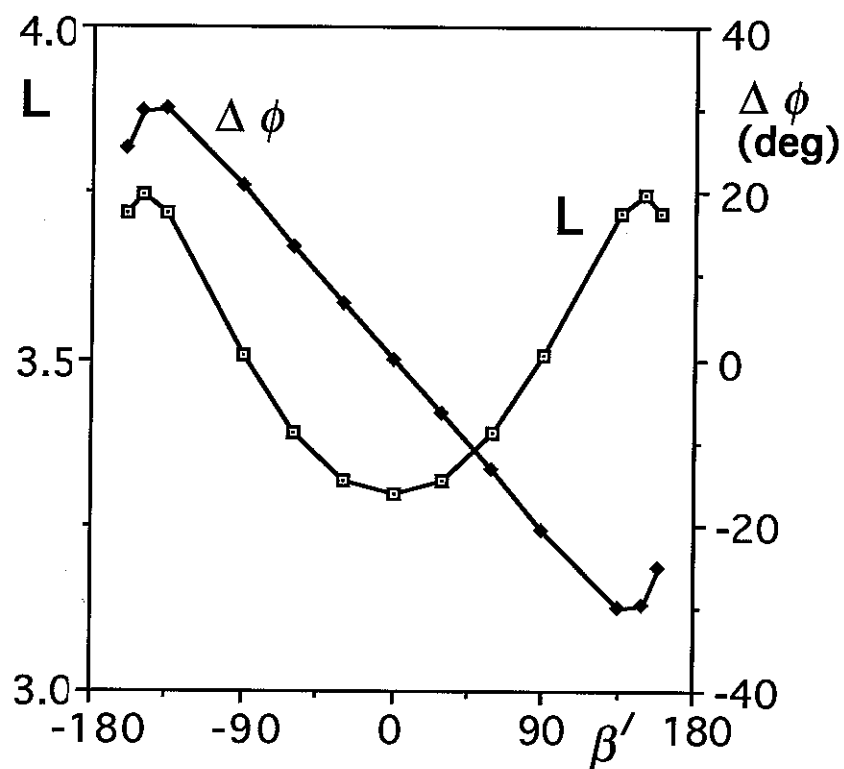
Figure 3.10

Fig. 3.11. L values and the longitude drift $\Delta\phi$ of 2.5 kHz whistler mode rays at the third equatorial crossing versus their initial azimuthal angle β' between the perpendicular component of the wave vector and the magnetic meridional plane. The value of β' is within a few degrees from the angle between axes x' and y in Figure 2.2

the same point with different initial azimuthal wave vector orientations can be observed at different L-shells and different longitudes. For example, if a satellite is located at $\sim$25-30° away in longitude from that of the source (e.g., thunderstorm) location, third-hop whistler rays should initially have azimuthal wave vector directions of $\sim$120-140° in order to be observable on the satellite. Results of our three-dimensional ray tracing calculations show that such rays would still have significant azimuthal wave vector components at the observation point in spite of the tendency for wave vectors to 'collimate' near the magnetic meridional plane [*Cairó and Lefeuvre*, 1986]. A manifestation of this effect in experimental data may be the case of the plasmaspheric hiss discussed in connection with Figure 2.9, which exhibits a significant azimuthal wave vector component, consistent with its having been produced by whistlers originating in thunderstorm centers at longitudes different from that of the observation point.

Figure 3.11 shows that magnetospherically reflected whistlers originating from the same thunderstorm center, populate a large but limited region of the magnetosphere (assuming that they originate from the same thunderstorm center). Since the group velocity direction depends on the wave frequency, the shape and dimensions of the regions of the magnetosphere populated by whistler wave energy should also depend on the wave frequency. Our three-dimensional ray tracing calculations show that whistler waves with higher frequencies propagate along trajectories qualitatively similar to those of lower frequency waves, but located at lower altitudes. For example, the points of the third equatorial crossing of 3.5 kHz rays are at $\Delta L \sim 0.6$, below those shown in Figure 3.11 for 2.5 kHz rays (all other parameters being the same). If the observation point is located in a region of the plasmasphere which is accessible to whistler waves from only a limited frequency band, hiss produced by whistlers and observed on a satellite may exhibit higher and/or lower frequency cutoffs, such as that at $\sim$2.9 kHz the data shown in Figure 2.9.

In our approximate analytical model, the wave group velocity is inversely proportional to the wave vector magnitude, and its direction is exactly perpendicular to the resonance

cone surface. We can estimate the validity of this quasi-electrostatic approximation by comparing the resonance cone angles to the measured wave normals of plasmaspheric hiss. Assuming a dipole model for the magnetic field, the resonance cone angles at the satellite location can be estimated as $\psi_r \sim 77^o$ for $f = 3.5$ kHz and $\psi_r \sim 81^o$ for $f = 2.5$ kHz. Since hiss wave normal angles were measured to be $\sim 70^o$ and $\sim 77^o$ respectively, they appear to be within few degrees from the resonance cone. Tests show that, for the parameters used here, our method predicts the direction of the group velocity to be $\sim 5^o$ farther from the direction of the magnetic field and the magnitude of the group velocity $\sim 20\%$ larger than those from the full cold plasma theory. The error of $\sim 20\%$ is of the same order as that which results from the uncertainty of the wave vector measurement, so that our approximate analytical ray tracing formulation is sufficiently accurate for the interpretation of the experimental data in hand.

3.5 ASSOCIATION OF HISS WITH LIGHTNING AND WHISTLERS

An important feature of the results presented in Figures 3.9 and 3.11 is that the drift in longitude of whistler mode waves is limited to $\sim 30^o$, which indicates that the group velocity lies almost in the magnetic meridional plane during the fourth and subsequent hops. Since the wave group velocity lies in the same plane as the wave vector and the magnetic field, this would in turn mean that the wave vector lies in the meridional plane. From a qualitative point of view this result can be explained as the growth of the radial component of the wave vector, while the azimuthal component does not change significantly (see (3.3.14) and (3.3.15)). After several tens of seconds, the radial component of the wave vector becomes large enough to tilt the wave vector toward the meridional plane, regardless of the initial value of the azimuthal component. This behavior of whistler waves is in agreement with the 'collimation effect' for azimuthal angles of whistler wave vector directions that was found using a numerical three-dimensional ray tracing approach [*Cairó and Lefeuvre*, 1986].

It is useful to compare the results of the ray-tracing study presented here to those

from Section 3.1, where the two-dimensional propagation of non-ducted whistlers with a narrow distribution of initial wave normal angles was studied. We have shown in Section 3.1 that over time periods of up to $\sim 10^2$ s, the whistler wave vectors tilted toward the resonance cone due to the magnetic field and plasma density gradients, and the resulting quasi-electrostatic whistler rays merged into a noise-like emission similar to hiss. The two-dimensional analysis of Section 3.2 showed that plasmaspheric hiss may be produced by whistler propagation at frequencies not too much higher than the local lower hybrid resonance (LHR) frequency. The results of our three-dimensional ray tracing of quasi-electrostatic waves indicate that wave frequencies do not need to be restricted to the vicinity of the LHR frequency if the wave vector has a significant initial azimuthal component. Although the existence of an azimuthal wave vector component is not necessary for hiss generation by whistlers, our model predicts that hiss should have a significant azimuthal wave vector component at frequencies well above the local LHR frequency.

The range of longitudes of the magnetosphere which can be illuminated by one lightning flash may be estimated as the sum by two quantities: (i) the range of longitudes in the vicinity of the lightning flash where the waves enter the ionosphere after propagation in the earth-ionosphere waveguide and (ii) the longitudinal spread of the waves during their propagation in the ionosphere and the magnetosphere. While the former quantity can be estimated as $\sim 10^o$ [*Carpenter and Orville*, 1989], the latter one can be estimated from our ray tracing calculations as $\sim 30^o$, so that plasmaspheric hiss should be observed within $\sim 40^o$ in longitude from its source. If hiss is generated by lightning, there should thus be a correlation between the distribution of the average plasmaspheric hiss intensity in longitude and the geographic regions of high thunderstorm activity. If hiss is generated primarily by energetic particles, its intensity should exhibit weak dependence on longitude, except during periods immediately after substorms, when the injected population of energetic particles is longitudinally dependent. A comprehensive survey of hiss intensity at low altitudes was recently reported [*Parrot*, 1990]. While the statistical data presented

show a prominent maxima of hiss intensity at longitudes of high thunderstorm activity ($\sim 250^{\circ}$E-320°E) (see [*Parrot,* 1990] and references therein), the relevance of this result to the problem in hand is not clear since most hiss, and in particular that which evolves from magnetospherically reflected whistlers would be confined to higher altitudes.

The measurements of hiss wave vector direction presented above show a local azimuthal anisotropy of hiss wave vector directions. In general, an azimuthal component of the hiss wave vector can be formed only if there is an azimuthal anisotropy of the hiss source distribution and/or azimuthal anisotropy of energetic particle distribution which might generate plasmaspheric hiss. While lightning activity as a possible source of hiss obviously has an azimuthal dependence, the distribution of the energetic particles in the magnetosphere is generally less dependent on longitude, with the exception of time periods immediately after magnetic storms, when injection of energetic particles takes place. In many cases discussed in Section 2.5, as well as that in Section 2.6, relatively quiet ($\Sigma K_p \sim$15-20) conditions prevailed, so that it is reasonable to assume only weak variation of the energetic particle distribution in longitude. Thus, the fact that there was indeed an azimuthal component of hiss wave normal angle in cases analyzed above is consistent with hiss generation by whistlers, rather than generation by energetic particles.

For propagation at large wave normal angles and in the presence of multiple magnetospheric reflections, the spread in group delays of signals originating at the same point below the ionosphere and observed at a fixed location (i.e., satellite) in the magnetosphere may be up to 20 s or more, according to Figure 3.9. This theoretical prediction may be manifested in satellite data, which show hiss-like signals lasting for $\sim 10 - 20$ s after the observed whistlers in the magnetosphere [*Sonwalkar and Inan,* 1989]. *Sonwalkar and Inan* [1989] ascribed this phenomena to the embryonic triggering of hiss by whistlers. While we do not reject the possibility of hiss amplification via wave-particle interaction, we note that the duration of the hiss-like signals observed after whistlers appear to be solely explainable by propagation effects alone. Since whistler waves at higher frequencies are damped after a shorter time, our proposed mechanism would lead to a higher

frequency cutoff in the hiss following whistlers, with lower frequencies lasting longer, precisely as observed in the experiment [*Sonwalkar and Inan*, 1989]. Another example of the same effect may be data presented by *Bell and Inan* [1981] and *Bell et al.* [1981], showing arrival time delays ranging up to 10-20 s for multiply reflected pulses from ground-based transmitters observed on the ISEE-1 satellite.

Since at any observation point wave spectral components with different wave vectors can be observed, our analysis of the spin fading characteristics provides an 'average' value of the magnitude of the wave vector as discussed in Section 2.2. This average value must necessarily be less than the maximum possible value of k as limited by the Landau damping condition discussed above. The average value of k corresponds to some average value of group delay, which must in turn be less than the maximum group delay estimated as $\sim$20 s at the third hop and shown with an arrow in Figure 3.10. Since the observed magnitude of k was $\sim 2.5 \times 10^{-5}$ cm^{-1}, i.e., about one third of the estimated maximum possible value, the average group delay should also be about one third of the maximum, i.e., $\sim$7 s. Therefore, at the observation point one can simultaneously observe signals from all whistlers originating up to at least 7 s before the time of the observation. Due to an extremely high whistler rate in the case analyzed here, there were several tens of whistlers during a 7 s period, each of them potentially contributing to the observed plasmaspheric hiss. Signals from different whistlers lasting on average for $\sim$7 s each, would overlap and completely lose their initial discrete character. Thus, it is possible that the plasmaspheric hiss shown in Figure 2.9 might have been produced entirely by nonducted oblique whistlers.

While propagating through the ionosphere, whistler wave energy may be split between scattered quasi-electrostatic waves and non-scattered electromagnetic waves. As we show in this paper, quasi-electrostatic waves may form hiss on time scales of $\sim$7 s due to the spread in their velocity of propagation. Non-scattered whistler rays would propagate without any significant spread in group delay, and therefore would be observed as discrete whistlers on a satellite. Observed cases of discrete whistlers superposed on hiss (Figure

2.9) may be a manifestation of such a split of whistler energy. For discrete whistlers which have not scattered during their propagation to the observation point, the wave vector orientation would be determined solely by magnetic field and plasma density gradients, and the wave vector would not significantly deviate from the meridional plane, in agreement with our measurements. Upon further propagation, the wave vectors of the discrete whistlers would approach the resonance cone, so that on longer time scales ($\sim 10^2$ s) their low-frequency components may also evolve into plasmaspheric hiss as shown above.

3.6   SUSTENANCE OF HISS ENERGY BY LIGHTNING

While the data presented above show that some plasmaspheric hiss may be produced by multiply reflected whistlers, additional work has to be done in order to investigate what fraction of hiss may indeed be produced by lightning on a global scale.

To estimate the total hiss energy, we start from the relation for the energy density (per unit volume) of the oblique whistler mode wave

$$q_h = \frac{|[\vec{E}_h \times \vec{B}_h]|}{4\pi} \frac{c}{v_g}$$

Substituting the electric field value from the Maxwell's equations, we find

$$q_h = \frac{B_h^2}{4\pi} \frac{c}{v_g} \frac{1}{n_h \sin \alpha} \qquad (3.6.1)$$

where B_h is the total wave magnetic field, n_h is the refractive index and α is the average (over one period) angle between the electric field of the wave and the wave vector. The latter two parameters can be determined through a solution of the full dispersion equation for the oblique whistler wave employing the dielectric permittivity tensor in the form given by (2.3.6)-(2.3.7). The numerical solution of the dispersion equation

performed with APM code* [Chmyrev et al., 1991] leads to $\frac{c}{v_g} \frac{1}{n_h \sin\alpha} \sim 1$ for typical magnetospheric parameters and for k values of $\sim 2 \times 10^{-5} - 7 \times 10^{-5}$ cm^{-1} as obtained above. We note that for the same wave magnetic field intensity, the hiss energy density would be higher for larger k, since for large k the wave becomes more electrostatic, and a larger fraction of its energy is concentrated in the electric field, which is not measured by the magnetic antenna. Quantitatively, this effect would manifest itself as lower values of $\sin\alpha$ in (3.6.1). This trend is illustrated by Figure 3.12 which shows the refractive index n, a cross section of the wave vector surface, B/E ratio and $\sin\alpha$ for a 1 kHz whistler wave in the plasma with density of 500 cm^{-3} and parameters corresponding to the magnetic equator at $L = 4$.

We use the hiss energy density to estimate the total rate of energy loss of the hiss wave in the magnetosphere as $Q_h = q_h V \frac{1}{\tau_h}$, where $V \sim 2 \times 10^{22}$ m^3 is the total volume of the magnetosphere occupied by plasmaspheric hiss (assumed here to be the region limited by $2 < L < 4$ and $-40^o < \lambda_m < 40^o$), and τ_h is the lifetime of the whistler waves in the magnetosphere. Although the particular case analyzed in this paper refers to relatively high hiss frequencies ($f \sim$2-3 kHz), the major concentration of hiss energy is typically at or near $\sim$1 kHz [Thorne et al., 1973]. As shown in Section 3.1, nonducted whistlers may evolve into plasmaspheric hiss at frequencies of order 1 kHz after several tens of magnetospheric reflections. On this basis, we choose to make comparison of hiss and whistler energy densities by using observed hiss spectral densities at $\sim$1 kHz. We adopt the value of $\sim$1 pT/Hz$^{1/2}$ in a 300 Hz frequency band as reported by Thorne et al. [1973]. Substituting $\tau_h \sim$20 s, we find $Q_h \sim 3 \times 10^5$ J/s.

We compare this value to the total energy input from whistlers into the magnetosphere, which can be estimated as

$$Q_w = \frac{B_w^2}{4\pi} \frac{c}{n_w} S \tau_w I_l \qquad (3.6.2)$$

---

* This is a general warm plasma code which for a given wave frequency allows the determination the frequency, the wave vector, the damping rate and polarization characteristics for the warm multicomponent magnetoplasma.
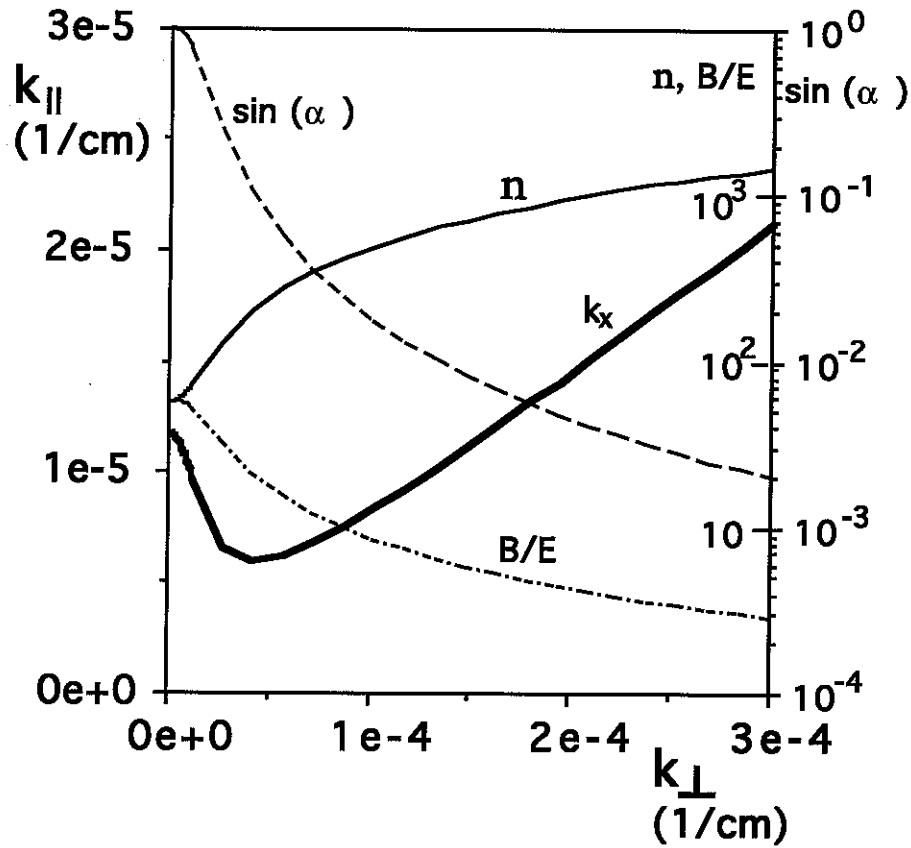
Fig. 3.12. The refractive index n, a cross section of the wave vector surface, B/E ratio and $\sin \alpha$ for a 1 kHz whistler wave A purely hydrogen plasma is assumed with density of 500 cm^{-3} and magnetic field corresponding to the magnetic equator at $L = 4$.

where B_w is the whistler wave amplitude, n_w is the refractive index, τ_w is the whistler duration at the equatorial plane, S is the area illuminated by an average whistler in the equatorial plane, and I_l is the global rate of lightning discharges. The latter parameter can be estimated as $I_l \sim 10^2$ s^{-1} [Uman, 1987]. Though the area illuminated by a whistler can be significantly larger than the magnetospheric projection of the spot of whistler entrance in the ionosphere due to azimuthal drift of whistler rays, we conservatively neglect the azimuthal divergence of whistler rays in our estimates. Taking the azimuthal dimension of the whistler illumination region at the lower ionosphere to be $\sim$2000 km [Carpenter and Orville, 1989], and assuming that whistler rays cross the equatorial plane

at $2 < L < 4$ (as follows from ray tracing calculations), we estimate $S \sim 6 \times 10^7$ km^2. For a whistler wave amplitude of ~3 pT (consistent with satellite observations [*Sulič et al.*, 1991]), refractive index of ~30, and typical duration of ~0.3 s we estimate the whistler wave energy input into the magnetosphere to be $Q_w \sim 2 \times 10^5$ J/s. Since Q_w is comparable to Q_h, lightning generated whistlers can indeed provide a significant portion of the energy needed to maintain the 1 pT/Hz$^{1/2}$ hiss intensities on a global scale.

Our mechanism of hiss generation does not rule out the possibility of wave amplification due to wave-particle interactions [*Church and Thorne*, 1983], so that the observed intensity levels of the plasmaspheric hiss may be a result of both hiss generation by non-ducted whistlers and its subsequent amplification by the interaction with energetic electrons. We also note that our ray tracing calculations in fact show that the whistler wave energy from lightning discharges should be inhomogeneously distributed in longitude, exhibiting correlation with thunderstorm activity. Therefore, while our energy estimates are based on azimuthally averaged values, the local values of both hiss energy density and lightning generated whistler energy might be significantly different.

3.7 MAGNETOSPHERIC REFLECTION OF WHISTLER RAYS WITH $\omega < \omega_{LHR}$

Ray tracing modeling of magnetospheric whistler wave propagation presented in this Chapter was limited to frequencies above the local lower hybrid frequency. While the major part of magnetospheric hiss is observed above the local lower hybrid resonance frequency ω_{LHR}, observations of hiss with $\omega < \omega_{LHR}$ are not uncommon [e.g., *Church and Thorne*, 1983, see Figure 1]. In this section we provide qualitative discussion of propagation in the magnetosphere of whistler waves with $\omega < \omega_{LHR}$. We show that such waves are subject to magnetospheric reflection similar to that for higher frequency $(\omega > \omega_{LHR})$ waves. Therefore, it is potentially possible that hiss below the local lower hybrid frequency may be formed by multiply reflecting whistlers, similar to the higher

frequency hiss. Comprehensive consideration of hiss propagation below ω_{LHR} is a topic of future research.

It is known that the refractive index surface for whistler mode waves with $f < f_{LHR}$ is closed, in contrast to the open refractive index surface for $\omega < \omega_{LHR}$ [*Stix*, 1962]. This means that the magnitude of the transverse component of the wave vector is limited for $\omega < \omega_{LHR}$. For a wave frequency just below the local lower hybrid frequency, the refractive index surface resembles that for frequencies just above ω_{LHR}, i.e., $k_\perp$ may have large (but bounded) values. These qualitative considerations are illustrated by Figure 3.13, where the refractive index surfaces are plotted for different ω_H, ω_{LHR}. The general trend is that the largest possible value of the transverse component of the wave vector increases monotonically with decreasing ω_H.

Let us qualitatively consider oblique whistler mode wave propagation in the magnetosphere. When a ray propagates in the inhomogeneous magnetic field, its frequency remains constant (assuming stationary magnetosphere). However, due to the inhomogeneity of the medium, both the perpendicular and the parallel components of the wave vector are subject to variations along the raypath. The variation of the transverse component is determined by plasma parameter gradients across the magnetic field lines. It is difficult to assess qualitatively the evolution of the transverse wave vector component, but based on the results of our two-dimensional ray tracing calculations, we can assume that it steadily grows during the wave propagation. We consider the propagation of a whistler mode wave with frequency below the local lower hybrid frequency and wave vector having a perpendicular component in the direction of higher L-shells. Since the group velocity of whistler mode waves is perpendicular to the refractive index surface, it should have components along the magnetic field line ($v_\parallel$) and another one directed toward higher L-shells ($v_\perp$) (see Figure 3.13). If the wave propagates from the magnetic meridian towards higher latitudes, the local magnetic field increases due both to changes in latitude and in L-shell. Since almost everywhere in the plasmasphere $\omega_{LHR} \sim (\omega_{He}\omega_{Hi})^{1/2}$ (see formula (1.2.2) for $\omega_{pe} \gg \omega_{He}$), the increase of the local
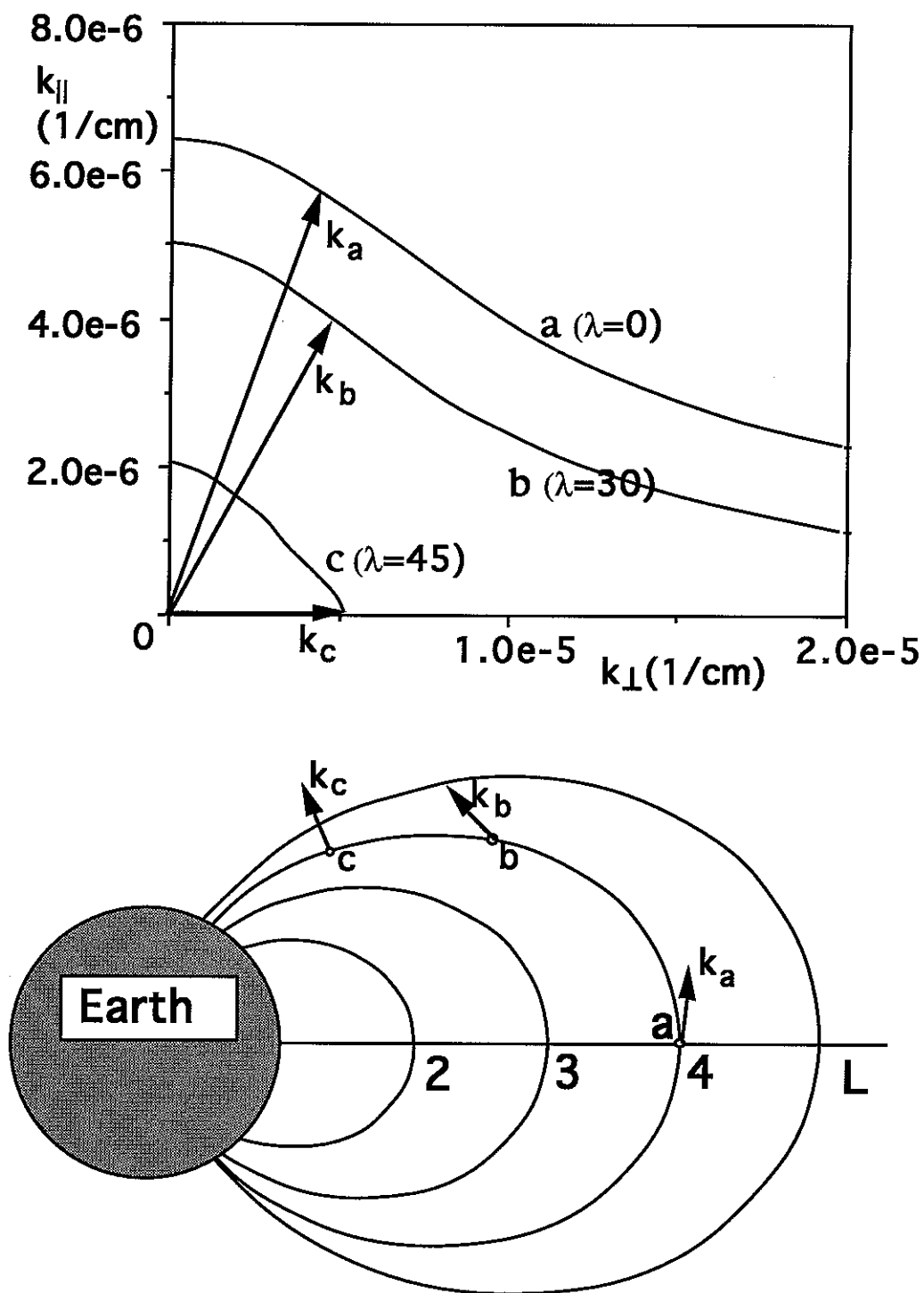
Fig. 3.13.   Refractive index surfaces for $\omega < \omega_{LHR}$ **at three different points** a, b **and** c **along the magnetic field line.**   Vectors $\vec{k}_a$, $\vec{k}_b$, and $\vec{k}_c$ represent the evolution of the wave vector as the wave propagates toward higher latitudes.

magnetic field is accompanied by an increase in the local LHR frequency. Therefore, if the wave frequency is lower then ω_{LHR} at some point along the trajectory, the difference between ω_{LHR} and ω increases during the wave propagation toward higher latitudes.

As we have seen from Figure 3.13, a larger difference between the LHR frequency and the wave frequency results in a lower limit to the magnitude of the transverse component of the wave vector ($k_\perp$). Therefore, if we plot the local refractive index surfaces along the ray trajectory, we should see their transverse dimensions decrease, and the transverse component of the wave vector at some point of the ray trajectory reach the maximum value allowed by the refractive index surface. This situation is qualitatively sketched in Figure 3.13, where three local refractive index surfaces are shown, for points a, b and c along the ray trajectory, the outer one (marked a) corresponding to lower latitudes, and the inner ones (marked b, c) corresponding to higher latitudes. If the wave has a wave vector $\vec{k}_a$ as shown in the Figure 3.13 at low latitudes, we may assume the transverse component of the wave vector to increase, resulting in a wave vector of $\vec{k}_b$ at the intermediate point b. When the trajectory reaches point c, the magnitude of $k_\perp$ may now be equal to the maximum possible value as shown in Figure 3.13. Since the wave group velocity is always perpendicular to the refractive index surface, the wave propagates exactly across the magnetic field lines at the point c, so that c is a turnaround (or reflection) point for the ray trajectory and the wave starts to propagate back towards lower latitudes. Therefore, whistler mode waves with frequencies below the local lower hybrid frequencies are subject to bouncing between the hemispheres [*Edgar*, 1976] similarly to higher frequency waves.* In fact, we did not use any assumptions on the wave frequency in the equatorial region, so that the mechanism of the wave reflection described above would work regardless of whether the wave frequency is higher or lower than ω_{LHR} at the equator. In both cases, the ray is reflected beyond the point where the wave frequency is equal to the local lower hybrid frequency. For waves with large $k_\perp$

---

* Bouncing of whistler mode waves with $\omega < \omega_{LHR}$ corresponds to first three magnetospheric reflections in Figure 3.1.

the turnaround occurs over a short extent of the raypath, and the wave does not penetrate significantly into the region where $\omega < \omega_{LHR}$. In this case, the process is similar to reflection from the surface where $\omega = \omega_{LHR}$. For waves with lower values of $k_\perp$, the wave may penetrate deeply into the region where $\omega < \omega_{LHR}$, and a significant part of the ray trajectory may lay in this region.

The above considerations show that there is no qualitative difference between magnetospheric propagation of whistler rays with $\omega < \omega_{LHR}$ and $\omega > \omega_{LHR}$. In both cases rays may bounce between hemispheres, and the wave energy may be stored for extended periods within the magnetosphere. Therefore, there is a possibility that the mechanism of hiss generation by multiply reflecting whistlers as suggested here and demonstrated extensively and quantitatively for $\omega > \omega_{LHR}$ may also be similarly valid for $\omega < \omega_{LHR}$. The comprehensive investigation of the possibility of generation of hiss with $\omega < \omega_{LHR}$ is a topic of future research.

4

Some aspects of hiss interaction with electrons

4.1 INTRODUCTION

Pitch angle diffusion of energetic electrons due to their interaction with whistler mode waves has long been suggested as an important cause of electron precipitation into the lower ionosphere. A self-consistent theory of this phenomenon was presented in the pioneering work by *Kennel and Petschek* [1966]. Later, this theory was elaborated by *Etcheto et al.* [1973], where an iteration technique was used to find a solution for the problem of plasmaspheric hiss interacting with energetic electrons. *Lyons et al.* [1972] studied the pitch angle diffusion of radiation belt electrons due to interaction with whistler waves having a Gaussian distribution of the wave energy with respect to the wave normal angles with a maximum at $\psi = 0$. The model by *Lyons et al.* [1972] took into account the interaction of oblique waves with particles at all cyclotron harmonic resonances and the Landau resonance and evaluated diffusion coefficients at different geomagnetic latitudes. However, in view of the results of our hiss wave normal measurements (Chapter 2), the assumption of hiss wave energy having a maximum at small wave normal angles [*Lyons et al.*, 1972] is difficult to justify. Another problem with the *Lyons et al.* [1972] theory

is that local effects of the medium inhomogeneity have not been taken into account (although diffusion coefficients were integrated along the magnetic field line, at each point along the trajectory they were calculated as if in a homogeneous media).

In a contrast to the analytical theory of *Lyons et al.* [1972], test particle calculations have a significant advantage of being able to take full consideration of the inhomogeneity of the medium [e.g., *Inan et al.*, 1978]. As shown by *Inan et al.* [1978], mirror forces due to the varying magnetic field are the primary factor which determine the length of electron interaction with discrete whistlers, so that one can assume that magnetic field inhomogeneity may also play an important role in the local interaction of electrons with hiss. In *Inan* [1987], similar methods were used to evaluate the electron precipitation due to interaction with a broadband signal, which was modelled by a sequence of short monochromatic pulses. By comparing the pitch angle scattering and precipitation fluxes resulting from interaction with coherent and incoherent waves, *Inan* [1987] showed that although the net scattering of individual electrons were substantially smaller for incoherent waves, many more electrons (than for a coherent wave) were scattered due to larger bandwidth, so that the precipitated flux was about the same for coherent versus incoherent waves. Again using a test particle formulation, *Jasna et al.* [1992] recently showed that interaction of suprathermal electrons with discrete oblique whistlers results in larger precipitation fluxes, as compared to the case of interaction with parallel propagating whistlers.

In this Chapter, we provide preliminary analytical estimates for electron pitch angle diffusion due to interaction with oblique whistler mode waves. We also take into account the inhomogeneity of the medium in our estimates. As we show below, both the inhomogeneity and the high wave normal angles significantly affect the rate of diffusion. These results are in qualitative agreement with earlier numerical results *Inan et al.* [1978] and *Jasna et al.* [1992], and can be a basis for future theoretical modeling of energetic electron interaction with oblique hiss waves in the inhomogeneous magnetosphere.

We first discuss in Section 4.2 the resonant energies of electrons which can interact with oblique whistler mode waves. A general theory of electron diffusion is reviewed in Section 4.3. Section 4.4 gives estimates of the variation of electron velocity due both to wave-particle interaction and mirror forces, showing that the medium inhomogeneity represented by the mirror force) is indeed the primary factor determining the length (duration) of the electron resonance with hiss spectral components. We estimate the diffusion coefficient for electrons by using the contribution from the mirror force in Section 4.5, summarizing estimates for electron diffusion due to their interaction with obliquely propagating hiss in the inhomogeneous magnetosphere.

4.2 RESONANT ENERGIES FOR ELECTRON INTERACTION WITH OBLIQUE WHISTLER WAVES

Particles interact resonantly with the wave if their velocity satisfies the condition [*Krall and Trivelpiece*, 1973]:

$$\omega - k_{\parallel} v_{r\parallel} = \nu \omega_H \tag{4.2.1}$$

where $v_{r\parallel}$ is the parallel component of the resonant velocity of electrons, and ν is an integer. The case with $\nu = 0$ is referred as the Landau or Čerenkov resonance, and $\nu = 1$ corresponds to the first order gyroresonace. In general, the three resonances with $\nu = 0, \pm 1$ make larger contribution to electron pitch angle scattering as compared to higher order resonances [*Lyons et al.*, 1972]. For the sake of simplicity, we consider below only the first gyroresonance.

We can see from (4.2.1) that for a fixed wave frequency, smaller values of $k_{\parallel}$ correspond to larger $v_{r\parallel}$. Figure 4.1 shows a cross section of a whistler-mode refractive index surface, which defines the relation between the perpendicular and parallel components of the wave vector so as to satisfy the dispersion equation for whistler waves in a cold plasma for a given frequency ($L=4$ at the magnetic equator, $n=500$ cm^{-1}, $f=1$ kHz). The smallest value of $k_{\parallel}$ (or the largest $v_{r\parallel}$) corresponds to wave propagation in the Gendrin mode. For

wave normal angles greater than the Gendrin angle, resonant energies become lower. Near the resonance cone, $k_{\parallel}$ becomes very large, so that electrons of suprathermal energies may interact with the wave. As was seen in the wave normal analysis of DE-1 data (Chapter 2), typical wave normal angles for hiss lie at or beyond the Gendrin angle. Therefore, spectral components of oblique hiss may interact with electrons over a broad range of energies, including both energies higher and lower than those which interact with quasi-parallel propagating whistler mode waves of the same frequency.

4.3 GENERAL THEORY OF ELECTRON DIFFUSION IN THE MAGNETOSPHERE

A semi-rigorous derivation of a diffusion coefficient for gyroresonant interactions is given by *Kennel and Petschek* [1966]. The main idea is that, at any given time, electrons effectively interact with wave components in a narrow spectral range (with width Δk in wave vector space), so that the magnitude and polarity of the wave forces they experience depend on the relative phase difference between their gyromotion and the phase of that component of the wave. After a time Δt, electrons move from resonance with one narrow spectral range to another. If the phases of the two spectral components are not correlated, then changes in electron velocity due to the interaction with different spectral bands are also not correlated, and the electrons execute a random walk in velocity space. This concept allows the evaluation of the diffusion coefficient D for electrons as (equation (3.7) [*Kennel and Petschek*, 1966], slightly modified)

$$D \simeq C B_k^2 \Delta k \Delta t \qquad (4.3.1)$$

where the expression for C may be given through the wave frequency and external magnetic field strength, and B_k is the wave spectral density in wave number space. From (4.3.1) we see that the value of the diffusion coefficient depends on the interaction time Δt during which the electrons are in resonance with the wave-number band of width Δk. Accurate estimation of the product $\Delta k \Delta t$ is important for the quantitative application
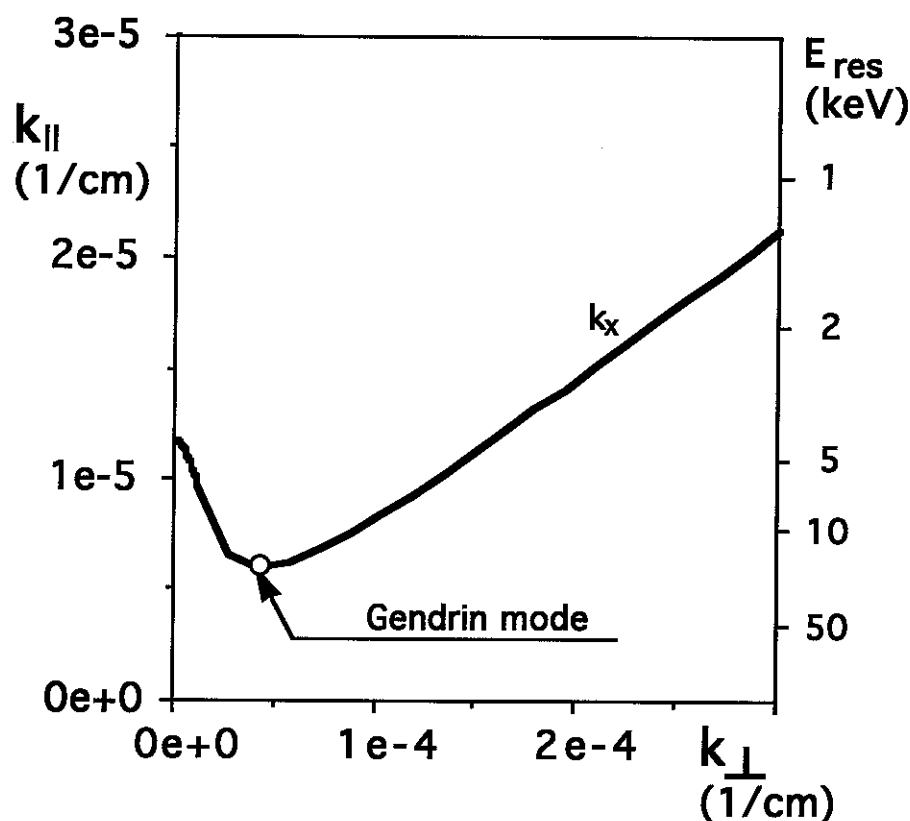
Fig. 4.1. **Perpendicular and parallel components of the wave vector which satisfy the dispersion equation for whistler waves in a cold plasma for a given frequency** (L=4 at the magnetic equator, n=500 cm^{-1}, f=1 kHz). The smallest value of $k_\parallel$ (or the largest value of the electron resonant energy) corresponds to the wave propagation in the Gendrin mode. For wave normal angles larger than the Gendrin angle, resonant energies become lower. Near the resonance cone, $k_\parallel$ becomes very large, so that electrons of suprathermal energies may interact with the wave [*Inan and Bell*, 1991; *Jasna et al.*, 1992].

of the theory of electron diffusion. In *Kennel and Petschek* [1966], Δt is estimated as the time during which the phase of the particle's gyromotion changes by 1 radian with respect to the phase of the spectral components which are at the edges of the spectral band (i.e., $\pm \Delta k/2$), yielding

$$\Delta t \simeq \frac{2}{\Delta k v_\parallel} \tag{4.3.2}$$

Note, that Δt is inversely proportional to Δk, so that in Kennel-Petschek theory the width of the resonance band Δk (or the interaction time Δt) may be chosen ambiguously, as long as the product of these two quantities is constant.

While this approach results in an accurate value of the diffusion coefficient [*Galeev and Sudan*, 1983], more rigorous derivation of the electron velocity diffusion in a homogeneous plasma accounts for the variation of the velocity of a particle due to its interaction with the wave, which in turn causes the electrons to move from resonance with one wave component to another [see *Galeev and Sudan*, 1983 and references therein]. This approach leads to a somewhat different expression for the time of interaction

$$\Delta t' \simeq \frac{2}{k \Delta v_\parallel} \tag{4.3.3}$$

where $\Delta v_\parallel$ is the change of electron parallel velocity due to interaction with the wavenumber band of width Δk. In the Galeev and Sudan approach, special consideration must be given to the choice of Δk, since it determines the numerical value for D. The Kennel-Petschek and Galeev-Sudan approaches give the same numerical results, since it can be shown that*

$$\Delta k v_\parallel \simeq k \Delta v_\parallel \tag{4.3.4}$$

We note that both approaches implicitly assume that electrons move from one resonance to another due to their interaction with the waves. In the case of electron diffusion in the

---

* See the discussion for (4.4.15) in the next Section.

magnetosphere, however, the electron velocity varies due both to wave-particle interaction and mirror forces resulting from the magnetic field inhomogeneity. The latter has been shown to be the primary factor responsible for the time of interaction, in the case of electron interaction with monochromatic signals [e.g., *Inan et al.*, 1978] or with broadband incoherent waves [*Inan*, 1987]. In the following, we provide the analytical basis for a diffusion theory which accounts for both oblique propagation and the inhomogeneity of the medium. In order to compare the relative contributions of the inhomogeneity and the wave-particle interaction, we must calculate $\Delta v_{\parallel}$ due both to the wave forces and the adiabatic forces. As we mentioned above, in the Kennel-Petschek approach electrons interact with a spectral component of unspecified width Δk, so that the numerical value of the variation of the electron velocity due to interaction with a narrow spectral component can not be determined. Therefore, to compare contributions from the mirror force and from the wave-particle interaction, we use the Galeev-Sudan approach.

4.4 VARIATION OF THE ELECTRON VELOCITY DUE TO THE WAVE-PARTICLE INTERACTION

In this section we calculate the change in the parallel component of the velocity of an electron which results from its interaction with a narrow spectral component of an obliquely propagating whistler mode wave. We start from the equation of motion for electrons in the electromagnetic field of the wave and in the homogeneous ambient earth magnetic field

$$\frac{d\vec{v}}{dt} = -\frac{e}{m}\left\{\vec{E} + \frac{1}{c}[\vec{v} \times \vec{H}]\right\} \tag{4.4.1}$$

A typical method for solving (4.4.1) is to expand $\vec{v}$ in a power series with respect to the wave field, and find a solution by iteration [*Krall and Trivelpiece*, 1973]. In the zero order approximation with respect to the wave field (i.e., neglecting the electromagnetic field of the wave), the electron motion is a helical gyration in the earth's magnetic field

$$v_x = v_{\perp} \cos(\omega_H t + \phi) \tag{4.4.2a}$$

$$v_y = v_\perp \sin(\omega_H t + \phi) \tag{4.4.2b}$$

$$v_z = v_\| \tag{4.4.2c}$$

where ω_H is the electron gyrofrequency. The electron trajectory (i.e., position in physical space) may be obtained by integrating equations (4.4.2) as

$$r_x = \rho \sin(\omega_H t + \phi) \tag{4.4.3a}$$

$$r_y = -\rho \cos(\omega_H t + \phi) \tag{4.4.3b}$$

$$r_z = v_\| t + r_0 \tag{4.4.3c}$$

where $\rho = \frac{v_\perp}{\omega_H}$. This zero order solution can be substituted in the right-hand part of (4.4.1) (so that electromagnetic field intensities of the wave are evaluated at the coordinates given by (4.4.3)) to find the first order approximation for the electron motion. Since we are interested the time it takes the electron to move from one resonance to another, and the resonant condition (4.2.1) employs the value of the electron parallel velocity, we need only to evaluate the variation of the parallel component of the electron velocity. From (4.4.1) we find for the average value of the electron velocity

$$\frac{dv_\|}{dt} = -\frac{e}{m}\left(<E_\|> + \frac{1}{c} <[\vec{v} \times \vec{H}]> \right)_\| \tag{4.4.4}$$

where $<.>$ denotes averaging over time periods which are much larger than the wave period but smaller than the time of interaction. To simplify the right hand side of (4.4.4), we use expressions for the electromagnetic field of the wave

$$\vec{E} = \frac{1}{2}\left(\vec{e}E_0 \exp(i(\omega t - \vec{k} \cdot \vec{r})) + c.c. \right) \tag{4.4.5a}$$

$$\vec{H} = [\vec{\mu} \times \vec{E}] \tag{4.4.5b}$$

where $\vec{e}$ is the complex polarization vector of the whistler mode waves as defined by (2.3.5), c.c. denotes the complex conjugate term, and $\mu = \frac{c\vec{k}}{\omega}$ is the refractive index. As we discussed above, the exponent in (4.4.5) should be evaluated at the position of the particle as defined to zero order by (4.4.3). Limiting our consideration to the first order gyroresonance for which $\nu = 1$ and $\omega - k_{\parallel}v_{\parallel} = \omega_H$, we find

$$\exp(i(\omega t - \vec{k} \cdot \vec{r})) \simeq \exp(i(\omega_H t - k_{\parallel}r_0))\Big(J_0(k_{\perp}\rho) + iJ_1(k_{\perp}\rho)\sin(\omega_H t + \phi)\Big) \quad (4.4.6)$$

where $J_0()$ and $J_1()$ are Bessel functions of the first kind and zero and first order respectively. Substituting (4.4.5),(4.4.6) and (4.4.2) into (4.4.4) and time averaging the products of rapidly varying sine, cosine and exponents, we obtain the expression for the slow variation of the electron parallel velocity

$$\frac{dv_{\parallel}}{dt} = -\frac{e}{2mc}E_0 v_{\perp} J_0(k_{\perp}\rho)\Big(\mu_{\parallel}|e_x|\cos(\phi + k_{\parallel}r_0 - \theta_x)$$

$$+\mu_{\parallel}|e_y|\sin(\phi + k_{\parallel}r_0 + \theta_y) - \mu_{\perp}|e_z|\cos(\phi + k_{\parallel}r_0 - \theta_z)\Big)$$

$$-\frac{ieJ_1(k_{\perp}\rho)}{2m}|e_z|E_0\sin(\phi + k_{\parallel}r_0 + \theta_z) \quad (4.4.7)$$

where the angles θ_j are defined by $e_j = |e_j|\exp(i\theta_j)$ and $j = x, y, z$. Taking into account the fact that $J_1(k_{\perp}\rho) < k_{\perp}\rho$ for all values of $k_{\perp}\rho = \frac{k_{\perp}v_{\perp}}{\omega_h}$, we can estimate the term containing J_1 in (4.4.7) as

$$\frac{ieJ_1(k_{\perp}\rho)}{2m}|e_z|E_0\sin(\phi + k_{\parallel}r_0 + \theta_z) < \frac{e}{2m}\frac{k_{\perp}v_{\perp}}{\omega_h}|e_z|E_0 \quad (4.4.8)$$

Since for typical hiss frequencies $\omega \ll \omega_H$, the left hand side of (4.4.8) (i.e., the last term in (4.4.7)) is small compared to another term in (4.4.7) containing $|e_z|$

$$\frac{e}{2m}\frac{k_{\perp}v_{\perp}}{\omega_h}|e_z|E_0 \ll \frac{e}{2mc}E_0 v_{\perp} J_0(k_{\perp}\rho)\mu_{\perp}|e_z|\cos(\phi + k_{\parallel}r_0 - \theta_z) \quad (4.4.9)$$

Therefore, equation (4.4.7) can be rewritten as

$$\frac{dv_\parallel}{dt} \simeq -\frac{e}{2mc} E_0 v_\perp J_0(k_\perp \rho)\Big(\mu_\parallel |e_x| \cos(\phi + k_\parallel r_0 - \theta_x)$$

$$+\mu_\parallel |e_y| \sin(\phi + k_\parallel r_0 + \theta_y) - \mu_\perp |e_z| \cos(\phi + k_\parallel r_0 - \theta_z)\Big) \qquad (4.4.10)$$

We can see from (4.4.10) that the sign and the magnitude of the forces affecting the particle depend on the gyrophase ϕ of the particle with respect to the wave phase. The next (second) order approximation can be found in a similar way, by integrating (4.4.10) and substituting in (4.4.5) and then in the right hand side of (4.4.1). This procedure would result in an oscillating solution for the parallel velocity of electrons, so that they are trapped by the wave [*Bell*, 1986].

Though the evaluation of the expression in parentheses in (4.4.10) can only be made by numerical methods, we note that the value of this term is smaller for quasi-electrostatic whistler waves. In such a case, the electric field is almost parallel to the wavevector (which is assumed to be in x, z plane), so that $\theta_x = \theta_z = 0; e_x \simeq \frac{\mu_\perp}{\mu}; e_z \simeq \frac{\mu_\parallel}{\mu}; |e_y| \ll e_x, e_z$. Substituting in (4.4.10), we can see that the maximum value of the expression in the parentheses contains two terms: (i) a term proportional to the small average angle between the $\vec{E}$ component in the x, z plane and the wave vector; (ii) a second term proportional to the small e_y value. Small values of these quantities are qualitatively understandable, since most of the energy of a quasi eletrostatic whistler wave resides in the electric field (i.e., $B \ll E$), so that the right-hand side of (4.4.4) has smaller value for oblique waves as compared to parallel propagating waves. To simplify the right-hand side of (4.4.10), we define

$$R = J_0(k_\perp \rho)\Big(\mu_\parallel |e_x| \cos(\phi + k_\parallel r_0 - \theta_x)$$

$$+\mu_\parallel |e_y| \sin(\phi + k_\parallel r_0 + \theta_y) - \mu_\perp |e_z| \cos(\phi + k_\parallel r_0 - \theta_z)\Big)$$

To estimate R we can neglect the small second term containing e_y, and note that in view of $\theta_x = \theta_z = 0$ and the assumption of the wavevector being in the x, z plane (i.e., $k_\parallel = k_z, k_\perp = k_x$) we can rewrite R in the form

$$R \simeq J_0(k_\perp \rho) \frac{ck}{\omega} \left(\frac{k_z}{k} e_x - \frac{k_x}{k} e_z \right) \cos(\phi + k_\parallel r_0) \qquad (4.4.11)$$

Therefore, R is of order of $J_0(k_\perp \rho)\frac{ck}{\omega} \sin \alpha_{E,k}$, where $\alpha_{E,k}$ is the angle between the wave vector and the projection of the polarisation vector $\vec{e}$ to the wave vector plane. Since the change in the particle parallel velocity is caused by the term which contains H in (4.4.4), and since it follows from (4.4.5b) that $H \sim \frac{ck}{\omega} \sin \alpha_{E,k} E$, it is understandable that $RE_0 \sim H$. Thus, if the wave amplitude is measured by a magnetic antenna, we would get the same order of magnitude change in $v_\parallel$ for oblique and for parallel waves assuming the same amplitude of the wave magnetic field. However, if we compare the change in the electron parallel velocity for oblique and parallel waves assuming the same amplitude of electric field, we would get smaller values for larger wave normal angles, due to relatively smaller values of the wave magnetic field for quasi-electrostatic waves. For larger wave normal angles ψ, the refactive index μ becomes larger, and the average angle between the wave vector and the wave electric field becomes smaller (due to the more electrostatic nature of the wave), so that their product depends on ψ in a relatively smooth way. Therefore, our estimates for R are not critical to the exact knowledge of the wave normal angle. For typical parameters of oblique hiss waves in the magnetosphere ($L \sim 3\text{-}4$, $\mu \sim 10^2 - 10^3$, $\psi \sim 50^o - 80^o$) we can numerically estimate the value of R using the APM computer code* [*Chmyrev et al.*, 1991] as $R \sim 1$.

Using trigonometric identities, we can rewrite (4.4.11) in the form

$$R = R_0 \cos(\phi + k_\parallel r_0 - \theta) \qquad (4.4.12)$$

---

* This is a general warm plasma code which for a given wave frequency allows the determination the frequency, the wave vector, the damping rate and polarization characteristics for the warm multicomponent magnetoplasma.

where θ is a constant and R_0 is the maximum value of R, estimated above as $R \sim 1$. Substituting (4.4.12) in (4.4.10), we note that the expression for $\frac{dv_\parallel}{dt}$ is in the form of the equation of motion for a particle moving in a potential well

$$\frac{dv_\parallel}{dt} = \Phi(r_0)$$

where

$$\Phi(r_o) = -\frac{e}{2mc}E_0 v_\perp R_0 \cos(\phi + k_\parallel r_0 - \theta)$$

The variation of the parallel velocity $v_\parallel$ results in the variation of the phase $k_\parallel r_0$ of the particle with respect to the wave, since $\frac{dr_0}{dt} = v_\parallel$. We can estimate the frequency and the amplitude of oscillations of electrons trapped by the wave* [*Landau and Lifshitz*, 1976] using $\Omega^2 = \frac{d\Phi}{dr_o}$ evaluated at the equilibrium point (i.e., where $\Phi = 0$)

$$\Omega^2 \sim \frac{e}{2mc}E_0 v_\perp R_0 k_\parallel \qquad (4.4.13)$$

$$\Delta v_{\parallel max} \sim \frac{\pi\Omega}{k_\parallel} \qquad (4.4.14)$$

The change in the electron parallel velocity corresponds to a change in the resonant parallel component of the wave vector. The relation between the two can be found by differentiating equation (4.2.1)

$$\Delta v_{\parallel max} = (v_{g\parallel} - v_\parallel)\frac{\Delta k_\parallel}{k_\parallel} \qquad (4.4.15)$$

where v_g is the group velocity of the wave. For large wave normal angles, we can estimate $v_{g\parallel} \sim \omega/k_\parallel$ and from (4.2.1) we obtain $v_\parallel = (\omega - \omega_H)/k_\parallel$. Since typically $\omega \ll \omega_H$, we have $|v_\parallel| \gg v_{g\parallel}$. From the latter inequality it follows that equation (4.4.14) is equivalent to equation (4.3.4).

---

* In fact, depending on specific structure of the wave packet and on the relative phase between the particle gyromotion and the wave field, some particles may be not trapped by the wave. In this case, $\Delta v_{\parallel max}$ denotes the maximum change in the velocity of the particle due to interaction with the wave, and Ω is the inverse time needed to change the velocity of the particle by $\Delta v_{\parallel max}$.

The above derivation was performed for electron interaction with a monochromatic wave. If electrons interact with magnetospheric hiss with an incoherent broadband spectrum, at any point of the trajectory they effectively interact with a narrow band in the wave spectra in the vicinity of the resonance. To apply our formulation to this case, we can replace the amplitude of the wave by

$$E_0 = E_k \Delta k_{\parallel}^{\frac{1}{2}}$$ (4.4.16)

where E_k is the spectral density of the wave in the parallel component of the wave vector space. The rigorous approach to choose $\Delta k_{\parallel}$ [following the ideas in *Galeev and Sudan*, 1983] is to substitute (4.4.16) in (4.4.13) to determine Ω, then substitute this value of Ω in (4.4.14) and use the result in (4.4.15). The resulting equation can be solved for $\Delta k_{\parallel}$ as

$$\Delta k_{\parallel}^{\frac{3}{4}} \sim \frac{\pi}{v_g - v_{\parallel}} \left(\frac{e}{2mc} E_k v_{\perp} R_0 k_{\parallel} \right)^{\frac{1}{2}}$$ (4.4.17)

With $\Delta k_{\parallel}$ defined by (4.4.17) we can estimate all other parameters which are needed to calculate the diffusion coefficient.

In order to estimate the contribution to the diffusion coefficient numerically, we assume the following values of parameters typical for magnetospheric hiss: $\omega \sim 1$ kHz, $\omega_H \sim 15$ kHz, $k \sim 5 \times 10^{-5}$ cm^{-1}, $k_{\parallel} \sim 10^{-5}$ cm^{-1} (as follows from our data analysis in Chapter 2), $R_0 \sim 1$, and the wave magnetic field $B_w \sim 1$ pT/Hz$^{\frac{1}{2}}$. We can estimate the spectral density of the electric field as $E_{\omega} \sim B_{\omega}/R$. However, the estimation of E_k for (4.4.16) is not straightforward. In general, $E_k \sim E_{\omega} \frac{\Delta \omega}{\Delta k_{\parallel}}$, where $\Delta \omega, \Delta k_{\parallel}$ are changes of the resonant frequency and of the resonant parallel component of the wave vector. For parallel propagation, $\frac{\Delta \omega}{\Delta k_{\parallel}} \sim v_{\parallel g}$. However, for oblique quasi-electrostatic waves a change in $k_{\parallel}$ may be accompanied by only a small or no change in frequency (see Figure 4.1, where wave vectors span a broad range for the same frequency value). Qualitatively, this means that oblique waves may have a larger width of the wave packets in k space as compared to that of parallel propagation. Therefore, $\frac{\Delta \omega}{\Delta k_{\parallel}} \sim v_{\parallel g}$ provides only an

upper limit estimate in the case of oblique waves. This means that, for the same spectral density E_ω, oblique wave packets may have lower spectral densities in the wave vector space, resulting in lower rates of diffusion. The quantitative estimation of E_k requires the detailed knowledge of the wave packet structure, which possibly can be extracted from experimental data.

Using the highest value for the electric field spectral density resulting from $\frac{\Delta\omega}{\Delta k_\parallel} \sim v_{\parallel g}$, we estimate from (4.4.17) $\Delta k_\parallel \sim 3 \times 10^{-7}$ cm^{-1}, resulting in an estimate for the change in the parallel electron velocity due to the interaction with hiss wave packets of

$$\frac{1}{v_\perp}\frac{dv_{\parallel w}}{dt} \sim 2 \times 10^{-2} s^{-1} \tag{4.4.18}$$

where the subscript w denotes the contribution to the variation of $v_\parallel$ due to the wave-particle interaction. This quantity must now be compared with the $\frac{dv_\parallel}{dt}$ due to the mirror force. From the conservation of the first adiabatic invariant, we find

$$\frac{1}{v_\perp}\frac{dv_{\parallel m}}{dt} \simeq \frac{v_\perp}{2v_\parallel}\frac{1}{\omega_H}\frac{d\omega_H}{dt} \tag{4.4.19}$$

where $\frac{1}{\omega_H}\frac{d\omega_H}{dt}$ characterizes the rate of the relative change of the electron gyrofrequency along the trajectory. The right-hand side of (4.4.19) can be easily evaluated using the conservation of the first adiabatic invariant and a dipole field model for the magnetic field. We find

$$\frac{1}{v_\perp}\frac{dv_{\parallel m}}{dt} \simeq \frac{3v_{\perp eq}}{2LR_e}\frac{\sin\lambda(3+2\sin^2\lambda)}{(1+3\sin^2\lambda)^{\frac{5}{4}}\cos^5\lambda} \tag{4.4.20}$$

where $v_{\perp eq}$ is the perpendicular component of the particle velocity at the magnetic equator, and R_e is the radius of the earth. Figure 4.2 shows both the value of the right hand side of (4.4.20) (solid line) for $v_{\perp eq} = 10^9$ cm/s and $L=4$, and the right hand side of (4.4.18) (dashed line) versus magnetic latitude λ.

The near-equatorial region is characterized by relatively slight medium inhomogeneity, thus the contribution to $\Delta v_\parallel$ due to the wave particle interaction prevails. However, even
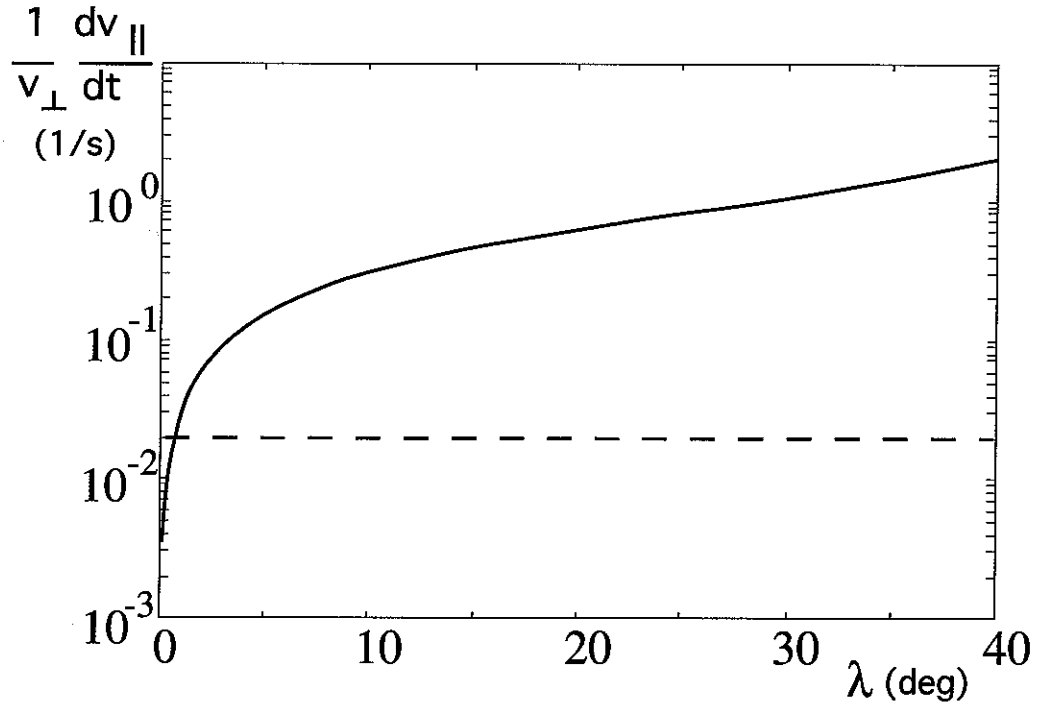
Fig. 4.2. The value of the right hand side of (4.4.20) (solid line) for $v_{\perp eq} = 10^9$ **cm/s and L=4, and the right hand side of (4.4.18) (dashed line) versus magnetic latitude** λ. The near-equatorial region is characterized by a slight inhomogeneity, thus the contribution to $\Delta v_{\parallel}$ due to wave particle interaction prevails. In a few degrees of latitude from the magnetic equator the medium inhomogeneity makes a major contribution to $\Delta v_{\parallel}$.

only a few degrees of λ from the magnetic equator the inhomogeneity term makes a dominant contribution to $\Delta v_{\parallel}$, so that we should modify classical expressions [[*Kennel and Petschek*, 1966; *Lyons*, 1972] for the electron diffusion in this region, accounting for the inhomogeneity of the medium. Note that for electrons with larger pitch angles, the region in the magnetosphere where the medium inhomogeneity may be neglected becomes even narrower than that shown in Figure 4.2. It should be noted, however, that the result in Figure 4.2 is for a wave spectral density of ~ 1 pT/Hz$^{\frac{1}{2}}$. For more

intense waves, the latitude region over which the wave forces dominate may be larger. Nevertheless, due to sharp dependence of the right-hand side of (4.4.20) on λ (see the solid line in Figure 4.2) the inhomogeneity dominates over most of the trajectory even for wave intensities which are two orders of magnitude higher than that used for our numerical estimates.

4.5 ELECTRON DIFFUSION COEFFICIENT RESULTING FROM INHOMOGENEITY OF THE MEDIUM

In this section we estimate the magnitude of the diffusion coefficient for the parallel velocity of energetic electrons in the region of the magnetosphere where the inhomogeneity is dominant. For the sake of simplicity, we assume that electrons move from resonance with one spectral harmonic to resonance with another driven solely by the mirror force. In this case, and to a zero approximation with respect to the wave field, the electron parallel velocity varies at a rate defined by the inhomogeneity, and, as a consequence, the electron interacts with different wave spectral harmonics. The variation of $v_\parallel$ due to the mirror force does not change the first adiabatic invariant, so that the diffusion term must be calculated to a first order approximation by substituting $r_0 = v_\parallel t$ in the right hand side of expressions (4.4.7) and (4.4.12). We find

$$\frac{dv_\parallel}{dt} = -\frac{e}{2mc}E_k \Delta k^{\frac{1}{2}} v_\perp R_0 \cos[(\omega - k_\parallel v_\parallel - \omega_H)t]$$

where we choose the $t = 0$ moment to correspond to precise resonance between the electron and the wave.

We now estimate the change in the electron parallel velocity due to its interaction with a narrow spectral band with a fixed frequency ω

$$\Delta v_{\parallel w} \sim \left(\frac{dv_\parallel}{dt}\right)_{max} \int_{-\infty}^{+\infty} \cos[(\omega - k_\parallel v_\parallel - \omega_H)t]dt \qquad (4.5.1)$$

where the subscript w denotes that $\Delta v_\parallel$ is evaluated to a first order approximation (i.e., as caused by the wave field), and

$$\left(\frac{dv_\parallel}{dt}\right)_{max} = \frac{e}{2mc}E_k\Delta k^{\frac{1}{2}}v_\perp R_0 \tag{4.5.2}$$

is the maximum rate of change of the electron parallel velocity corresponding to the exact resonance with $\omega - k_\parallel v_\parallel - \omega_H = 0$. Expanding the argument of the cosine function in (4.5.1) in a Taylor series in the vicinity of resonance, we have

$$\Delta v_{\parallel w} \sim v'_{max}\alpha^{-\frac{1}{2}} \tag{4.5.3}$$

where

$$\alpha = \frac{d}{dt}(\omega - k_\parallel v_\parallel - \omega_H) \tag{4.5.4}$$

The contribution of the integral (4.5.1) is largest in the vicinity of the resonance when the argument of the cosine varies relatively slowly. The characteristic time of interaction Δt can be estimated as that time during which the argument of the cosine varies over a $\pm\pi$ range around zero. This gives

$$\Delta t \sim \left(\frac{\pi}{\alpha}\right)^{\frac{1}{2}} \tag{4.5.5}$$

According to the general concept of electron diffusion, the resonant parallel component of the wave number changes during time Δt, so that electrons begin to interact with another wave spectral component of the wave. For small Δt we can assume that the resonant wave vector changes linearly with time during the interaction

$$\Delta k = k'\Delta t \tag{4.5.6}$$

where k' is a constant depending on the medium inhomogeneity and will be estimated below.

To estimate the diffusion coefficient we can calculate $\Delta v_{\parallel}$ due to both medium inhomogeneity and wave-particle interaction

$$\Delta v_{\parallel} = \Delta v_{\parallel m} + \Delta v_{\parallel w} \tag{4.5.7}$$

where subscript m denotes the change in the electron velocity as caused by the medium inhomogeneity. Squaring (4.5.7) and ensemble averaging over different values of $\Delta v_{\parallel w}$, we find

$$\Delta v_{\parallel}^2 = \Delta v_{\parallel m}^2 + \Delta v_{\parallel w}^2 \tag{4.5.8}$$

where we assumed that $\Delta v_{\parallel m}$ and $\Delta v_{\parallel w}$ are not correlated and that the average value of $\Delta v_{\parallel w}$ is zero. The first term in (4.5.8) is due to the inhomogeneity and has a fixed value at any point of the trajectory of a particle. Therefore, it does not affect the diffusion of particles in the velocity space, and the diffusion coefficient can be estimated similar to that for a homogeneous media [*Lyons et al.*, 1972]

$$D = \frac{\Delta v_{\parallel w}^2}{\Delta t} \tag{4.5.9}$$

Substituting (4.5.3) in (4.5.9) and accounting for (4.5.2),(4.5.6) we find

$$D = \left(\frac{ev_{\perp}}{2mc}\right)^2 \frac{CR^2 E_k^2 k'}{\alpha} \tag{4.5.10}$$

The numerical value for the diffusion coefficient depends on the ratio

$$F = \frac{k'}{\alpha} \tag{4.5.11}$$

Note that in the case of diffusion in a homogeneous media, the diffusion coefficient is defined by a formula similar to (4.5.10) where the ratio (4.5.11) is replaced by $F \to \frac{1}{v_{\parallel}}$ [e.g., *Kennel and Petschek*, 1966; *Inan*, 1987]. The denominator in (4.5.11) can be estimated using (4.2.1) and (4.5.4) as

$$\alpha = -v_{\parallel} k' - k_{\parallel} \frac{dv_{\parallel m}}{dt} - \frac{d\omega_H}{dt} \tag{4.5.12}$$

To estimate k' in (4.5.11) and (4.5.12) we use the approximate dispersion equation for oblique quasielectrostatic whistler mode waves (see (3.3.1) for $\omega \ll \omega_H$)

$$\frac{k_\parallel}{k} \simeq \frac{\omega}{\omega_H} \qquad (4.5.13)$$

which results in

$$k' \simeq -\frac{k_\parallel}{\omega_H} \frac{d\omega_H}{dt} \qquad (4.5.14)$$

From the conservation of the first adiabatic invariant we have

$$dv_{\parallel m} = -\frac{\omega_H}{2} \frac{v_\perp^2}{v_\parallel} d\omega_H \qquad (4.5.15)$$

Substituting (4.5.12) through (4.5.15) in (4.5.11) we find

$$F = \frac{1}{2 + \frac{1}{2}\frac{v_\perp^2}{v_\parallel^2}} \frac{1}{v_\parallel} \qquad (4.5.16)$$

Note that the value of F depends on the electron pitch angle, being smaller for large pitch angles (i.e., when $\frac{v_\perp^2}{v_\parallel^2} \gg 1$). The most important feature of equation (4.5.16) is that it gives lower values for the diffusion coefficient for electrons with large pitch angles as compared to the case of homogeneous media for the same value of E_k. In addition to the effect of the inhomogeneity, the electric field spectral density E_k may have smaller values for oblique waves for the same value of the measurable quantity E_ω, as discussed above in connection with equation (4.4.11). Therefore, we estimate that electron diffusion in the field of an oblique wave packet should have a lower rate as compared to parallel propagating waves, in qualitative agreement with results by *Inan and Bell* [1991]. However, this does not mean that the total amount of the precipitating electrons should be lower for oblique waves. As we mentioned in Section 4.2, an oblique wave packet may interact with electrons over a broader range of energies, so that lower diffusion rates may be compensated by larger number of electrons involved in the interaction as was shown by *Inan* [1987]. Sections 4.2-4.5 merely provides a preliminary analytical

framework and that is useful for the comparison of electron interactions with oblique versus parallel propagating wave packets. A comprehensive analytical theory of electron interaction with hiss accounting for both medium inhomogeneity and large wave normal angles may be a topic of future research.

5

Summary and suggestions for future work

5.1 SUMMARY

In this section, we summarize first the present status of our knowledge of the origin and $\vec{k}$-spectrum of plasmaspheric hiss and then the new results put forth in this dissertation.

5.1.1 Summary of the results from previous studies

Plasmasheric hiss is a band-limited noise-like emission, omnipresent in the plasmasphere. The range of frequencies over which plasmaspheric hiss is observed depends on the altitude, but is usually from a few hundred Hz to a few kHz. The highest hiss wave power densities are typically observed below 1 kHz. The peak power density varies up to two orders of magnitude depending upon magnetospheric activity, and also exhibits some random variations; the average value is $\sim 10^{-6}\gamma^2/\text{Hz}$. The power density is higher during magnetically quiet periods, especially during the recovery phase of magnetic storms. Typically, hiss is observed at high altitudes, from $L \sim 2$ to the plasmapause, and is rarely observed outside the plasmapause. The only exception is the afternoon sector at high geomagnetic latitude ($\lambda > 35^o$), where hiss is observed well beyond the plasmapause. A few previous studies of hiss wave vector direction have shown plasmaspheric hiss

to propagate at high wave normal angles ($\theta \sim 50^o - 85^o$), though some minor part of hiss can propagate at low wave normal angles. Plasmaspheric hiss can be triggered by whistlers; in this case, a hiss-like signal lasts about $\sim$ 5-15 s after the whistler and has many of the properties of regular hiss. Observations and direct experiments using ground based transmitters show that chorus emissions can often be triggered out of hiss band.

Despite intensive study and many observations, the mechanism of plasmaspheric hiss generation remains unclear. One of the mechanisms proposed previously suggests that the energetic electron fluxes in the magnetosphere are a source of energy for plasmaspheric hiss generation [*Kennel and Petschek*, 1966; *Church and Thorne*, 1983]. This mechanism predicts the generation of plasmaspheric hiss with low wave normal angles via gyroresonant interaction, since the increment of the whistler wave growth due to the interaction with energetic electrons is highest for parallel propagation in this case. Ray-tracing simulations show that some unique ray trajectories do propagate along a quasi periodical path with small wave-normal angles in the equatorial region (so-called 'cyclic trajectories') [*Church and Thorne*, 1983]. Since satellite data analysis shows that hiss has high wave-normal angles [*Lefeuvre and Helliwell*, 1985; *Storey et al.*, 1991; *Sonwalkar and Inan*, 1988], gyroresonant amplification along the cyclic trajectories cannot explain the generation of all the hiss. One possible way to overcome this problem is to assume that whistler mode waves can be amplified from the thermal level during a single pass through the equatorial region [*Solomon et al.*, 1988]. After the wave is amplified, it acquires high wave normal angles due to the propagation in the inhomogeneous earth's magnetic field. Another mechanism suggests the ring current protons as a source of energy for hiss [*Parady*, 1974]. This mechanism contributes to the generation of hiss with high wave normal angles and with frequencies close to the lower hybrid frequency.

5.1.2 The new picture of the origin and $\vec{k}$-spectrum of hiss

In this dissertation research we analyzed experimental data on plasmaspheric hiss to measure its $\vec{k}$-spectrum and performed analytical and numerical modeling of whistler mode wave propagation in the magnetosphere to clarify the origin of hiss. We provided the results of hiss wave vector direction measurements in 22 different cases based on DE-1 satellite wave data, representing a wide range of L shells and thus allowing the analysis of general trends in hiss wave normal angles. The results of these measurements strongly suggest that hiss generally propagates at high wave normal angles. The azimuthal angles of the wave vector directions of hiss (i.e., angles between the wave vector and the meridional plane) cover a wide range, often corresponding to propagation at large angles with respect to the meridional plane.

We also performed the first simultaneous measurements of the wave vector direction of discrete whistlers (originating in lightning and arriving at the satellite over a short direct path) and plasmaspheric hiss as observed on the DE-1 satellite. The whistler wave normal angles and dispersion characteristics were consistent with propagation over typical nonducted magnetospheric paths with the wave vector being at $50^o - 60^o$ with respect to the ambient magnetic field and within $< 20^o$ with respect to the meridional plane. The wave normal angles of the simultaneously observed hiss were found to be larger, being $70^o - 77^o$. The azimuthal angles of the wave vector for hiss were found to be $\sim 80^o$ with respect to the magnetic meridional plane.

The results of the measurements form an experimental basis for the new mechanism of plasmaspheric hiss generation put forth in this work. On the basis of extensive two- and three-dimensional ray tracing, we have shown that hiss-like signals can be formed by nonducted whistlers as a result of propagation effects only. The combined contribution from whistler rays produced by a single lightning flash but entering the magnetosphere at different points and locations and/or with different initial wave vectors forms a continuous hiss-like signal in the magnetosphere, as observed at a fixed point.

Our model of plasmaspheric hiss generation and sustenance is based on the fact that whistler waves generated by lightning can persist for a long time in the magnetosphere undergoing multiple magnetospheric reflections and effectively being 'stored' in the magnetospheric resonator. Quantitative modeling of whistler-mode waves propagating in the magnetospheric plasma with a high-energy non-Maxwellian tail was reported by *Huang et al.* [1983] as part of a hiss propagation study, where it was shown that whistler-mode signals originating with an initial intensity greater than the thermal level can propagate a considerable distance before damping out, and that the total growth/damping rates for such waves are low. The results of our calculations show that while the first several hops of impulsive wave energy from lightning form discrete magnetospherically reflected whistler components [*Edgar*, 1976], subsequent reflections can lead to the formation of continuous hiss-like signals with a durations of up to $\sim 10^2$ sec at lower frequencies (~ 1 kHz). Based on these estimates, we suggest that lightning activity can be a source for magnetospheric hiss without any amplification of whistler mode waves as long as the whistler damping rates in the magnetosphere are relatively low. The hiss-like signals produced by magnetospherically reflected whistlers have properties that are in qualitative agreement with reported experimental data on plasmaspheric hiss, in particular, with Dynamic Explorer-1 observations of the features (upper and lower cutoff frequencies and their variation with time) of hiss-like signals which often follow whistlers [*Sonwalkar and Inan*, 1989]. The spectra of the hiss-like signals formed by discrete whistlers is highly dependent on the *L*-shell of observation.

According to our model, most plasmaspheric hiss would be observed at high wave-normal angles, in agreement with experimental results [*Lefeuvre et al.*, 1983; *Sonwalkar and Inan*, 1988]. On the other hand, hiss spectra observed by satellites has on occasion spectral components below the local LHR frequency [e.g., *Church and Thorne*, 1983, see Figure 1], which has not been studied in detail in this thesis. However, some of the observed hiss may appear to be at lower frequencies due to relatively large Doppler shifts that would be expected in view of the high wave normal angles. For a wavenumber of

$k \sim 10^{-3}$ cm^{-1} which is typical for our ray-tracing simulations, the Doppler shift can be as high as $\sim 10^2$ Hz. Another possible way by which hiss generation with $\omega < \omega_{LHR}$ can occur in our model was discussed in Section 3.7, where we have shown that such rays are subject to magnetospheric reflection similar to that for higher frequency ($\omega > \omega_{LHR}$) rays. Therefore, it is potentially possible that hiss energy below the local lower hybrid frequency may also be formed by multiply reflecting whistlers, similar to the higher frequency hiss. Comprehensive consideration of hiss propagation below ω_{LHR} is a topic of future research.

The fact that the measured wave vector directions of both whistlers and hiss have significant components in azimuth indicate that considerations of three dimensional ray propagation are important in assessing the possible causative connection between whistlers and hiss. An approximate analytical model was put forth to evaluate the propagation of quasi-electrostatic whistler waves in three dimensions. Applications of the model indicate that waves injected from fixed thunderstorm centers on the ground may be observed at longitudes which differ from those of the lightning flash by as much as $\pm 40^o$ (accounting for $\pm 10^o$ propagation in the earth-ionosphere waveguide and $\pm 30^o$ drift of the wave packet in the ionosphere and the magnetosphere). Considerations of group delay and overlap of many such waves lend support to the concept of formation of magnetospheric hiss as a superposition of magnetospherical reflected whistlers. Since the longitude drift of whistler mode waves is limited to $\sim 40^o$, any possible causative connection between whistlers and hiss should manifest itself as a longitudinal correlation between regions on the ground of high thunderstorm activity (i.e., regions of higher whistler rates), and magnetospheric regions of higher average hiss intensity.

Since hiss is an intense noise-like broadband signal, magnetospheric electrons can diffuse in velocity space due to gyroresonant interactions with hiss. Some of the energetic electrons diffuse from higher pitch angles to inside the loss cone, and precipitate into the lower ionosphere. In this way, the presence of plasmaspheric hiss places a limit on energetic electron fluxes, and due to the omnipresence of hiss in the plasmasphere and

its relatively high amplitude, hiss is believed to play the major role in radiation belt dynamics [*Kennel and Petschek*, 1966]. Measurements of hiss wave vector directions presented in this thesis, which reveal that hiss generally propagates at high wave normal angles, show that theoretical models of hiss interaction with energetic particles have to be reconsidered to account for the generally high wave normal angles of hiss. In this thesis we presented preliminary estimates of electron diffusion in velocity space in oblique wave packets and compared the rate of diffusion to that which occurs in quasi-longitudinal (i.e., parallel propagating) wave packets. We showed that the rate of electron diffusion due to their interaction with oblique wave packets in the inhomogeneous magnetosphere may be considerably smaller than that of electrons interacting with parallel waves in homogeneous media due to two effects: (i) the width of the wave packet in wave vector space may be larger, resulting in lower spectral densities for the same wave amplitudes; (ii) the inhomogeneity of the medium which causes the electrons to move from from one resonance to another faster than they would otherwise, resulting in reduced diffusion coefficient for large pitch angles.

5.2   SUGGESTIONS FOR FUTURE WORK

Future research on plasmaspheric hiss may concentrate on the further clarification of the spectral features of hiss, mechanisms of its generation and the role of hiss in terms of its effects on the radiation belt particles. In particular, a comprehensive study of the mechanisms of hiss generation is needed. While this work (as well as some previous studies, e.g. *Sonwalkar and Inan* [1989]) shows that there undoubtedly is a connection between hiss and whistlers, the extent of this connection remains not entirely clear. We have shown that plasmaspheric hiss may be produced by multiply reflecting nonducted whistlers, and that the input energy from whistlers on a global scale is sufficient to produce magnetospheric hiss. However, this dissertation does not establish the quantitative extent of the causative link between hiss and whistlers on a global scale. We believe that an extensive statistical study of hiss occurence and its correlation with regions of high

lightning rates may bring decisive new understanding of the connection between hiss and whistlers.

Another aspect of hiss which has not been investigated in detail in the current study is its generation and propagation at frequencies below the local lower hybrid frequency. We have shown in a qualitative fashion that it is possible for whistler waves with $\omega < \omega_{LHR}$ to propagate similarly to higher frequency waves, and undergo magnetospheric reflections. Therefore, waves below the lower hybrid frequency may be stored in the magnetosphere, and the suggested model of hiss generation may work for waves with $\omega < \omega_{LHR}$ as well as for waves with $\omega > \omega_{LHR}$. However, extensive ray tracing modeling of wave propagation needs to be undertaken in order to quantitatively establish possible generation of the low frequency ($\omega < \omega_{LHR}$) hiss by nonducted whistlers.

According to our ray tracing calculations, nonducted whistler mode waves reflect from regions where their frequency is approximately equal to the local lower hybrid frequency, and do not penetrate deeply into lower altitudes. This simplistic model does not account for hiss penetration to lower altitudes as observed in the experimental data [*Gurnett and Burns*, 1968; *Muzzio and Angerami*, 1972]; however, such penetration can possibly occur as a result of reflection of ducted hiss waves from the lower ionospheric boundary and nonducted propagation upward. Such hybrid propagation (i.e., ducted followed by nonducted) is a known means by which ducted-mode whistler waves can populate large regions of the magnetosphere [*Rastani et al.*, 1985; *Smith et al.*, 1985]. Additional work is needed to extend our model of hiss generation to ducted hiss and its possible connections to nonducted hiss.

Recent experimental data on wave vector directions of plasmaspheric hiss, including those provided in this thesis, show that typically the propagation occurs with oblique wave normals. As we discussed above, particle diffusion in oblique whistler wave packets differs from that in quasi-longitudinal waves in both the energy of the interacting paticles and the rate of particle pitch-angle diffusion. We believe that models of hiss interaction

with radiation belt particles have to be modified to account for the oblique wave vector directions of hiss. The study of interaction between obliquely propagating hiss and radiation belt electrons may have important implications for our understanding of the radiation belt dynamics and equilibrium.

Both wave-wave and wave-particle interactions affect fine features of the wave spectra, including phase correlations between spectral components. General equations of the wave turbulence [*Galeev and Sudan*, 1983] link the phase of different wave spectral components to coefficients of the wave coupling due to wave-wave and/or wave-particle interactions. Analyzing wideband experimental data, one can get information on the interactions in which the waves are involved. The first attempt of this kind was made by *Kabanov* [1990], where ground observations of hiss were used to estimate the Nakagami parameter* for the hiss signal. The results of the paper by *Kabanov* [1990] show that ground observed hiss is not equivalent to random noise, which possibly may be connected to the effects of wave-wave or wave-particle interactions on the hiss wave packets. In this connection, *Sonwalkar and Inan* [1988] also found evidence for some underlying coherence in hiss based on their observation of a ~30 Hz modulation of hiss intensity.

---

* The Nakagami parameter is defined through the second and the fourth moments of the distribution of the wave amplitude with respect to frequency [*Kabanov*, 1990], reflecting the signal-to-noise ratio.

Bibliography

Aikyo, K., and T. Ondoh, Propagation of nonducted VLF waves in the vicinity of the plasmapause, *J. Radio Res. Lab. Jpn., 18*, 153, 1971.

Angerami, J. J., and J. O. Thomas, Studies of planetary atmosphere, 1, The distribution of electrons and ions in the earth's exosphere, *J. Geophys. Res., 69*, 4537, 1964.

Bell, T. F., The wave magnetic field amplitude threshold for nonlinear trapping of energetic gyroresonant and Landau resonant electrons by nonducted VLF waves in the magnetosphere, *J. Geophys. Res., 91*, 4365, 1986.

Bell, T. F., and U. S. Inan, ISEE-1 observations in the magnetosphere of VLF emissions triggered by nonducted coherent VLF waves during VLF wave-injection experiments, *Adv. Space Res., 1*, 203, 1981.

Bell, T. F., U. S. Inan, and R. A. Helliwell, Non-ducted coherent VLF waves and associated triggered emissions observed on the ISEE-1 satellite, *J. Geophys. Res., 86*, 4649, 1981.

Bell, T. F., and H. D. Ngo, Electrostatic lower hybrid waves excited by electromagnetic whistler mode waves scattering from planar magnetic-field-aligned plasma density irregularities, *J. Geophys. Res., 95*, 149, 1990.

Bracewell, R. N., *The Fourier transform and its applications*, McGraw-Hill, New York, 1986, 474 pp.

Brittain, R., P. M. Kintner, M. C. Kelley, J. C. Siren, and D. L. Carpenter, Standing wave patterns in VLF hiss, *J. Geophys. Res., 88*, 7059, 1983.

Budden, K. G., *The propagation of radio waves*, Camb. Univ. Press, Cambridge, 1985, 669 pp.

Cairó, L., and F. Lefeuvre, Localization of sources of ELF/VLF hiss observed in the magnetosphere: Three-dimensional ray tracing, *J. Geophys. Res., 91*, 4352, 1986.

Carpenter, D. L., On what ionospheric workers should know about the plasmapause-plasmasphere, *Reviews of geophysics and space physics, 11*, 133, 1973.

Carpenter, D. L., and R. E. Orville, The excitation of active whistler mode signal paths in the magnetosphere by lightning: two case studies, *J. Geophys. Res., 94*, 8886, 1989.

Chan, K.-W., and R. E. Holzer, ELF hiss associated with plasma density enhancements in the outer magnetosphere, *J. Geophys. Res., 81*, 2267, 1976.

Chmyrev, V. M., A. B. Draganov, Yu. N. Taranenko, and D. Teodosiev, Acceleration of particles in the upper ionosphere and the magnetosphere due to decay interactions of whistlers. 1, *Phys. Scripta, 43*, 495, 1991.

Church, S. R., and R. M. Thorne, On the origin of plasmaspheric hiss: Ray path integrated amplification, *J. Geophys. Res., 88*, 7941, 1983.

Dunckel, N., and R. A. Helliwell, Whistler-mode emissions on the OGO 1 satellite, *J. Geophys. Res., 74*, 6371, 1969.

Edgar, B. C., *The structure of the magnetosphere as deduced from magnetospherically reflected whistlers*, Ph.D. thesis, Stanford University, Stanford, Calif., 1972.

Edgar, B. C., The upper and lower frequency cutoffs of magnetospherically reflected whistlers, *J. Geophys. Res., 81*, 205, 1976.

Etcheto, J., R. Gendrin, J. Solomon, and A. Roux, A self-consistent theory of magneto-spheric ELF hiss, *J. Geophys. Res., 78*, 8150, 1973.

Galeev, A. A., and R.N. Sudan (editors), *Basic plasma physics*, North-Holland Pub., Amsterdam; New York, 1983.

Gendrin, R., Le guidage des whistlers par le champ magnetique, *Planet. Space Sci., 5*, 274, 1961.

Green, J. L., D. A. Gurnett, and S. D. Shawhan, The angular distribution of auroral kilometric radiation, *J. Geophys. Res., 82*, 1825, 1977.

Gurnett, D. A., and B. Burns, The low frequency cutoff of ELF emissions, *J. Geophys. Res.*, *73*, 7437, 1968.

Gurnett, D. A., and U. S. Inan, Plasma wave observations with the Dynamics Explorer 1 spacecraft, *Rev. of Geophys.*, *26*, 285, 1988.

Hattori, K., M. Hayakawa, D. Lagoutte, M. Parrot, and F. Lefeuvre, Further evidence of triggering chorus emissions from wavelets in the hiss band, *Planetary and Space Science 39*, 1465, 1991.

Helliwell, R. A., *Whistlers and related ionospheric phenomena*, Stanford University Press, Stanford, Calif., 1965, 349pp.

Helliwell, R. A., VLF wave-injection experiments from Siple Station, Antarctica *Adv. Space Res.*, *8*, 279, 1988.

Helliwell, R. A., D. L. Carpenter, U. S. Inan, and J. P. Katsufrakis, Generation of band-limited VLF noise using the Siple transmitter: A model for magnetospheric hiss, *J. Geophys. Res.*, *91*, 4381, 1986.

Himmelblau, D. M., *Applied nonlinear programming*, McGraw-Hill, New York, 1972, 498 pp.

Horne, R. B., Path integrated growth of electrostatic waves: the generation of terrestial myriametric radiation, *J. Geophys. Res.*, *94*, 8895, 1989.

Huang, C. Y., and C. K. Goertz, Ray-tracing studies and path-integrated gains of ELF unducted whistler mode waves in the Earth's magnetosphere, *J. Geophys. Res.*, *88*, 6181, 1983.

Huang, C. Y., C. K. Goertz, and R. R. Anderson, A theoretical study of plasmaspheric hiss generation, *J. Geophys. Res.*, *88*, 7927, 1983.

Inan, U. S., Gyroresonant pitch angle scattering by coherent and incoherent whistler mode waves in the magnetosphere, *J. Geophys. Res.*, *92*, 127, 1987.

Inan, U. S., and T. F. Bell, The plasmapause as a VLF wave guide, *J. Geophys. Res.*, *82*, 2819, 1977.

Inan, U. S., and T. F. Bell, Pitch angle scattering of energetic particles by oblique whistler waves, *Geophys. Res. Let*, *18*, 49, 1991.

Inan, U. S., T. F. Bell, and R. A. Helliwell, Nonlinear pitch angle scattering of energetic electrons by coherent VLF waves in the magnetosphere, *J. Geophys. Res., 83,* 3235, 1978.

Jasna, D., U. S. Inan, and T. F. Bell, Equatorial gyresonance between electrons and and magnetospherically reflected whistlers, *Geophys. Res. Let., 17,* 1865, 1990.

Jasna, D., U. S. Inan, and T. F. Bell, Precipitation of suprathermal (100 eV) electrons by oblique whistler waves, *Geophys. Res. Let., 19,* 1639, 1992.

Kabanov, V. V., The statistical structure of VLF-emissions, *Geomagnetism and Aeronomy, 30,* 776, 1990.

Kennel, C. F., and H. E. Petschek, Limit on stably trapped particle fluxes, *J. Geophys. Res., 71,* 1, 1966.

Koons, H. C., The role of hiss in magnetospheric chorus emissions, *J. Geophys. Res., 86,* 6745, 1981.

Koons, H. C., Observations of large-amplitude, whistler mode wave ducts in the outer plasmasphere, *J. Geophys. Res., 94,* 15393, 1989.

Krall, N. A., and A. W. Trivelpiece, *Principles of plasma physics,* McGraw-Hill, New York, 1973, 674 pp.

Landau, L. D. and E. M. Lifshitz, *Mechanics,* Pergamon Press, New York, 1976, 169 pp.

Lefeuvre, F., and R. A. Helliwell, Characterization of the sources of VLF hiss and chorus observed on GEOS 1, *J. Geophys. Res., 90,* 6419, 1985.

Lefeuvre, F., M. Parrot, and C. Delannoy, Wave distribution functions estimation of VLF electromagnetic waves, *J. Geophys. Res., 86,* 2359, 1981.

Lefeuvre, F., M. Parrot, L. R. O. Storey, and R. R. Anderson, Wave distribution functions for plasmaspheric hiss observed on board ISEE 1, *Tech. Note LPCE/6,* Lab. de Phys. et chim. de l'Environ., Orleans, France, 1983.

Lefeuvre, F., J. L. Rauch, J. J. Berthelier, and J. M. Bosqued, Direction of the Poynting flux for low altitude ELF hiss, paper presented at IAGG Symposium, Vienna, 1991.

Lefeuvre, F., J. L. Rauch, D. Lagoutte, J. J. Berthelier, and J. C. Cerisier, Propagation characteristics of dayside low-altitude hiss: case studies, *J. Geophys. Res., 97,* 10601, 1992.

Lyons, L. R., and D. J. Williams, *Quantitative Aspects of Magnetospheric Physics*, D. Riedel Publishing Co., Dordrecht, 1984, 231 pp.

Lyons, L. R., R. M. Thorne, and C. F. Kennel, Pitch-angle diffusion of radiation belt electrons within the plasmasphere, *J. Geophys. Res., 77*, 3455, 1972.

Maggs, J. E., Nonlinear evolution of the auroral electron beam, *J. Geophys. Res., 94*, 3631, 1989.

Muzzio, J. L. R., and J. J. Angerami, OGO 4 observations of extremely low frequency hiss, *J. Geophys. Res., 77*, 1157, 1972.

Parady, B. K., Anisotropic proton instability magnetospheric (APIM) hiss: An introduction, *Geophys. Res. Let., 1*, 235, 1974.

Parady, B. K., D. D. Eberlein, J. A. Marvin, W. W. L. Taylor, and L. J. Cahill, Jr., Plasmaspheric hiss observations in the evening and afternoon quadrants, *J. Geophys. Res., 80*, 2183, 1975.

Parrot, M., World map of ELF/VLF emissons as observed by a low-orbiting satellite *Annales Geophysicae, 8*, 135, 1990.

Peckham, D. W., M. A. Uman, and C. E. Wilcox, Jr., Lightning phenomenology in the Tampa Bay Area, *J. Geophys. Res., 89*, 11789, 1984.

Pinto, O., Jr., and W. D. Gonzalez, The role of Landau resonance in energetic electron precipitation from the inner radiation belt, *J. Geophys. Res., 94*, 12027, 1989.

Press, W. H., S. A. Teukolsky, W. T. Vetterling, and B. P. Flannery, *Numerical recipes in FORTRAN*, Cambridge Univ. Press, Cambridge, 1992, 963 pp.

Rastani, K., U. S. Inan, and R. A. Helliwell, DE-1 observations of Siple transmitter signals and associated sidebands, *J. Geophys. Res., 90*, 4128, 1985.

Shawhan, S. D., D. A. Gurnett, D. L. Odem, R. A. Helliwell, and C. G. Park, The plasma wave and quasi-static electric field instrument (PWI) for Dynamics Explorer-A, *Space Sci. Instrum., 5*, 535, 1981.

Smith, R. L., and J. J. Angerami, Magnetospheric properties deduced from OGO-1 observations of ducted and non-ducted whistlers, *J. Geophys. Res., 73*, 1, 1968.

Smith, A. J., D. L. Carpenter, and U. S. Inan, Whistler-triggered VLF noise bursts observed on the DE-1 satellite and simultaneously at Antarctic ground stations, *Annales Geophysicae, 3*, 81, 1985.

Smith, E. J., A. M. A. Frandsen, B. T. Tsurutani, R. M. Thorne, and K. W. Chan, Plasmaspheric hiss intensity variations during magnetic storms, *J. Geophys. Res.*, *79*, 2507, 1974.

Solomon, J., N. Cornilleau-Wehrlin, A. Korth, and G. Kremser, An experimental study of ELF/VLF hiss generation in the earth's magnetosphere, *J. Geophys. Res.*, *93*, 1839, 1988.

Sonwalkar, V. S., and U. S. Inan, Measurements of Siple transmitter signals on the DE 1 satellite: wave normal direction and antenna effective length, *J. Geophys. Res.*, *91*, 154, 1986.

Sonwalkar, V. S., and U. S. Inan, Wave normal direction and spectral properties of whistler mode hiss observed on the DE 1 satellite, *J. Geophys. Res.*, *93*, 7493, 1988.

Sonwalkar, V. S., and U. S. Inan, Lightning as an embryonic source of VLF hiss, *J. Geophys. Res.*, *94*, 6986, 1989.

Sonwalkar, V. S., T. F. Bell, R. A. Helliwell, and U. S. Inan, Direct multiple path magnetospheric propagation: A fundamental property of nonducted VLF waves, *J. Geophys. Res.*, *89*, 2823, 1984.

Stix, T. H., The theory of plasma waves, McGraw-Hill, New York, 1962, 283 pp.

Storey, L. R. O., An investigation of whistling atmospherics, *Philos. Trans. R. Soc. London, Ser. A, 246*, 113, 1953.

Storey, L. R. O., F. Lefeuvre, M. Parrot, L. Cairo, and R. R. Anderson, Initial survey of the wave distribution functions for plasmaspheric hiss observed by ISEE 1, *J. Geophys. Res.*, *96*, 19469, 1991.

Sulič, D.M., and G. Gustafsson, Study of whistlers recorded by Viking, paper presented at IUGG XX General Assembly, Vienna, 1991.

Thorne, R. M., S. R. Church, and D. J. Gorney, On the origin of plasmaspheric hiss: The importance of wave propagation and the plasmapause, *J. Geophys. Res.*, *84*, 5241, 1979.

Thorne, R. M., E. I. Smith, R. K. Burton, and R. E. Holzer, Plasmaspheric hiss, *J. Geophys. Res.*, *78*, 1581, 1973.

Uman, M. A., *Lightning*, McGraw Hill, New York, 1987, 264 pp.